DEMOCRATIC AND PEOPLE'S REPUBLIC OF ALGERIA MINISTRY
OF HIGHER EDUCATION AND SCIENTIFIC RESEARCH
ABOU-BEKR BELKAID UNIVERCITY – TLEMCEN

DOCTORAL THESIS

Presented to:

FACULTY OF SCIENCES – DEPARTMENT OF PHYSICS

For obtaining the diploma of:

DOCTORATE

Specialty: *Renewable Energies*
By :

Mr KACEM CHERIFI

On the theme

Computational Investigation of $ZnTiO_3$ Perovskite Based Photo-anode for Dye Sensitized Solar Cell Application

---

Publicly defended on 30/10/2022 in Tlemcen in front of a jury composed of:

Mr KALAIDJI Djamal	Professeur	University of Tlemcen	President
M_r CHEKNANE Ali	Professeur	University of Laghouat	Thesis director
Mme RAHMOUN Khadidja	Professeur	University of Tlemcen	Thesis Co-Director
Mr MERAD Abdelkrim	Professeur	University of Tlemcen	Examiner
Mr BASSOU Ghaouti	Professeur	University of Sidi Belabbes	Examiner
Mr NUNZI Michel	Professeur	University of Queen's	Examiner
Mr BENGHIA Ali	MCA	University of Laghouat	Guest

L'Unité de Recherche Matériaux et Énergies Renouvelables - URMER - , Abou Bekr Belkaid University, Tlemcen, 13000, Algeria..
Laboratoire des semiconducteurs et matériaux fonctionnels, Université Amar Telidji de Laghouat,BP37G, Bd des Martyrs, Laghouat (03000). Algeria.
Department of Physics, Engineering Physics and Astronomy, Queens University, Kingston, ONK7L-3N6, Canada.

Declaration of Authorship

I, Kacem CHERIFI, declare that this thesis titled, " Computational Investigation of $ZnTiO_3$ Perovskite Based Photo-anode for Dye Sensitized Solar Cell Application " and the work presented in it are my own. I confirm that:

- This work was done wholly or mainly while in candidature for a research degree at this University.
- Where any part of this thesis has previously been submitted for a degree or any other qualification at this University or any other institution, this has been clearly stated.
- Where I have consulted the published work of others, this is always clearly attributed.
- Where I have quoted from the work of others, the source is always given. With the exception of such quotations, this thesis is entirely my own work.
- I have acknowledged all main sources of help.
- Where the thesis is based on work done by myself jointly with others, I have made clear exactly what was done by others and what I have contributed myself.

Signed:

_____

Date:

_____

UNIVERSITY OF TLEMCEN

Abstract

Faculty of Science
Department of Physics

Doctor of Philosophy in the:

Computational Investigation of $ZnTiO_3$ Perovskite Based Photo-anode for Dye Sensitized Solar Cell Application

by Kacem CHERIFI

Dye-sensitised solar cells continue to be a promising photovoltaic technology for indoor and outdoor applications, with increased interest in power window applications integrated into buildings. This results from properties not seen in other, more established solar technologies, such as the range of available colours, partial transparency and good performance under low light intensities or in partial shade. TiO_2 and ZnO materials being developed and reported in the literature are the best candidates as photo-electrode in DSSC, since both of TiO_2 and ZnO metal oxides have their own advantages, combining both of them may yield a new hybrid system with higher performance of DSSC. in this work the perovskite $ZnTiO_3$ is investigated to combine the benefits of both TiO_2 and ZnO materials in term of chemical stability, excellent charge transport and high electron mobility, high surface area and suitable band gap and CBE, eventually a best photo-anode for dye-sensitised solar cell.

Les cellules solaires à colorant continuent d'être une technologie photovoltaïque prometteuse pour les applications intérieures et extérieures, avec un intérêt accru pour les applications de vitres électriques intégrées au bâtiment. Cela résulte de propriétés non observées dans d'autres technologies solaires plus établies, telles que la gamme de couleurs disponibles, une transparence partielle et de bonnes performances sous de faibles intensités lumineuses ou à l'ombre partielle. Les matériaux TiO_2 et ZnO en cours de développement et rapportés dans la littérature sont les meilleurs candidats comme photo-électrode dans DSSC, puisque les oxydes métalliques TiO_2 et ZnO ont leurs propres avantages, la combinaison des deux peut donner un nouveau système hybride avec des performances plus élevées de DSSC . Dans ce travail, la pérovskite ZnTiO3 est étudiée pour combiner les avantages des matériaux TiO_2 et ZnO en termes de stabilité chimique, d'excellent transport de charge et de mobilité électronique élevée, de surface élevée et de bande interdite et CBE appropriés, éventuellement une meilleure photo-anode pour les cellules solaires sensibilisée par un colorant. ...

تعد الخلايا الشمسية الحساسة الصبغية في كونها تقنية كهروضوئية واعدة للتطبيقات الداخلية والخارجية ، مع زيادة الاهتمام بتطبيقات النوافذ الكهربائية المدمجة في المباني. ينتج هذا عن خصائص لم تظهر في تقنيات الطاقة الشمسية الأخرى الأكثر رسوخًا مثل خلايا السيليكون، من بين هذه الخصائص، التنوع في ألوان الخلية الشمسية والشفافية الجزئية للخلية والأداء الجيد في حالة شدة الإضاءة المنخفضة أو في الظل الجزئي. تعد مواد ثنائي أكسيد التيتانيوم و أكسيد الزنك و التي يتم تطويرها والإبلاغ عنها في المقالات العلمية كأفضل مادتين مرشحين كقطب كهربائي ضوئي في خلايا الشمسية الحساسة الصبغية ، نظرًا لأن كل من أكاسيد المعدنية و لها مزاياها الخاصة ، فإن الجمع بين المادتين قد ينتج عنه نظام هجين جديد مع أداء أعلى لخلية الشمسية الحساسة الصبغية، فلهذا قد تم الفحص في هذا البحث عن مادة البيروفسكايت التي تجمع بين فوائد كل من مواد و من حيث الاستقرار الكيميائي ، ونقل الشحنة الممتاز ، وحركة الإلكترون العالية ، ومساحة السطح العالية ، وفجوة النطاق المناسبة ، مما يؤدي الى كونه كأحسن و أفضل قطب كهربائي ضوئي للخلايا الشمسية الصبغية الحساسة من حيث الأداء و الكفاءة .

Acknowledgements

I would like to express my special appreciation and thanks to my Supervisor Professor. Ali CHAKNANE for sponsoring me with a calculating station at his Materials, Energy Systems, Renewable Energies and Energy Management Laboratory (LMSEERGE), and my Co-supervisor Prof. Rahmoun KHADIDJA for hosting me at her Materials and Renewable Energies Research Unit (URMER), you have been a tremendous mentor to me. I would like to thank you for your continuous support in encouraging my research and for allowing me to grow as a research scientist. Your advice on both research as well as on my career has been invaluable. Not to mention, a special thanks to Dr. Ali BENGHIA for his technical support in the first stages of my Ph.D. journey. I would also like to thank Prof. Jean Michel Nunzi for his hospitality as a visiting research student with his powerful research team at Queen's University in Canada and his lab support of my research.

I would also like to thank my committee members, professor KALAIDJI Djamal, professor MERAD Abdelkrim,and professor BASSOU Ghaouti, for serving as my committee members even in hardship. I also want to thank you for letting my defense be an enjoyable moment, and for your brilliant comments and suggestions, thanks to you.

I would like to express my gratitude to my family. Words can not express how grateful I am to my mother and father for all of the sacrifices that you've made on my behalf. Without their tremendous understanding and encouragement over the past few years, it would be impossible for me to complete my study. Your prayer for me was what sustained me thus far.

A special thanks to my beloved fiancée, Miss. Yassmine for your lengthy patience with me in everything, and especially I can't appreciate you enough for encouraging me to finish my thesis before getting married. thanks to you.

To my dear Faye Ibbitson, I would like to express my thanks for being such a good Canadian mom during my staying with you in Canada in your lovely house with Toller and Tayla, I can't thank you enough for everything you have done for me throughout this experience and for always cheering me up. thanks to you.

Finally, I thank my God, for letting me through all the difficulties. I have experienced Your guidance day by day. You are the one who let me finish my degree. I will keep on trusting You for my future. Thank you, Lord. ....

Contents

List of Figures

List of Tables

List of Abbreviations

PV	PhotoVoltaic
C-si	Crystallin Siicon
TFSC	Thin Film Solar Cell
TFPV	Thin Film Photovoltaic
CPV	Concentrated Photovoltaic
DSSC	Dye Sensitized Solar Cell
OSC	Organic Solar Cell
PSC	Perovskite Solar cell
PCE	Power Conversion Efficiency
ETM	Electron Transport Material
CBE	Conduction Band Edge
VBE	Valence Band Edge
EPFL	École Polytechnique Fédérale de Lausanne
AM	Air Mass
PPV	Polymer Photovoltaic
CQD	Colloidal Quantum Dot
HCQD	High Colloidal Quantum Dot
MJ	Multijunction
SJ	Single Junction
MPP	Maximum Power Point
CdTe	Cadmium telluride
CIGS	Copper indium gallium selenide
CdTe	Cadmium telluride
NREL	National Renewable Energy Laboratory
TCO	Transparent Conductive Oxide
FTO	Fluorine-doped Tin Oxide
ITO	Indium-doped Tin Oxide
Pt	Platinum
HOMO	Highest Occupied Molecular Orbital
LOMO	Lowest Unoccupied Molecular Orbital
QD	Quantum Dot

NP	Nanoparticules
CE	Counter electrode
QDSSC	Quantum Dot Sensitized Solar Cell
CdS	Cadmium Sulfide
CdSe	Cadmium Selenide
DFT	Density Function Theory
HF	Hartree Fock
MS	Material Studio
CASTEP	CAmbridge Serial Total Energy Package
CSD	Cambridge Stracture Data
DFTB	Density Functional based Tight binding method
QM	Quantum Mechanical
ONETP	Cadmium Selenide
MM	Molecular Mechanics
QSAR	Quantitative Structure Activity Relationships
Eads	Energy adsorption
KMC	Kinetic Monte Carlo method
LEH	Light Harvesting Efficiency
TS	Light Harvesting Efficiency
FFT	Fast Fourier Transform
LDA	Local Density Approximation
GGA	Generalized Gradient Approximations
B3LYP	Becke3–Lee–Yang–Parr
BFGS	Broyden Fletcher Goldfarb Shanno
DNP	Dynamic Nuclear Polarization
TD-DFT	Time-Dependent Density-Functional Theory
DFT-D	Density Functional Dispersion Correction
GGA-PBE	Generalized Gradient Approximation - Perdew Burke Ernzerhof
BB	Bidentate Bridging
BC	Bidentate Chelating
ME	Monodentate Ester
MO	Metal Oxide
PBE	Perdew Burke Ernzerhof
TPA	Triphenylamine dye
MO	Metal Oxide
MO	Metal Oxide

List of Symbols

η	Efficiency (%)
h	Planck's constant (eV s)
Voc	Open circuit Voltage (V)
Iph	Photocurrent (A)
Isc	Short circuit Current (A)
K_{inj}	Injection rate
K_{reg}	Regeneration rate
ΔG_{ing}	Driving force of electron injection
ΔG_{reg}	Dye regeneration
Λ_{max}	maximum absorption energy of the dye

General Introduction

The solar PV technology research is all about improving the conversion efficiency regardless of the costs, and then, later, try to reduce costs, also search for lowest cost photovoltaic conversion materials and cell constructions, and then, through research, progressively increase the conversion rate. Currently there are three different types of solar cell technologies. First, Crystalline Silicon (c-Si) Solar Cells, the practical limit for c-Si cell efficiency is up 26%. However, to get close to this level of efficiency there is sufficient space for improvement. Most importantly, while c-Si PV technology is the most efficient PV cell compared to other technologies, with an average of 16%-20% efficiency in converting absorbed sunlight into electricity. Secondly, Thin Film Solar Cells (TFSC), which have relatively low efficiencies compared to c-Si cells, with typical efficiencies in the 12%-17% efficiency range. Most TFPV production modules are about 6%-14% efficient. However, there is wide variation in TFPV efficiency, which depends on, whether a cell is "multi-junction" or not. Multi-junction PV cells contain multiple layers of different semiconductor materials, with each layer of material adsorbs a different wavelength of sunlight. Increasing the range of light wavelengths that could increases the amount of solar energy that can be converted into electrical energy. Thirdly, New-Concept of PV Solar Cells such as; wide spectra concentrated PV (CPV), dye sensitized cells (DSC), organic solar cells (OSC) and Perovskite solar cells (PSC), they known also as "third-generation" of solar cells, these types of cells have experienced a low efficiency rate except Perovskite solar cells, which achieved a high efficiency level (up to 21%) during 10 years of developing. In contrast, c-Si cell spent more than 50 years in improving to reach 26% of efficiency. However, all PV cell technologies are still under developing and improving their respective technique levels.
PV Technologies is subjected to these important advancing steps of solar cell technologies: Improve existing processing technologies for first generation c-Si solar cells. Develop new materials for both thin-film and new concept PV technologies. For all the solar cells the basic scientific problems should be focused as follows: inner electric field construction; effective carriers transport mechanism; carriers mobility, lifetime, diffusion length; processing, materials characters, device structures and the controlling of the opto-electric transition; The relationship between the crystal micro-structure and materials performance. Electron excitation, transportation and recombination and optoelectronic excitation dynamics.

Problem statement

Massive efforts have been made for improving the performance of DSSC by means of increasing light harvesting, increasing the electron transport in the conduction band of semiconductor oxide and reducing the interfacial recombination of the charge carriers at the semiconductor oxide and electrolyte interfaces. Both TiO_2 and ZnO nanoparticles have advantages and disadvantages in PCE of DSSC. Therefore, the advantages or ZnO over TiO_2 include the following [1].

1. a direct band gap of approximately 3.37 eV.
2. a higher excitation binding energy (60 meV) compared with (4 meV).
3. Higher electron mobility (200 $cm^3 s^{-1}$) compared with TiO_2 (30 $cm^3 s^{-1}$).

However, previous researches has shown that DSSCs based on ZnO possess lower efficiency than those based on nanocrystalline TiO_2. In addition, a comparison between ZnO and TiO_2 as ETMs in PSCs was made, and it was concluded that the sensitizer such as ($MAPbI_3$ perovskite) was thermally less stable on ZnO than TiO_2 as a result of degradation upon annealing at even low temperatures [2]. The issue is that, one material (TiO_2 or ZnO) shows a disadvantage in DSSC, which counted at same time as an advantage in for DSSC, for example, some sensitizers can achieve high surface area with TiO_2 than ZnO and vice versa, however the electron mobility in ZnO still higher than TiO_2.

Purpose of the research

In order to benefit either TiO_2 and ZnO advantages for DSSC we attempted to combine all properties of each material in one material, $ZnTiO_3$ Perovskite material became a best candidate for this, which can be chemically synthesised by TiO_2 and ZnO as precursors. The objective of our research is to identify the properties of $ZnTiO_3$ Perovskite, some of these properties are as follows:

i) First, the conduction band edge (CBE) of the $ZnTiO_3$ Perovskite should align with the Highest Occupied Molecular Orbital (HOMO) of the dye.

ii) Second, the $ZnTiO_3$ Perovskite must have a high electron mobility to allow electrons flow from excited state of the dye to the conduction band of $ZnTiO_3$ Perovskite, that is depends on many factors, such as the processing method, microstructure, morphology, and defect characteristics and so on.

iii) Third, the $ZnTiO_3$ Perovskite must be sufficiently transparent that the dye layer can absorb as much light as possible to achieve optimal performance.

iv) Fourth, $ZnTiO_3$ Perovskite must have a high surface area with the dye, because the more aggregation of dye on the $ZnTiO_3$ Perovskite surface can improve the light absorption efficiency of the dye, thus improving the power conversion efficiency (PCE) of the cell.

Chapter 1

An introduction to solar cells technologies

1.1 Introduction

Solar cells are a promising and potentially important technology and are the future of sustainable energy for the human civilization. Solar cells are typically named after the semiconducting material they are made of. These materials must have certain characteristics in order to absorb sunlight. Some cells are designed to handle sunlight that reaches the Earth's surface, while others are optimized for use in space. Solar cells can be made of only one single layer of light-absorbing material (single-junction) or use multiple physical configurations (multi-junctions) to take advantage of various absorption and charge separation mechanisms. Solar cells can be classified into first, second and third generation cells. The first generation cells—also called conventional, traditional or wafer-based cells—are made of crystalline silicon, the commercially predominant PV technology that includes materials such as polycrystalline and Monocystalline silicon. Second generation cells are thin film solar cells, which include amorphous silicon, CdTe and CIGS cells and are commercially significant in utility-scale photovoltaic power stations, building integrated photovoltaic or in small stand-alone power system. The third generation of solar cells includes a number of thin-film technologies often described as emerging photovoltaics, most of them have not yet been commercially applied and are still in the research or development phase.
Through chapter one the history of photovoltaic and various technologies of solar cells were discussed. This chapter gives a brief overview of the important concepts and technologies in photovoltaic cells. First, generations of Photovoltaic solar cells, is described in Section 1.2. Next, the basic characteristics of a solar cell are explained in Section 1.3. Finally the efficiencies comparison between solar cells technologies is given in Section **??**.

1.2 Generations of Photovoltaic solar cells

All solar cells require a light absorbing material which is present within the cell structure to absorb photons and generate free electrons via the photovoltaic effect. The photovoltaic (PV) effect is the basis of the conversion of light to electricity in photovoltaic solar cells, Rapid technological developments over the last 20 years coupled with a dramatic decrease in costs of photovoltaic technology have opened the way for large-scale deployment.
There are a wide range of PV cell technologies on the market today, using different types of materials, and an even larger number will be available in the future. PV cell technologies are usually classified into three generations as shown in Figure 1.1. depending on the basic material used and the level of commercial maturity

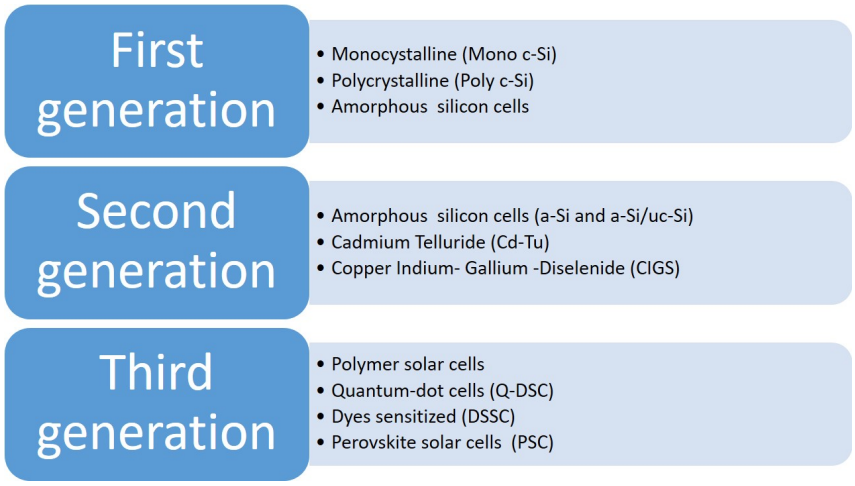

FIGURE 1.1: Classification of solar cells Technologies.

In these next subsections we are going to explain different types of PV technology present today in the world and to provide the achievements in the field of advanced photovoltaic and photo-chemical conversion of solar energy into electricity and methods of selection of PV technology according to different criteria (cost of production, the efficiency of solar energy conversion, and others. . .)
Rapid technological developments over the last 20 years coupled with a dramatic decrease in costs of photovoltaic technology have opened the way for large-scale deployment. There are a wide range of PV cell technologies on the market today, using different types of materials.

1.2.1 First Generation Solar Cell—Silicon Based

The vast majority of today is solar cells are made from silicon and offer both reasonable prices and good efficiency (the rate at which the solar cell converts sunlight into electricity). These cells are usually assembled into larger modules that can be installed on the roofs of residential or commercial buildings or deployed on ground-mounted racks to create huge, utility-scale systems, because of their good performance and stability. Most panels sold on the market come with a warranty of 25 years.
Crystalline silicon cells are classified into three main types depending on how the Si wafers are made. The types are based on the type of silicon used, specifically:

1. Monocrystalline (Mono c-Si)
2. Polycrystalline (Poly c-Si)
3. Amorphous Silicon Cells.

Silicon solar cells typically have two layers: a positive layer (p-type) and a negative layer (n-type). The positive layer is usually made by doping silicon with boron to create extra holes in the silicon valance band, and the negative layer is usually made by doping silicon with phosphorus to have extra electrons available in the silicon conduction band. Working principal for the silicon solar cells is shown in Figure 1.2.

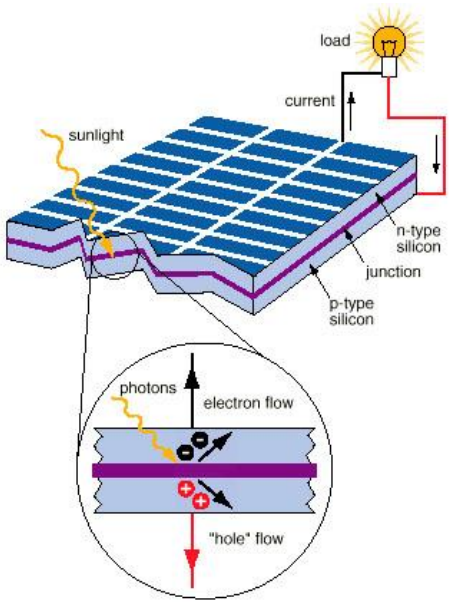

FIGURE 1.2: Schematic of the basic structure of a silicon solar cell.

1.2.1.1 Single/Mono-Crystalline Silicon Solar Cell

Monocrystalline silicon is the base material for silicon chips used in virtually all electronic equipment today. Mono-Si also serves as photovoltaic, light absorbing material in the manufacture of solar cells. It consists of silicon in which the crystal lattice of the entire solid is continuous, unbroken to its edges, and free of any grain boundaries. Mono-Si can be prepared intrinsic, consisting only of exceedingly pure silicon, or doped, containing very small quantities of other elements added to change its semiconducting properties. Most silicon mono-crystals are grown by the Czochralski process into ingots of up to 2 meters in length and weighing several hundred kilogrammes [3]. The efficiency of mono-crystalline single-crystalline silicon solar cells lies between 1% - 25% [4].

1.2.1.2 Polycrystalline Silicon Solar Cell (Poly-Si or Mc-Si)

Figure 1.3 shows Polycrystalline silicon, also called polysilicon or poly-Si, is a high purity, polycrystalline form of silicon, used as a raw material by the solar photovoltaic and electronics industry. Polycrystalline solar cells are also made from silicon. However, instead of using a single crystal of silicon, manufacturers melt many fragments of silicon together to form the wafers for the panel.. The processing of polycrystalline Si solar cells is more economical, which are produced by cooling a graphite mould filled containing molten silicon. Polycrystalline Si solar cells are currently the most popular solar cells. Though they are slightly cheaper to fabricate compared to Monocystalline silicon solar panels, yet are less efficient 12% - 17% [5].

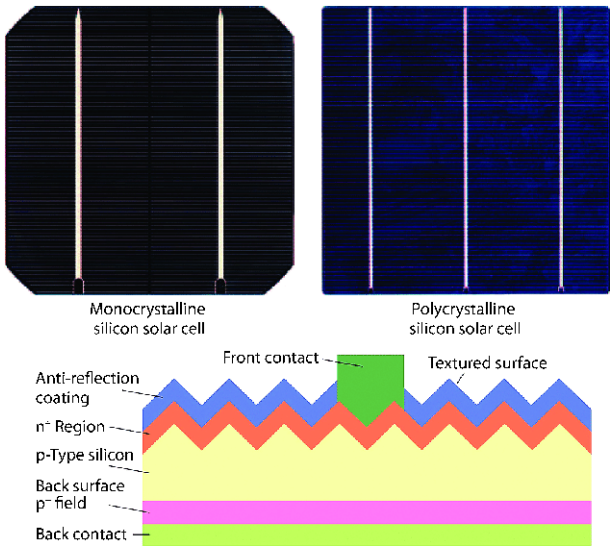

FIGURE 1.3: Typical mono and polycrystalline silicon solar cells top and simplified cross section.

1.2.1.3 Amorphous Silicon Solar Cell (A-Si)

Amorphous silicon (a-Si) is the non-crystalline form of silicon. It is the most well developed of the thin film technologies having been on the market for more than 15 years. It is widely used in pocket calculators, but it also powers some private homes, buildings, and remote facilities. Amorphous silicon cells are formed by vapor-depositing a thin layer of silicon material – about 1 micrometer thick – on a substrate material such as glass or metal.
Amorphous silicon can also be deposited at very low temperatures, as low as 75 degrees Celsius, which allows for deposition on plastic as well. In its simplest form, the cell structure has a single sequence of p-in layers. However, single layer cells suffer from significant degradation in their power output (in the range 15-35%) when exposed to the sun. The mechanism of degradation is called the Staebler-Wronski Effect [6], after its discoverers. Better stability requires the use of a thinner layers in order to increase the electric field strength across the material.The thickness of the solar cell is just 1 micron, or about 1/300th the size of mono-crystalline silicon solar cell.

The low efficiency rate is partly due to the Staebler-Wronski effect, which manifests itself in the first hours when the panels are exposed to sunlight, and results in a decrease in the energy yield of an amorphous silicon panel from 10% to around 7%. The principal advantage of amorphous silicon solar cells is their lower manufacturing costs, which makes these cells very cost competitive.

1.2.1.4 Crystalline Versus Amorphous Silicon Solar Cells

There are numerous advantages and disadvantages for each class of silicon solar cell. Higher efficiency and stability alongside the higher manufacturing costs of mono-crystalline silicon solar cell devices make them suitable for use in space. Whereas multi-crystalline cells with slightly lower efficiencies but more affordable prices increase their popularity for the use in terrestrial applications. Amorphous cells are considerably behind the previous classes of silicon solar cells in terms of efficiency, but their much cheaper and simpler fabrication methods will allow for easier large-scale implementation and potential to rival costs of fossil fuels. A range of silicon solar cells and their module efficiencies are tabulated in Table 1.1 These results emphasize the difference in efficiencies across the range of different classes of silicon solar cells [7].

TABLE 1.1: Confirmed terrestrial module efficiencies under the global AM1.5 spectrum (1000 W/ m2) at a cell temperature of 25 °C

Classification	**Eff. (%)**	**Area(cm2)**	**VOC(V)**	**JSC (mA/ cm2)**	**FF**	**Test centerd (date)**
Si (thin-film a-Si)	2.4	3.5	0.8	22	<45	RCA (2/76)
Si (thin-film a-SiC:H/a-Si: H)	8	1	0.88	15.2	62	Osaka (1/82)
Si (c-PERC cell)	22.8	0.2	0.7	40.3	81	SPL-JMRC (9/89)
Si (c-PERL cell)	24.2	4	0.7	42.9	81	SNL (8/90)
Si (a-Si:H)	8.9	1	0.85	16.1	65	Sanyo (/97)
Si (a-Si:H)	9.2	0.25	0.95	15	64	USSC (11/98)
Si (c-PERL cell)	24.4	4	0.7	42	84	SNL (10/98)
Si (mc-Si)	19.8	1	0.65	38.1	80	SNL (10/98)
Si (c-PERL FZ)	24.7	4	0.71	42.2	83	SNL (10/99)
Si (amorphous)	9.5	1	0.86	17.5	63	NREL (4/03)
Si (mc-Si)	20.4	1	0.66	38	81	NREL (5/04)
CIGS	19.9	0.4	0.69	35.5	81	NREL (11/07)
Si (a-20 µm nanowire)	5.3	0.002	0.52	16.8	61	California (1/10)
Si (mc-Si)	18.5	14,66	–	–	76	FhG-ISE (1/12)
Si (mc-Si))	20.8	243.9	0.66	39	80	TrinaSolar (11/14)
Si (amorphous)	10.2	1	0.89	16.3	70	AIST (7/14)
Si (c-HIT®)	25.6	143.7	0.74	–	83	Panasonic (4/14)

1.2.2 Second Generation Solar Cells—Thin Film

Another commonly used photovoltaic technology is known as thin-film solar cells because they are made from very thin layers of semiconductor material. Most of the thin film solar cells and a-Si are second generation solar cells, and are more economical as compared to the first generation silicon solar cells. Silicon-wafer cells have light absorbing layers up to 350 µm thick, while thin-film solar cells have a very thin light absorbing layers, generally of the order of 1 µm thickness [8]

1.2.2.1 Amorphous Silicon Thin Film (a-Si) Solar Cell

Amorphous Si (a-Si) PV modules are the primitive solar cells that are first to be manufactured industrially. Amorphous (a-Si) solar cells can be manufactured at a low processing temperature, thereby permitting the use of various low cost, polymer and other flexible substrates. These substrates require a smaller amount of energy for processing [9]. These solar cells generally are dark brown in color on the reflecting side while silverish on the conducting side [10]. The main issue of a-Si solar cell is the poor and almost unstable efficiency. The cell efficiency automatically falls at PV module level. Currently, the efficiencies of commercial PV modules vary in the range of 4% - 8%. They can be easily operated at elevated temperatures, By 2014, efficiencies only increased to 10.2%, confirming the difficulties that amorphous silicon cells have in achieving good cell efficiency and are suitable for the changing climatic conditions where sun shines for few hours [11].

1.2.2.2 Cadmium Telluride (CdTe) Thin Film Solar Cell

Among thin-film solar cells, cadmium telluride (CdTe) is one of the leading candidate for the development of cheaper, economically viable photovoltaic (PV) devices, and it is also the first PV technology at a low cost [4] [12] [13]. CdTe has a band gap of 1.5 eV as well as high optical absorption coefficient and chemical stability. These properties make CdTe most attractive material for designing of thin-film solar cells.
Therefore, its efficiency usually operates in the range 9% - 11% [4] [14]. CdTe solar cells can be made on polymer substrates and flexible. However, there are various environmental issues with cadmium component of solar cell. Cadmium is regarded as a heavy metal and potential toxic agent that can accumulate in human bodies, animals and plants. The disposal of the toxic Cd based materials as well as their recycling can be highly expensive and damaging too to our environment and society [15].

1.2.2.3 Copper Indium Gallium Di-Selenide (CIGS) Solar Cells

CIGS is a quaternary compound semiconductor comprising of the four elements, namely: Copper, Indium, Gallium and Selenium [15] [16]. CIGS are also direct band gap type semiconductors. Compared to the CdTe thin film solar cell, CIGS hold a higher efficiency 10% - 12%. Due to their significantly high efficiency and economy, CIGS based solar cell technology forms one of the most likely thin film technologies. The processing of CIGS are done by the following techniques: sputtering, evaporation, electrochemical coating technique, printing and electron beam deposition [3] [17].The substrates for CIGS material can be chosen from glass plate, polymers substrates, steel, aluminium etc. The advantages of CIGS thin film solar cells include its prolonged life without a considerable degradation. These properties of CIGS indicate an easy solution to enhance the efficiency [9].

1.2.3 Third Generation Solar Cells

A third type of photovoltaic technology is named after the elements that compose them, which are the new promising technologies but are not commercially investigated in detail. Most of the developed 3rd generation solar cell types arr [18]:

1. Polymer based solar cells.
2. Quantum-dot solar cells.
3. Dye sensitized solar cells.
4. Perovskite solar cells.

1.2.3.1 Polymer based solar cells

Polymer solar cells (PSC) are generally flexible solar cells due to the polymer substrate. It works usually as a combination of donor (polymer) and a acceptor (fullerene). There are various types of materials for the absorption of sunlight, including organic material like a conjugate/conducting polymer [19] [20]. The PSC and other organic solar cells operate on same principle known as the photovoltaic effect, i.e., where the transformation of the energy occurs in the form of electromagnetic radiations into electrical current [21] . This process triggered the development of a new age in the polymer materials for capturing the solar power. After significantly optimizing the parameters, researchers achieved efficiency over 3% for PPV type PSCs [22]. Polymer solar cells include organic solar cells (also called "plastic solar cells"). They are one type of thin film solar cell, which most organic solar cells are polymer solar cells. Figure 1.4

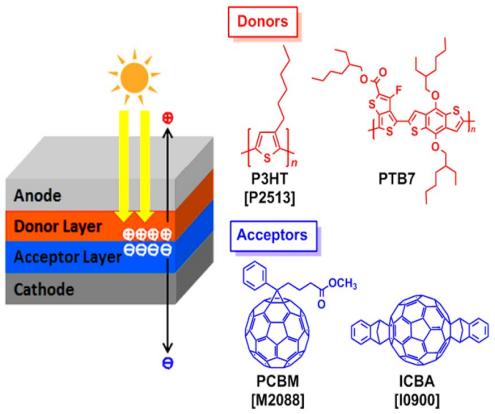

FIGURE 1.4: Polymer based solar cells structure.

1.2.3.2 Quantum Dot Solar Cell

A quantum dot solar cell, (Figure 1.5) is a solar cell design that uses quantum dots as the absorbing photovoltaic material also known Nanocrystal based solar cells. It attempts to replace bulk materials such as silicon, copper indium gallium selenide (CIGS) or CdTe. Quantum dots have band gaps that are tenable across a wide range of energy levels by changing the dots' size. In bulk materials the band gap is fixed by the choice of material(s). This property makes quantum dots attractive for multi-junction solar cells, where a variety of materials are used to improve efficiency by harvesting multiple portions of the solar spectrum [23].

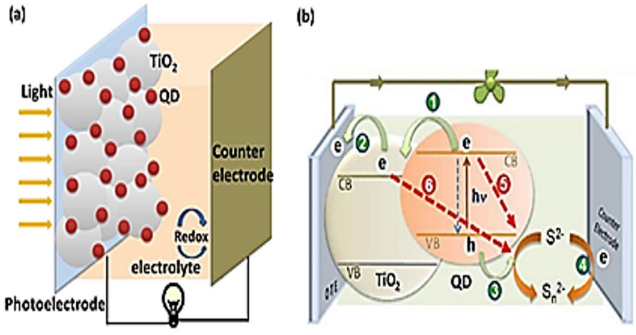

FIGURE 1.5: Representation diagram of the structure of a QDSC; and (b) representation diagram of photo induced charge transfer process..

1.2.3.3 Dye-Sensitized Solar Cell (DSSC)

Recent research has been focused on improving solar efficiency by molecular manipulation, use of nanotechnology for harvesting light energy [24]. The first DSSC solar cell was introduced by Michel Grätzel in Swiss federal institute of technology [15] . DSSCs based solar cells generally employ dye molecules between the different electrodes. The DSSC device consists of four components: semiconductor electrode (n-type TiO_2 and p-type NiO), a dye sensitizer, redox mediator, and a counter electrode (carbon or Pt) [40]. The DSSCs attractive due to the simple conventional processing methods like printing techniques, are highly flexible, transparent and low cost as well [15] . The novelty in the DSSC solar cells arise due to the photosensitization of nano grained TiO_2 coatings coupled with the visible optically active dyes, thus increasing the efficiencies greater than 10% [25]. However, there are certain challenges like degradation of dye molecules and hence stability issues [15].

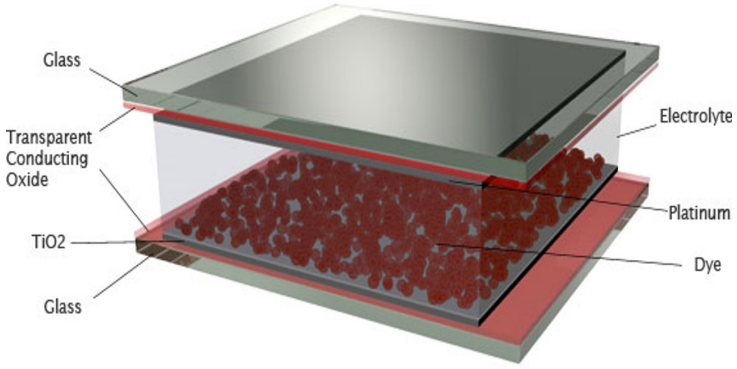

FIGURE 1.6: The structure of Dye-Sensitized Solar Cells.

1.2.3.4 Perovskite Solar Cell

The name 'perovskite solar cell' is derived from the ABX_3 structure of the absorber materials, which is referred to as perovskite structure. The most commonly studied perovskite absorber is methyl ammonium lead trihalide (CH3NH3PbX3), where X is a halogen ion such as I, Br, Cl), with an optical bandgap between 2.3 eV and 1.6 eV depending on halide content [26]. Perovskite solar cells (Figure 1.7)hold an advantage over traditional silicon solar cells in the simplicity of their processing.
Traditional silicon cells require expensive, multistep processes requiring high temperatures (upwards of 1000 °C) and vacuums in special clean room facilities to produce high purity silicon wafers [27]. These techniques are harder to scale up, while the

organic-inorganic perovskite material can be manufactured with simpler wet chemistry and processing techniques in a traditional lab environment [28]. Previously whenever a new material was discovered it had taken some 10-20 years of research to reach an efficiency rate of even 10%. Perovskite solar cells only emerged in 2012, but have already clocked up conversions of more than 19% efficiency [29].

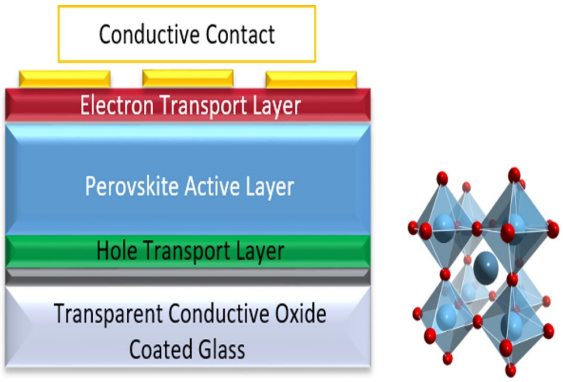

FIGURE 1.7: Perovskite Solar Cells structure..

1.3 Solar Cell IV-Characteristics

The main electrical characteristics of a photovoltaic cell is summarized in an IV curve. An IV curve is depicted in Figure 18 where the current (I) is plotted against voltage (V). The amount of power (P) the cell produces is given by the following equation:

$$P = I * V \tag{1.1}$$

If the cell is short-circuited, when no external load is connected, the device will experience its highest current (ISC). Voltage will then equate to zero. If the cell is disconnected from the outer circuit, the open voltage circuit (VOC) will be the potential between the two terminals. In this condition the current is zero. In both of the extremes, ISC and VOC, no power will be produced. In between these two points there is a combination of current and voltage where maximum power is produced. This is called the "maximum power point", or MPP (Pmp). The MPP has a corresponding current (Imp) and voltage (Vmp). The cell's Fill Factor (FF) can be calculated [30] using:

$$FF = \frac{I_{mp}.Vmp}{I_{sc}.V_{oc}} = \frac{P_{pm}}{I_{sc}.V_{oc}} \tag{1.2}$$

FF is the ratio of the theoretical power output if ISC and VOC could occur at the same time, compared to the actual power output. Graphically it is indicated in how rectangular shaped the IV-curve is in Figure 18. A large FF is preferable, but it can never exceed 1 [31], and will normally be in the range between 0.5 and 0.83 [51]. The most commonly used parameter to describe a cell is the efficiency, which is the conversion ratio of the power produced to the incoming power [32].

$$\eta = \frac{P_{mp}}{P_{in}} = \frac{FF.I_{sc}.V_{oc}}{P_{in}} \tag{1.3}$$

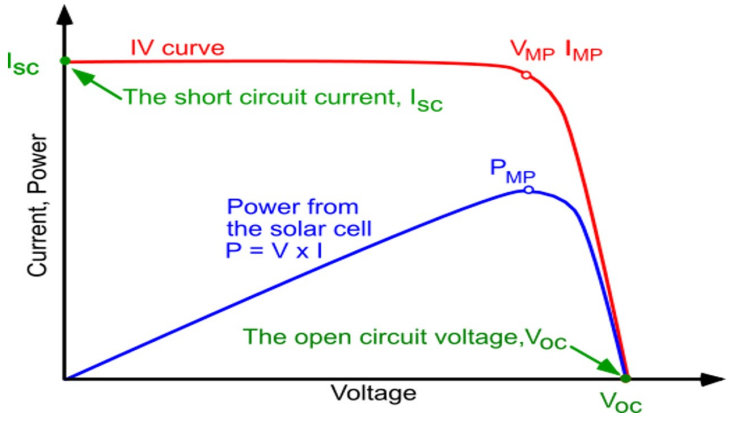

FIGURE 1.8: An IV curve provides information concerning the characteristics of a photovoltaic cell. Isc and Voc are the short current and open circuit respectively. Imp and Vmp are the points where the cell produces the maximum. power Pmp.

1.4 Fundamental limits to solar energy conversion

The maximum efficiency one can reach with the conventional solar cell structure is given by the so-called single material or Shockley-Queisser limit. Using a detailed balance approach and assuming that each photon above the band-gap gives rise to just one electron-hole pair, while all photons with energy below the band-gap are lost, one comes to a theoretical maximum energy conversion efficiency of about 30% for Si. This is relatively low, mainly because of the thermalisation and transmission losses, which account for about 56% loss of photon energy [33].

These losses result from a single energy band gap, Eg, being used to convert a wide range of solar energy photons. This is demonstrated in Figure 1.9. The photon energy is given by (hv) where (h) is Planck's constant and (v) is the frequency of the photon. Red photons, having energy lower than the band-gap energy, i.e., (h < Eg), are not absorbed in the material. Thus this part of the solar spectrum cannot be converted into

electricity and represents a transmission loss. The high energy photons having energy higher than the band-gap energy, i.e., (h > Eg), get absorbed in the material. In this case, a part of the photon energy is used to excite electrons across the band-gap, (Eg), giving rise to its potential energy while the energy difference, (h – Eg), increases the kinetic energy of the electrons. Electrons with high kinetic energy are referred to as "hot" electrons. Electrons lose their kinetic energy in the form of heat due to lattice scattering. In order to make more effective use of the solar spectrum. Different concepts have been proposed to overcome the Shockley-Queisser limit of light conversion efficiency. The concepts are based on splitting of the sun's spectrum to be absorbed by many cells (e.g., multijunction solar cells, intermediate band solar cells, quantum well solar cells), reduction in thermalisation losses (e.g., hot carrier cells), or adapting the solar spectrum to one host material (e.g., up- and down-conversion of photon energy)[33].

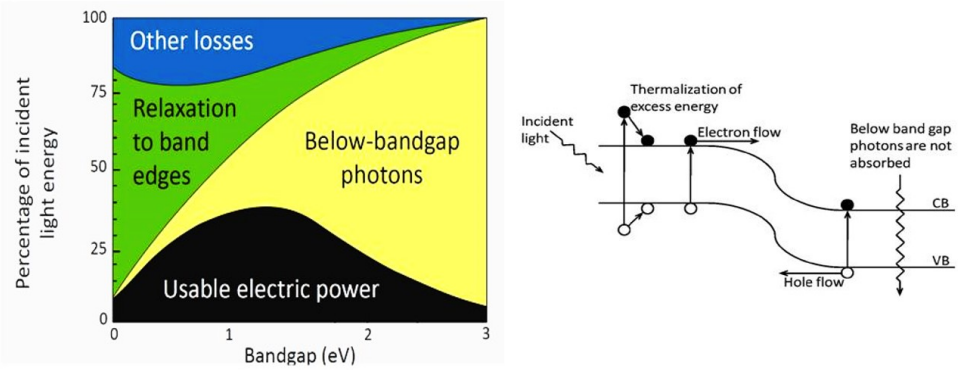

FIGURE 1.9: The Shockley-Queisser limit in Photovoltaic.

1.5 Solar cell efficiency tables (Version 56)

Since January 1993, "Progress in Photovoltaics" has published six monthly listings of the highest confirmed efficiencies for a range of photovoltaic cell and module technologies. By providing guidelines for inclusion of results into these tables and also encourages researchers to seek independent confirmation of results and to report results on a standardised basis[34]. Consolidated table 1.2 showing an extensive listing of the highest independently confirmed efficiencies for solar cells and modules are presented. Guidelines for inclusion of results into these tables are outlined, and new entries since January 2020 are reviewed.

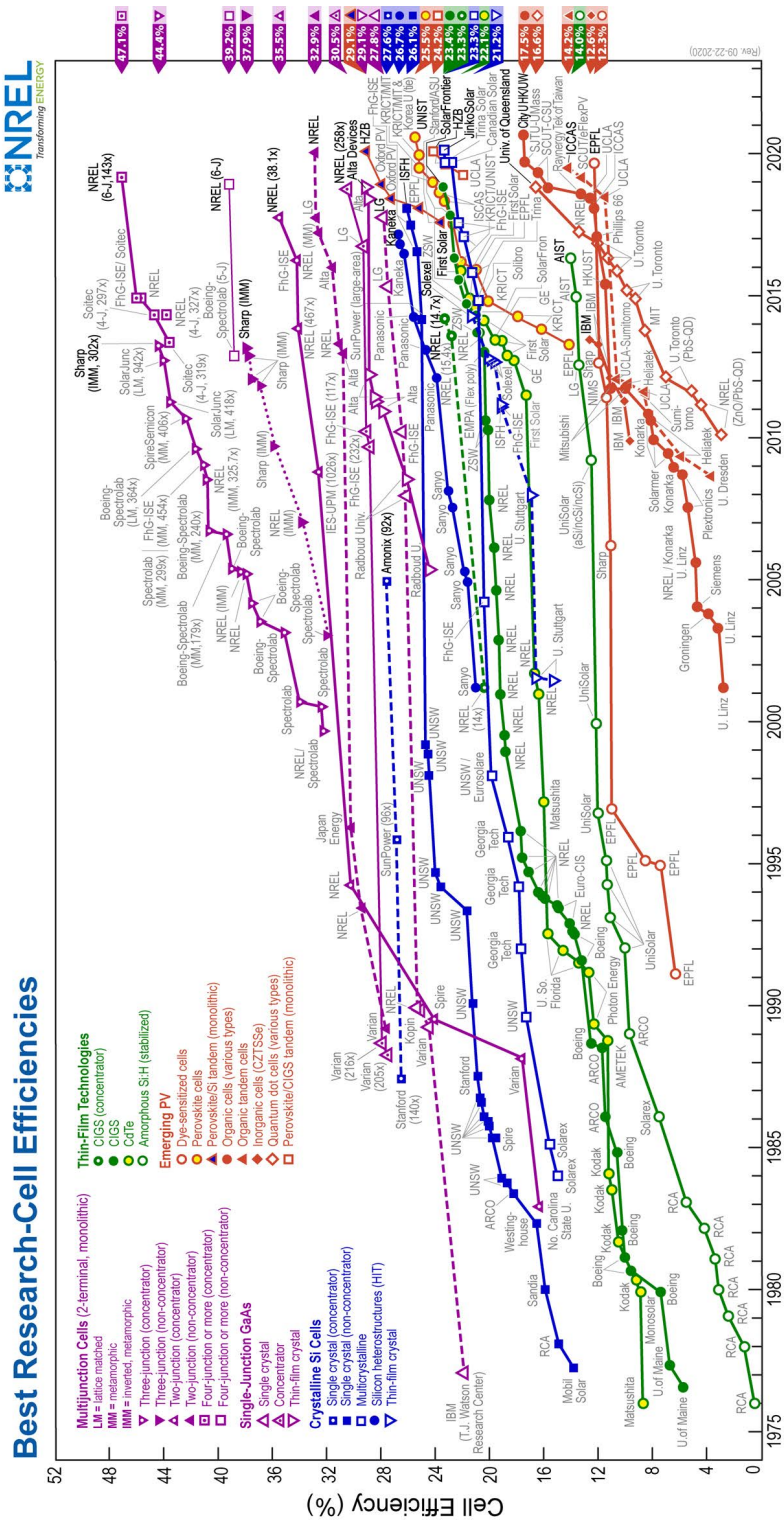

FIGURE 1.10: Research efficiencies of different solar cell technologies,from 1976 to the present. "This plot is courtesy of the National Renewable Energy Laboratory, Golden, CO.

TABLE 1.2: Confirmed single-junction terrestrial cell and submodule efficiencies measured under the global AM1.5 spectrum (1000 W/m2) at 25°C (International Electrotechnical Commission [IEC] 60904-3: 2008, ASTM G-173-03 global).

Classification	Efficiency (%)	Area (cm2)	Voc (V)	Jsc (mA/cm2)	Fill factor	Test Centre (date)
Silicon						
Si-Crystalline cell	26.7 ± 0.5	79.0 (da)	0.738	42.65a	84.9	AIST (3/17)
Si (DS wafer cell)	23.8 ± 0.3	246.44 (t)	0.7087	40.88 b	82.2	ISFH (12/19)
Si (thin transfer submodule)	21.2 ± 0.4	239.7(ap)	0.687c	38.50c,d	80.3	NREL (4/14)
Si (thin-film minimodule)	10.5 ± 0.3	94.0 (ap)	0.492c	29.7c,e	72.1	FhG-ISE (8/07)
III–V cells						
GaAs-thin film	29.1 ± 0.6	0.998 (ap)	1.1272	29.78f	86 .7	FhG-ISE (10/18)
GaAs (multicrystalline)	18.4 ± 0.5	4.011 (t)	0.994	23.2	79.7	NREL (11/95)
InP-crystalline	24.2 ± 0.5[g]	1.008 (ap)	0.939	31.15a	82.6	NREL (3/13)
Thin-film chalcogenide						
CIGS (cell)	23.35 ±0.5	1.043 (da)	0.734	39.58h	80.4	AIST (11/18)
CdTe (cell)	21.0 ± 0.4	1.0623(ap)	0.8759	30.25d	79.4	Newport (8/14
CZTSSe (cell)	11.3 ± 0.3	1.1761(da)	0.5333	33.57f	63.0	Newport,(10/18)
CZTS (cell)	10.0 ± 0.2	1.113 (da)	0.7083	21.77a	65.1	NREL (3/17)
Amorphous/microcrystalline						
Si-amorphous cell	10.2±0.3[i,g]	1.001 [(da)]	0.896	16.36[d]	69.8	AIST (7/14)
Si(microcrystalline cell)	11.9 ± 0.3[g]	1.044 [(da)]	0.550	29.72[a]	75.0	AIST (2/17)
Perovskite						
Perovskite (cell)	21.6±0.6[j,k]	1.0235 [(da)]	1.193	21.64[l]	83.6	CSIRO (6/19)
Perovskite (minimodule)	18.0±0.6[j,m]	19.276[(da)]	1.070c	21.53[c,b,n]	78.4	Newport (12/19)
Dye sensitised						
Dye (cell)	11.9 ± 0.4[o]	1.005 [(da)]	0.744	22.47[p]	71.2	AIST (9/12)
Dye-minimodule	10.7±0.4[o]	26.55 [(da)]	0.754[c]	20.19[c,q]	69.9	AIST (2/15)
Dye-submodule	8.8 ± 0.3[o]	398.8 [(da)]	0.697[c]	18.42[c,r]	68.7	AIST (9/12)
Organic						
Organic (cell)	13.45±0.2[s]	1.023 [(da)]	0.8422	23.28l	68.6	FhG-ISE (6/19)
Organic (minimodule)	12.6 ± 0.2[s]	26.129[(da)]	0.8315[c]	21.32[c,l]	71.1	FhG-ISE (9/19)
Organic (submodule)	11.7 ± 0.2[s]	203.98 [(da)]	0.8177[c]	20.68[c,l]	69.3	FhG-ISE (1/19)

1.6 Conclusion

Monocrystalline and polycrystalline silicon solar cells are the most common PV technology in use today. Monocrystalline solar cells have higher efficiency due to less lattice imperfection, but also higher production costs than polycrystalline silicon cells. Both cells are produced from silicon, a material that is one of the most abundant in the earth's crust. According to NREL's efficiency chart (Figure 2.4) the current record efficiencies are 23.8% for polycrystalline silicon solar cell and 26.7% for mono-crystalline silicon solar cell.
Thin-film solar cells can be flexible and lightweight, making them ideal for portable applications—such as in a soldier's backpack—or for use in other products like windows that generate electricity from the sun with an efficiency u to 23.35%. Some types of thin-film solar cells also benefit from manufacturing techniques that require less energy and are easier to scale-up than the manufacturing techniques required by silicon solar cells. New approaches and concepts of nanotechnology may also improve the multiple junction devices by controlling the growth, band structures and defects. Currently solar energy is expensive source of energy but with use of multi junction high efficiency solar cells with innovative concepts can accelerate the field of photovoltaic.
There are several new solar cell concepts that aim at making better use of the solar spectrum and by doing so the target is to achieve much higher energy conversion efficiencies than in the present conventional solar cells such as nanotechnology approaches. The only concept that has demonstrated higher efficiency 30% in practice so far is the multi-junction solar cell based on InGaP, GaAs and Ge materials. Multi-junction cells are presently used in space applications and are being introduced for terrestrial concentration systems.
Other concepts like the Organic cells, dye sensitizer solar cells, Perovskite cells, and quantum dot cells are presently at the stage of research and development in term of efficiency and stability, but might lead to very high solar cell efficiency at lower cost in future. In next chapter we focus and discuss more about Dye sensitizer solar cells-DSSC technology, in term of research and developments on structures and efficiencies, this type of solar cell is completely different on work principal compared to conventional solar cells technology, excitation and transportation of electrons in silicon cells occurs in one material. In contrast, in DSSC both phenomenal execute in different materials and layers in the structure.

Chapter 2

Dye Sensitized Solar Cells: Fundamentals and Current Status

2.1 History of DSSC

The history of dye sensitized solar cell started in 1972, when a researcher published an article was where chlorophyll had been sensitized to ZnO [35]. The article explained how it was possible to generate electricity, through letting electrons being excited by photons in the dye molecules and transferring them to external circuit via the semiconductor. This work made a big interest in the research community. As a direct consequence after couple years saw a strong increase in research on ZnO single-crystals [36]. Despite massive of research being investigated during the early period of DSSC, the efficiency at that time was impoverished to 1%. This was mainly due to the low surface area of ZnO. The amount of dye adsorbed to the surface was thus low, and as dye is responsible for the light harvesting, very small amounts of sun was harvested. The problem of low efficiency remained until the introduction of porous TiO2, which with a much higher surface area allowed for absorption of a higher amount of dye. A major development was made by Grätzel and O'Regan, who in 1991 used this semiconductor to produce a cell with 7.9% efficiency [37]. This is known to be the first version of the DSSC we have today, and it is sometimes referred to as the Grätzel cell in honour of its inventor. After several years Michael Grätzel and his group were able to demonstrate the first 10% efficient cells certified by NREL in USA. Recently, commercial applications of the DSSC have been under intensive investigation. The cost of commercially fabricating DSSCs is expected to be relatively low because the cells are made of low-cost materials and assembly is simple and easy.

2.2 Structure of standard DSSC

The DSSC can be described as an electrochemical cell, which consists of an anode (named photoanode), an electrolyte and a cathode. An illustration of the whole cell is depicted in Figure 2.1. The photoanode consists of four main components, namely glass, FTO, semiconductor and dye, it is clear how glass act as the foundation of the cell. Directly on top of the glass, there are a thin layer of a transparent conductive film, commonly named FTO (Fluorine-Tin-Oxide) or ITO (Indium-Tin Oxide) which will be described in Section 2.4.1. The semiconductor can be divided in different layers, which all serves different functions. These functions are all thoroughly explained in Section 2.4.2. In order to ensure a high surface area, it is of great importance that the semiconductor is made of a porous material. The semiconductor most typically used for this purpose is TiO_2 (Titanium Oxide). The dye it can be seen adsorbed onto the semiconductor. In order for the dye to be well-functioning, the dye needs to hold specific properties, which will be sufficiently described in Section 2.4.3. Percolating between the pores in the semiconductor is the electrolyte which is described in Section 2.4.4. A typical cathode consists of the same FTO and glass as the anode, with the addition of a layer of platinum. The platinum works as a catalyst to increase the electron rate between the FTO and electrolyte. The pathway of electrons in DSSC is shown by the arrows in 2.2.

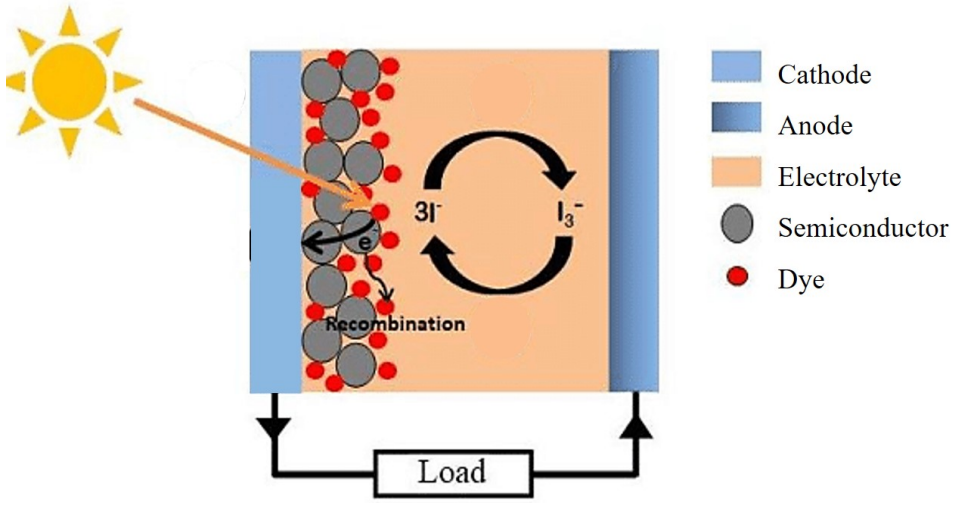

FIGURE 2.1: the structure of DSSC.

2.3 Types of Dye-Sensitized Solar Cells (DSSCs)

2.3.1 N-Type dye-sensitized solar cells (n-type DSSCs)

In an n-type DSSC, which contains a photoactive anode and a passive cathode, an electron is injected from the excited dye to the conduction band of the n-type semiconductor.

2.3.1.1 Working Principles of n-type DSSCs

The working principle of DSSCs involves some key processes, light absorption, charge separation and charge collection. The mechanism of the DSSC is as follows.

- The dye serves to harvest the solar light and generate the electrons.
- Electrons are injected into the conduction band of semiconductor (TiO_2)
- Electrons travels through the nanoparticle (TiO_2) network and collected by the
- Then the electron subsequently passes through the external circuit, performs the electrical work and moves to the cathode (Pt)
- Meanwhile the dye injects holes to the whole conductors and transport to the counter electrode with the outside circuit which finishes the loop.

As long as the DSSC device being exposed under illumination the cell keep repeating the mechanism and producing electricity and sunlight.

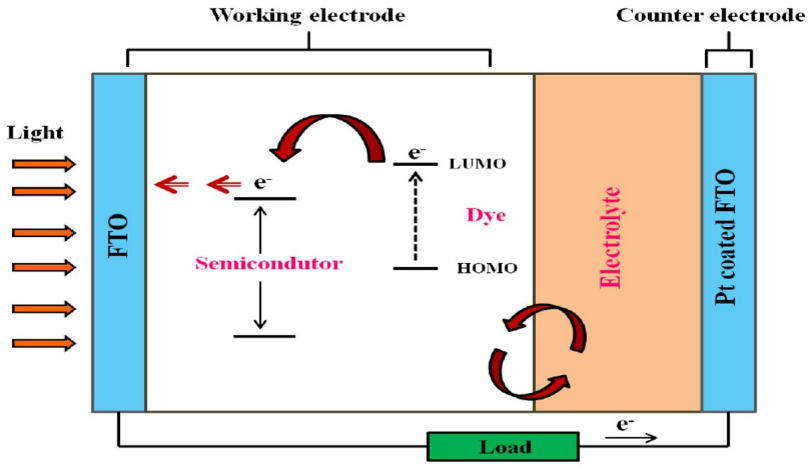

FIGURE 2.2: Schematic illustration of the working principle of n-type DSSC.

A similar DSSC as was portrayed in 2.2 is depicted. This figure 2.3 shows the energy levels of the electrons when they go through the electrolyte, dye and semiconductor. The green arrows illustrate the desired pathway of the electrons, while the purple arrows shows the recombination possibilities.

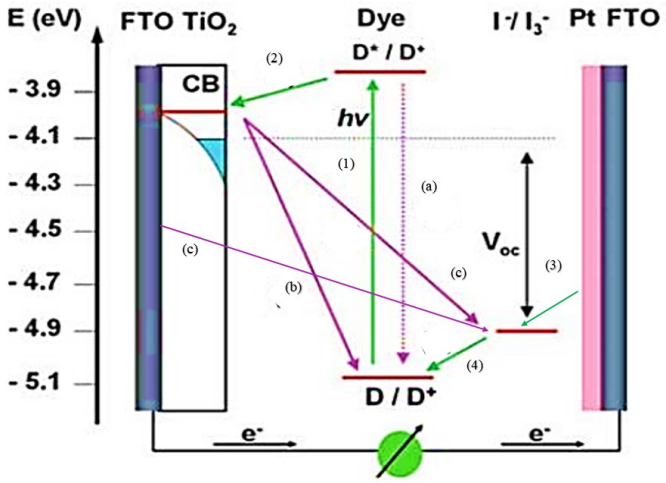

FIGURE 2.3: Overview of kinetics of electron transfer process in DSSC.

The dye will absorb a photon, lifting an electron from the valence band (UOMO) to the conduction band (LUMO), and therefore go from a ground state (D) to the excited state (D*). This process is described by (equation 2.1) and depicted as number (1) in Figure 2.3. The lifetime of the excited state is in the order of nanoseconds, before the electron will relax back into ground state. However, the electron do not normally relax back into ground state, as it will instead fall into the CB of the semiconductor within picoseconds number (2) in Figure 2.3) . This leaves the dye oxidized (equation 2.2). The electron will pass through the conduction band of porous semiconductor and then travel through the external circuit and regenerate the electrolyte at the surface of the cathode. This process is described by (equation 2.3) and depicted as number (3) in Figure 2.3. The electrolyte will then regenerate the oxidized dye as described by (equation 2.4) and depicted as number (4) in Figure 2.3 [38].

$$D + hv \rightarrow D^* \tag{2.1}$$

$$D^* \rightarrow D^+ + e^-_{Tio_2} \tag{2.2}$$

$$I_3^- + 2e^-_{cathode} \rightarrow 3I^- \tag{2.3}$$

$$D^+ + \frac{3}{2}I^- \rightarrow D + \frac{1}{2}I^- \tag{2.4}$$

Equations (2.1) to (2.4) shows the desired direction of the electron flow. There are other possible ways for the electron to go, which would decrease the overall efficiency of the cell. These are portrayed as purple dotted arrows in Figure 2.3. One of these is the excited electron returning to a higher state in the dye (HUMO), before it is able to transfer to the CB of the semiconductor:

$$D* + e^-_{excited} \rightarrow D \tag{2.5}$$

A second recombination path is when the electron in the semiconductor recombines with the oxidized dye:

$$e^-_{Tio_2} + D^+ \rightarrow D \tag{2.6}$$

A third possible recombination occurs if the electron in the semiconductor recombines with the electrolyte:

$$e^-_{Tio_2} + E^+ \rightarrow E \tag{2.7}$$

A fourth recombination path is when the electron in the FTO recombines with the electrolyte:

$$e^-_{FTO} + E^+ \rightarrow E \tag{2.8}$$

It has been noted by Gregg et al [38]. That considering equation (2.7), it is strange that the cell can work at all. The electron have to diffuse through the $10\mu m$ -layer of porous TiO_2. This will take some time, as the average transit time is 10ms. During this time the electron is only a few nanometers away from the electrolyte. Since the recombination rate of equation (2.7) is extremely slow, the cell still work. The V_{OC} is determined by the difference between the Fermi level of the semiconductor and the red-ox potential of the electrolyte. The I_{SC} is determined by the amount of adsorbed dye molecules, light harvesting and excited electrons ability to diffuse through the semiconductor and go through the external circuit.

2.3.2 P-Type dye-sensitized solar cells (p-type DSSCs)

The p-type DSSC is a sandwich structured device composed of a photoactive working electrode (cathode), a passive counter electrode (anode), and redox electrolyte (as shown in Figure 2.5. The main components are: 1) a fluorine-doped SnO_2 (FTO) glass substrate, 2) a nanostructured p-type semiconductor layer, 3) a light-absorbing layer, normally the dye, 4) a platinized (Pt) conducting glass counter electrode, and 5) the electrolyte. In our case, the p-type semiconductor is nickel oxide (NiO), which has a band gap of 3.6 eV and has the advantage of good stability and transparency. The electrolyte is a liquid system containing the iodide/triiodide redox couple

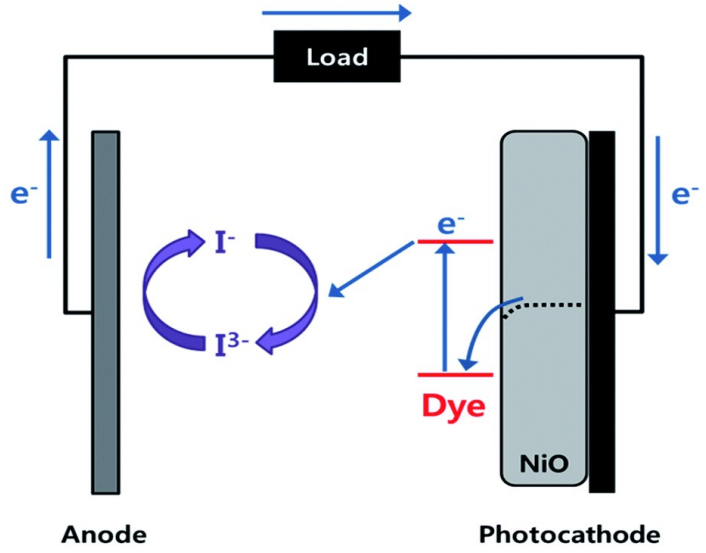

FIGURE 2.4: Schematic illustration of p-type DSSC.

2.3.2.1 Working Principles of p-type DSSCs

In p-type DSSCs, visible light absorption by the dye is followed by electron transfer from the valence band of the semiconductor to the dye (or, in other words, whole injection from the dye to the valence band of the semiconductor). The dye is then regenerated by electron transfer from the reduced dye to the oxidized species (I_3^-) in the electrolyte (see Figure 2.5) . If the reduced dye cannot react with the electrolyte within the charge-separated lifetime, it may recombine with the hole in the semiconductor (geminate recombination). The holes in the semiconductor move to the back collector of the working electrode and the reduced species (I^-) in the electrolyte diffuses to the (Pt) electrode. This charge collection gives rise to a cathodic photo-current in the external circuit.

$$Dye|NiO + hv \rightarrow Dye^*|NiO \qquad (excitation) \tag{2.9}$$

$$Dye^*|NiO \rightarrow Dye^-|NiO + h + (NiO) \qquad (hole - injection) \tag{2.10}$$

$$Dye^-|NiO + h(NiO) \rightarrow Dye|NiO \qquad (geminate - recombination) \tag{2.11}$$

$$Dye^-|NiO + 1/2I_3^- \rightarrow Dye|NiO + 3/2I^- \qquad (dye - generation) \tag{2.12}$$

$$3/2I^- \rightarrow 1/2I_3^- + e - (Pt) \qquad (regeneration of I_3 - at the counter electrode) \tag{2.13}$$

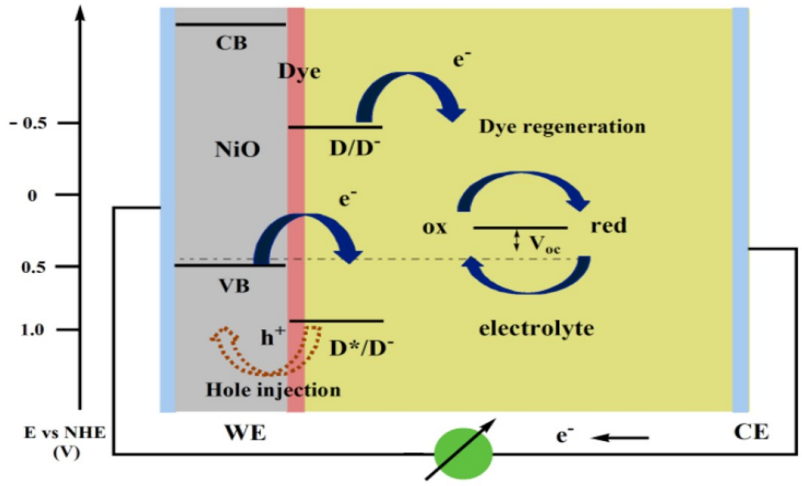

FIGURE 2.5: Schematic illustration of working principle of p-type DSSC.

2.4 Components of dye-sensitized solar cells

As mentioned previously in Section 2.2, DSSC consists of four principal component, an anode (named photoanode), a dye sensitizer, an electrolyte and a cathode. The component is discussed below:

2.4.1 Transparent Conductive Oxide (TCO)

TCO substrates must be highly transparent (transparency > 80%) to allow the maximum passage of sunlight to the active area [39] .The FTO is a type of a transparent conductive film (TCO). TCOs are optical transparent and able to transfer electric current. When the light hits the device, it is crucial that most of the rays go through the film. A metal oxide is often used for this purpose. The oxide is coated on a glass plate and used both as a substrate on the anode side and the cathode side of the DSSC. Two commonly used TCOs is ITO (indium tin oxide glass, In_2O_3/SnO_2 and the before mentioned FTO (Fluorine doped tin oxide glass, SnO_2/F. ITO has the advantage of having twice the carrier concentration of FTO.
The transmittance of ITO films are over 80% in the visible region, with a sheet resistance of approximately 18 Ω/cm^2, whereas FTO films exhibit a transmittance of approximately 75% with a sheet resistance of 8.5 Ω/cm^2 [39]. The drawback of ITO is its decrease in conductivity when exposed to high temperatures [40]. Sima et al. conducted a study based on FTO and ITO glass substrates sintered at 450 ºC [25]. They found that upon sintering, the sheet resistance of ITO increased from 18 Ω/cm^2 to 52 Ω/cm^2 version efficiencies (η) of DSSCs based on FTO and ITO are approximately

9.4% and 2.4%. Since TiO_2 is heated to 450 C° in the synthesizing process, FTO is strongly recommended for use in DSSC fabrication due to its conduction properties and stable sheet resistance temperature[25].

2.4.2 The Semiconductor (photoanode)

It is possible to divide the semiconductor into different layers, which serve different functions. These layers are referred to as a compact layer, an active layer and a scattering layer. These layers are depicted in Figure 2.6.

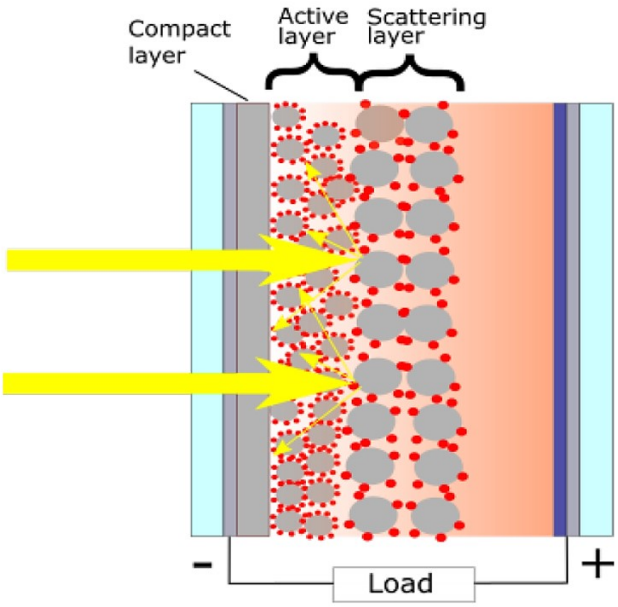

FIGURE 2.6: different layers of semiconductor (Photoanode).

2.4.2.1 Compact layer

The compact layer is placed closest to the FTO and has a thickness of around 100nm [41]. The function of this layer is to prevent and reduce the recombination route where the electrolyte come into contact with the FTO, as equation 2.7 showed. This layer is often referred to in literature is the blocking layer. Due to the higher density of the compact layer, there are also additional pathways for the electrons to diffuse into the FTO [42]. The compact layer could be coated on the FTO by a range of methods, where each method provide different advantages. To produce a TiO_2 compact layer a relatively cheap and widely used method is $TiCl_4^-$, where the FTO is immersed in a solution consisting of distilled water and TiCl4. Research by Choi et al. found that this procedure would increase the efficiency of the cell with 24% from 4.15% to 5.16% [43].

2.4.2.2 Active layer

The active layer has a thickness of around $10\mu m$ with a particle size of around 20nm [44]. This is the main layer of the semiconductor. It is in a mesoporous form, meaning that it consist of pores between 2 and 50nm. The small size of the particles and the mesoporous form ensures a high surface area, which in turn increases the amount of dye that can be adsorbed on to the surface. This behaviour is a key factor for the efficiency of the cell. A small surface area will decrease the amount of adsorbed dye, which would lead to less excited electrons and less current. The semiconductor which is most widely used in DSSC is TiO_2, which can occur in three natural forms; rutile, anatase and brookite. In a DSSC, anatase form is the desired one, due to a higher bandgap of 3.2 eV, compared to that of 3.0 eV for rutile. In addition, anatase has a higher conduction band energy, which leads to a higher Fermi level and Voc [44].

2.4.2.3 Scattering layer

Because of the small size of the particles in the active layer, the particles exhibit a poor scattering effect. As larger particles are able to scatter a greater number of the incoming photons, some DSSCs have a scattering layer coated on top of the active layer [45]. This is due to how particles with higher scattering ability lead to more light being absorbed by the dye. The scattering layer is around $3\mu m$ and contains particle with a size of 400 nm. The scattering layer does not directly contribute to the dye adsorption, but instead scatters the incoming light. Such a layer can increase the current density up to 80% [46].

2.4.3 Dye (Sensitizer)

To have a functional and efficient cell, the dye needs to possess some inherent properties. Some of these properties are as follows [47]:

- As the dye is responsible for the excitation of electrons it should be able to absorb photons from the visible region and the near infrared region (NIR). This would allow it to absorb as much of the suns energy as possible.
- For the dye to work it is dependent on a good adsorption to the surface layer of the semiconductor. The dye therefore needs to contain anchoring groups, which would make it stick to the semiconductor.
- The excited state of dye should be long enough for the electron to be injected into the conduction band of the semiconductor. If this is not the case, the electron would go back to ground state, before it is injected to the conduction band.

- The energy level of the excited state should be higher than the conduction band of the semiconductor. The electron is looking for a lower energy band, so this will make the transfer more efficient.
- To regenerate an oxidized dye, the energy level of the oxidation state should be lower than the redox potential of the electrolyte.
- To be able to repeat the process numerous times, the dye should be stable. Both electrochemically, photo-chemically as well as thermally. It should be able to stand 20 years of operation, which corresponds to about 108 turnovers [39].

Three dyes which has shown good stability and efficiency of around 11% is the ruthenium based N3, N719 and black dye 2.7 [48]. These has been widely studied and used in DSSC. A downside with these dyes is that they are relatively costly, which is why the use of cheaper natural dyes has been studied extensively [49]. At this point, they are not able to compete with the efficiency of ruthenium based dye.

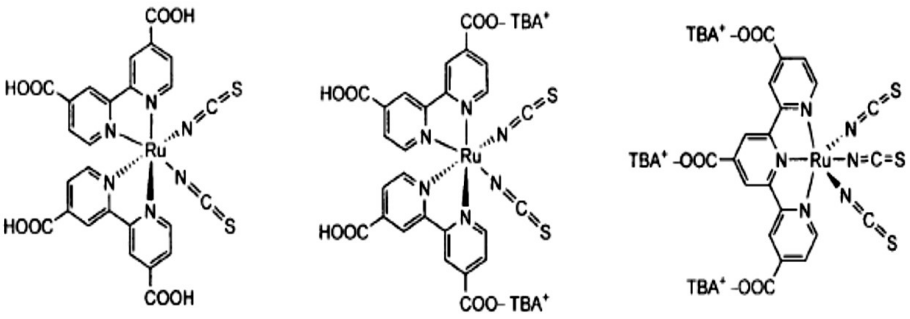

FIGURE 2.7: Chemical structure of dye materials: N3, N719 and Black dye.

2.4.4 Electrolyte

Electrolytes are used to regenerate the dye after electron injection into the conduction band of the semiconductor and also act as a charge transport medium for the transfer of positive charge toward the counter electrodes [50]. The liquid electrolyte is based on an organic solvent with a high ionic conductivity and distinctive interfacial contact properties; nevertheless, the leakage and volatility of the solvent affect the long-term performance of DSSCs [45]. Therefore, the electrolyte must have the following characteristics [49]-[51]:

1. High electrical conductivity and low viscosity for faster electron diffusion.
2. Good interfacial contact with the nanocrystalline semiconductor and counter electrode.
3. No tendency to induce the desorption of the dye from the oxidized surface or the degradation of the dye.
4. No absorption of light in the visible region.

A commonly used electrolyte is an organic solvent containing an iodide/triiodide couple. The iodide ions (I^-) reduces the dye, and turn it into triiodide (I_3^-). Other redox couples used include (Br^-/Br_2), (SCN_2/SCN^-), ($SeCN_2/SeCN^-$) [52][53] and bipyridyl cobalt (III/II) complexes [54], which have also been investigated for use in DSSCs. There are two types of solid-state DSSCs: one using a hole transport material (HTM) as a medium and one using a solid-state electrolyte containing an I^-/I_3- redox couple as the medium.
A solid-state device has recently been described in which the liquid electrolyte based on a porous nanocrystalline oxide film is replaced by a wide-band gap p-type semiconductor acting as a medium for hole transport [55] The solid-state device containing a p-type semiconductor has advantages over all solid-state cells due to its easy preparation and higher stability, whereas solar cells occupied with polymer electrolytes exhibit a higher efficiency and have additional future practical applications with proper encapsulation [55]. Organic and inorganic electron HTMs cannot be used as a transport material in DSSCs for practical applications due to their low power conversion efficiencies [56].

2.4.5 Counter Electrode

The purpose of the cathode is to transfer the electrons from the outer circuit to the liquid electrolyte. A DSSC with only FTO as the cathode will function poorly, as it has a high charge transfer resistance in a standard iodide/triiodide electrolyte. The charge transfer resistance can be as high as $10^6 cm^2$, compared to the achieved $1\Omega cm^2$ with a platinum layer coated on top. Platinum is often the material used for this purpose, and is also used in the laboratory work in this thesis. Some other alternatives are carbon materials, conducting polymers and cobalt sulfides [44].

2.5 Equivalent Circuit of DSSC

The equivalent circuit of DSSCs as shown in Figure 2.8 can thus be proposed, which is similar to that of a conventional solar cell. This suggests an abundance of experience

obtained through the development of high efficiency conventional solar cells [57] can be applied to DSSCs which consists of the current source, diode, capacitances, and the resistances.

The current source generates the (I_{PH} - photoelectric current) in proportion to the irradiation of sunlight and the (C_{Pt}) and (R_{Pt}) are the impedance through carrier transport on the surface of the counter electrode. The (C_{ELEC}) and (R_{ELEC}) are the impedance with regard to carrier transport through the ions in the electrolyte, and those are worked as the diode with regard to electron transfer of (TiO_2/dye/electrolyte) facing surface. (R_{TCO}) is the resistance through the surface resistance. (R_{SH} nored because the values of the capacitances are fairly large. That is why the circuit will be simplified such as current source, diode, one of parallel resistance, and three of series resistances [58].

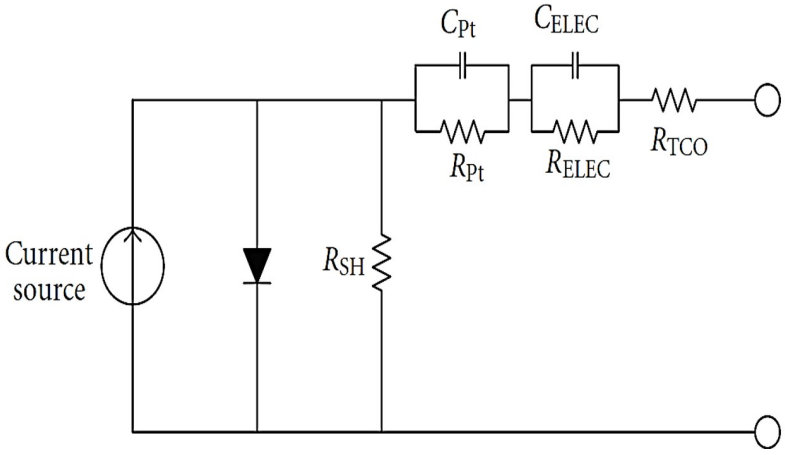

FIGURE 2.8: An equivalent circuit of a DSSC.

The Equation (2.14) represents the I_D which is the current flowing through a diode:

$$I_D = I_0 \left[exp\left(q\frac{V + IR_s}{nKT} \right) - 1 \right] \tag{2.14}$$

Equation (2.15) represents the I_{SH} which is current flowing through R_{SH}. The R_{TCO}, R_{ELEC}, and R_{Pt} are incorporated as R_S:

$$I_{SH} = \frac{V + IR_s}{R_{SH}} \tag{2.15}$$

The output current I_0 can be explained in equation number (2.16). The output current is same as all current excluding I_D and I_{SH} : $I_0 = I_{PH} - I_D - I_{SH}$

$$I_0 = I_{PH} - I_0 \left[exp\left(q\frac{V + IR_s}{nKT} \right) - 1 \right] - \frac{V + IR_S}{R_{SH}} \tag{2.16}$$

2.5.1 I.V Characteristics of DSSC

The capability of the photovoltaic cell to generate voltages over a load when illuminated can be simply explain in a current-voltage (I-V) curve. Figure 2.9 shows a typical shape of the current-voltage curve of a photovoltaic cell showing the open circuit voltage V_{oc}, short circuit current I_{sc}, and the maximum power point MPP, and the current and voltage at the MPP is given to be I_{mpp} . V_{mpp} [59]. When the cell is short-circuited under illumination by the maximum current, otherwise called the short circuit current (I_{sc}), is generated, while under open circuit conditions, that is, no current can flow and the voltage is at its maximum, called the open circuit (V_{oc}).

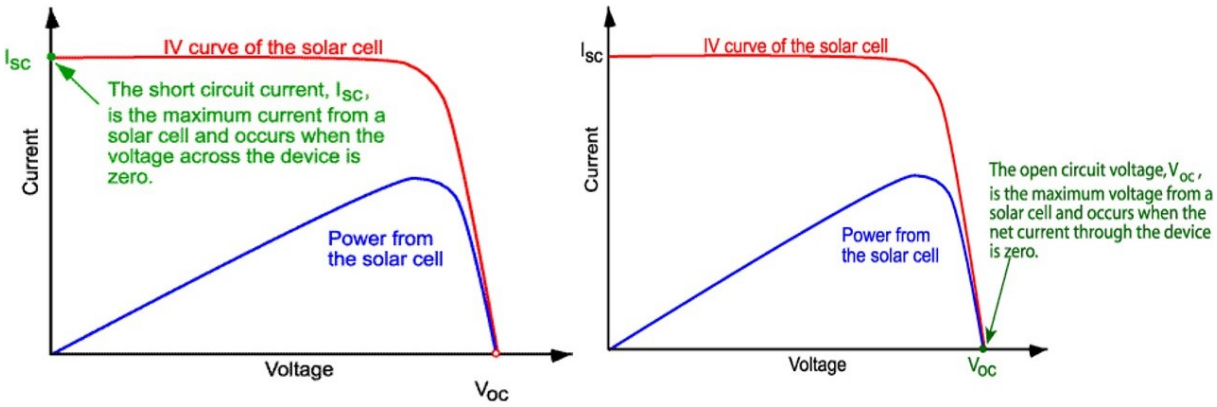

FIGURE 2.9: The photo-current-photo-voltage curve of the cell.

In Figure 2.9 The point in the I.V. curve yielding maximum product of current and voltage, i.e. power, is called the maximum power point (MPP). Another Characteristic of the solar cell performance is the fill factor (FF) which is the measure of the efficiency of solar cells.

$$P_{max} = V_{max} \times I_{max} \tag{2.17}$$

$$FF = \frac{V_{max} \times I_{max}}{V_{oc} \times I_{sc}} \tag{2.18}$$

The efficiency η of a solar cell is defined as

$$\eta = \frac{P_{max}}{P_{light}} \tag{2.19}$$

Where, (P_{light}) is illuminated power generated or some time called energy of incident photon.

2.6 Improvements in DSSCs

There are several parameters influencing the efficiency of the DSSC such as,

a Working function and resistivity of indium tin oxide electrode (ITO or FTO).

b Morphology and carrier transport properties of semiconductor (oxide materials).

c Absorption wavelength and interface alignment of dye molecule and semiconductor material.

d Electron transfer from redox electrolyte to excited dye molecule.

e Catalytic reaction of platinum counter electrode with the iodide electrolyte.

2.6.1 Improvement in dyes

A massive attempts have been achieved for developing different dyes and sensitizers in dssc that can be widely classified into the following six types: (see .Figure 2.10)

1. Ru-complex dyes.
2. metal-free organic dyes.
3. QD sensitizer.
4. perovskite-based sensitizer.
5. mordant dyes.
6. Natural dyes.

Tables 2.1 and 2.2 illustrate the status and advances of the different types of sensitizers used in DSSC [60], including Ru-complex dyes, metal-free organic dyes, QD sensitizer, perovskite-based sensitizer, mordant dyes, and natural dyes. Ru complexes have shown the good photovoltaic properties such as broad absorption spectrum, suitable excited and ground state energy levels, relatively long excited-state lifetime, and good stability. It is clear that research into the sensitizers for DSSC is progressing, and are considered as best for the production of efficient DSSC having efficiency of 10–11%.
Various metal complex dyes have been tested as sensitizers for DSSCs. On the negative side, the disadvantages of these dyes are their low conversion efficiencies. As a next step, natural dyes extracted from different easily available flower and fruits are the suitable alternative for possible application as sensitizers in DSSC. Even though natural dye-based solar cells have lower light to electricity conversion efficiency when

TABLE 2.1: Type of photoelectrode used, precursors used for the synthesis of sensitizers and the type of electrolyte used in fabrication of DSSC

DSSC type	Author	Photoelectrode	Sensitizer	Precursors used	Electrolyte	Efficiency
	Nazeeruddin et al.	TiO2 prepared by doctor blade method	cis-X2Bis(2,2′-bipyridyl-4,4′-dicarboxylate) ruthenium(II) complexes	RuL2C12.2H2O, DMF, aq. NaOH, sodium	Lithium iodide/triiodide	**10%**
DSSC with Ru-complex dyes	O'Regan et al.	TiO2 prepared by doctor blade method	Ru 2,2′ bipyridine-4,4′ dicarboxylic acid (μ-(CN) Ru (CN) 2,2′	-	Lithium iodide/triiodide	**7.1%**
	Nazeeruddin et al.	TiO2 prepared by doctor blade method	Di-tetrabutyl ammonium cis-bis (isothiocyanato) bis (2,2′-bipyridyl-4,4′-	-	Lithium iodide/triiodide	**11.2%**
	Sánchez Carballo et al.	TiO2 prepared by screen	Dichloro(p-cymene)-ruthenium(II) dimer	2-Thiophenethiol,2-	Lithium iodide/triiodide	**7.5%**
	Yella et al.	TiO2 films	YD2-o-C8	Tetrahydrofuran, TBAF, CH2Cl2,		**12.5%**
DSSC with metal-free organic dyes	Shi et al.	TiO2 prepared by screen printing method	4-(bis-(4-bromo-phenyl)-amino)-benzaldehyde	4-(diphenylamino) benzaldehyde, dichloromethane, bromine, aq.	Lithium iodide/triiodide	**5.35%**
	Zhou et al.	TiO2 prepared by electro-spray deposition	Triphenylamine moiety as the electron donor, a cyanoacrylic acid as the electron acceptor. and a	-	Lithium iodide/triiodide	**10.1%**
	Gratzel et al.	TiO2 prepared by doctor blade	Phenyl dihexyloxysubstituted	-	-	**10.3%**
	He et al.	TiO2 films	(DHO-TPA) Y123	-	Lithium iodide/triiodide	**5.1%**

TABLE 2.2: (Continued).

DSSC type	Author	Photoelectrode	Sensitizer	Precursors used	Electrolyte	Efficiency
	Lee et al	TiO2 prepared by spin coating method	Zinc porphyrin dye having an acrylic acid at	TiO2 film was dipped in Cd(NO3)2 and then into NaS	Na2S, S, and KCl	**4.22%**
	Pan et al	TiO2 films	CdSe0.45Te0.55 alloyed quantum dots	TiO2 film was dipped in Se or Te in TOP and paraffin and then	Na2S, S, and KCl	**6.36%**
DSSC with Quantum dot dyes	Santra et al.	TiO2 prepared by SILAR method	Manganese acetate mixed with cadmium nitrate/CdS/CdS	TiO2 film was dipped in cadmium nitrate in methanol- cation source	Sulfide / polysulfide	**5.42%**
	Kojima et al	TiO2 prepared by screen printing	CH3NH3)PbI3	CH3NH3I and PbI2	Lithium iodide/triiodide	**3.8%**
DSSC with perovskite-based	Im et al.	TiO2 films	(CH3NH3)PbI3	CH3NH3I and PbI2 in	Lithium iodide/triiodide	**6.54%**
	Saliba et al.	TiO2 prepared by spin	Csx(MA0.17FA 0.83)(100−x)Pb(	-	fluorene–dithiophene	**21.1 %**
	Haixia et al.	CuOx prepared by spin	CH3NH3PbI3-xClx	-	Chlorobenzol solution of	**19%**
	Alhamed et al.	TiO2 prepared by sol–gel method	Raspberries	Raspberries, methanol,	Lithium iodide/triiodide	**1.50%**
DSSC with natural dyes	Chang et al.	TiO2 nanofluid	Ipomea	Ipomea, water	Lithium iodide/triiodide	**0.28%**

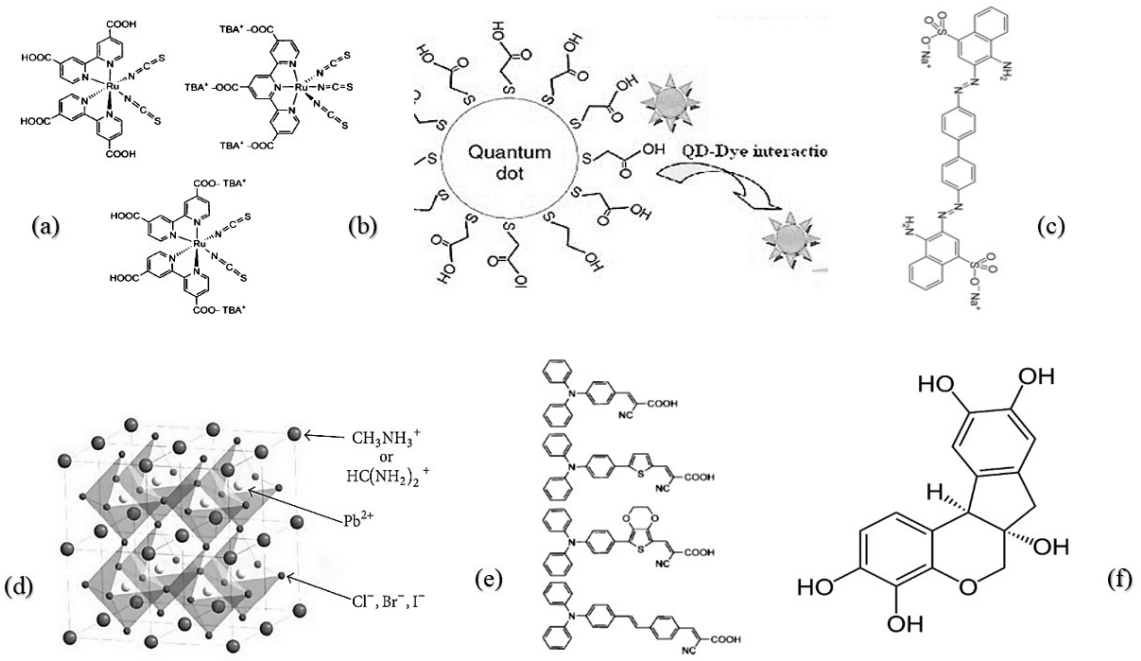

FIGURE 2.10: Chemical structure of different types of sensitizers; a) Ru-complex dyes, b) QD sensitizer, c) mordant dyes, d) perovskite-based sensitizer, e) metal-free organic dyes, f) Natural dyes.

compared with cells employing synthetic dyes, natural dyes are relatively cheaper, environmentally friendly, non-toxic, and are easily available. Thus, low conversion efficiencies of these natural sensitizers can boost research interest and provide opportunities to explore new natural dyes rendering good stability and higher efficiencies. On the other side, QD sensitizer produces an efficiency of 6.36%, and nearly 21% of efficiency is achieved using perovskite-based sensitizer[61].

2.6.2 Improvement in Electron-Charge Transporters (ETM)

The selection of the ETM is important in third-generation solar cells; the electrode materials have to satisfy a number of requirements, an extensive researches have continued to increase the power conversion efficiency of DSSC by incorporating n-type metal oxide semiconductors. We categorize ETMs into four categories: Metal oxides, carbon Nano-architecture, perovskite materials and organic compounds (see Figure 2.11) [62]. Metal oxides serving as an ETM should satisfy the following requirements. First, they should have suitable band alignment, the conduction band minimum (CBM) and valence band maximum (VBM) have to be lower than those of the dye absorber. Second, good charge mobility is necessary to transport charge carriers swiftly and suppress

charge recombination within an ETM. This section discusses several oxide-based ETMs that have been incorporated into DSSCs (Figure 2.12).

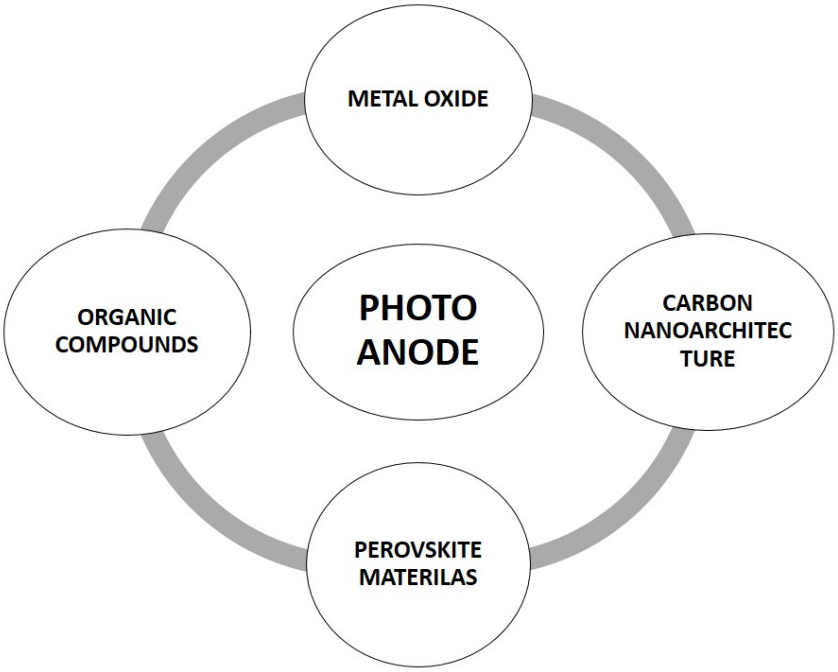

FIGURE 2.11: Schematic representation of different photo-anodes used in DSSCs.

2.6.2.1 Binary oxides materials used in DSSC

Apart from TiO_2, other metal binary oxides and composite materials such as ZnO SnO_2, Nb_2O_5, WO_3 and Fe_2O_3 have been tested for their use as photo-electrode in DSSC., Mostly binary metal oxides have been reported as a photo-anode in DSSCs. The first DSSC was fabricated by using a ZnO photo-anode, but later on TiO_2 became the most popular metal oxide for DSSCs, mainly due low cost, stability, catalytic activity and easy to prepare, TiO_2 occurs in four polymorphous. They are anatase, rutile, and brookite. Their composites as photo-electrode materials to achieve a reasonable efficiency of DSSCs of low cost, being therefore a promising alternative to conventional p-n junction solar cell.

2.6.2.2 Tin(IV) Oxide

SnO_2 is promising for electrochemical applications requiring high electrical conductivity and optical transparency [63]. Furthermore, it has better electron-hole separation ability, superior high transport properties, predominately higher electron mobility (100 $cm^2\ V^{-1}\ s^{-1}$ for nanocrystals and 200 $cm^2\ V^{-1}\ s^{-1}$ for single crystals) [64]

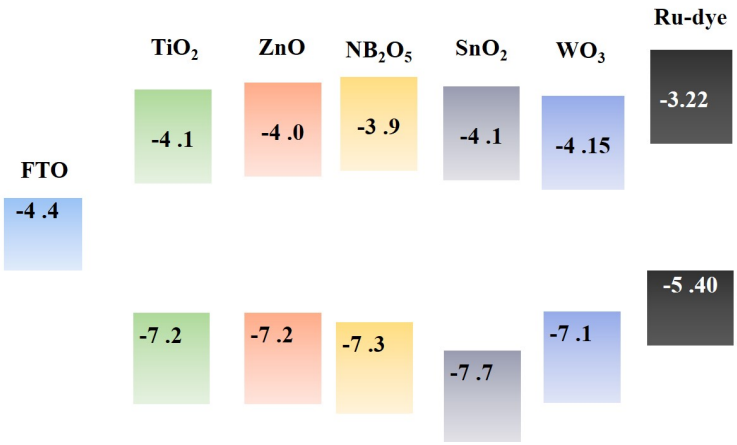

FIGURE 2.12: Energy-level diagrams of various binary metal oxides and ruthenium, used as ETM and light-harvesting material, respectively, in DSSCs.

compared with the anatase form of TiO_2 (>$1cm^2\ V^{-1}\ s^{-1}$). Moreover, SnO_2 has wider bandgap (3.6 eV) than that of anatase TiO_2 (3.2 eV), which creates fewer oxidative holes in the valence band (VB) under UV illumination, to suppress the dye degradation rate and improve the long-term stability of cells. Despite these superior properties compared with TiO_2, SnO_2 photoanode based DSSCs exhibit relatively lower efficiencies than those of TiO_2 [65]. The highest value reported for a bare SnO_2-based DSSC was 3.16% for a cell sensitized with N719 dye. To obtain a significant improvement in Voc and efficiency, numerous studies have been tested on modifying SnO_2 by:

1. Developing novel architectures
2. Covering the mesoporous SnO_2 with a thin shell of another metal oxide.
3. Doping various elements.

Among these approaches, modification of the surface with $TiCl_4$ enhanced the Voc and Fill Factor (FF), leading to nearly a twofold increase in efficiency [66].
Whereas a new record efficiency of around 7.4% was set with SnO_2 multiporous nanofiber (mpnfs) DSSCs with a thin layer of TiO_2 (T-mpnfs) by Wali et al [67]. Furthermore, Li et al. achieved a highly efficient DSSC with Zn doping into SnO_2, The overall efficiency of the optimized Zn-doped SnO_2-based DSSC reached 4.18% and increased to 7.70% after $TiCl_4$ treatment [68]. The highest efficiency in SnO_2-doped DSSC was achieved with quintuple shelled SnO_2 hollow microspheres [69]. In that study reported by Dong et al., DSSCs were constructed with SnO_2 are utilized as a scattering layer on top of P25 films photoanodes and obtained a record efficiency from 7.18% to 9.53%.

2.6.2.3 Tungsten Trioxide

Tungsten trioxide WO_3 is a transition metal oxide with a band gap of 2.6 - 3.1 eV (depending on its crystal structure) [70], it is becoming the focus of attention in research owing to its unique electronic properties, such as its high carrier mobility, which is reported to be within the range of TiO_2 [71]. Nevertheless, the problem is that the efficiency is relatively lower than that of DSSCs based on other semiconducting metal oxides such as TiO_2, SnO_2, and ZnO. One of the first studies based on WO_3 photoelectrodes was reported by Zheng et al. in 2010 [72]. They used commercial WO_3 NPs with a size of approximately 40 nm as the photoelectrode in DSSCs and obtained a PCE of 0.75% (Jsc of 4.61 mA cm2 , Voc of 0.390 V, and FF of 0.375), which was enhanced to 1.46% (Jsc of 6.67 mA cm2 , Voc of 0.490 V, and FF of 0.403) by treating the WO_3 surface with $TiCl_4$. WO_3 nanorods were applied for the first time as photo electrodes in DSSCs with or without $TiCl_4$ treatment [73]. As a result, a significant improvement in cell performance was achieved Jsc = 6.75 mA cm-2, Voc = 0.457 V, FF = 0.489, and PCE = 1.51%.This enhancement was attributed to the increase in dye loading, but also to suppression of the recombination reaction and the negative shift of the CB by TiO_2 coating.

2.6.2.4 Cerium(IV) Oxide

Nanocrystalline particles of CeO_2 with a cubic fluorite crystal structure have been synthesized via the hydrothermal method at different process times (12 and 24 h) and employed as photoelectrode materials in DSSCs [74]. The DSSCs assembled with dye-sensitized CeO_2 photoanodes showed 1.201% (Jsc =4.83 mA cm2 , Voc =0.654 V, and FF =0.380) and 0.931% (Jsc =4.01 mA cm2 , Voc =0.619 V, and FF =0.375) of PCE at 100 mW cm^2 solar illumination for Ce-12 h and Ce-24 h samples, respectively. Some approaches have been developed to improve the photocatalytic performance of CeO_2, Yu et al. in 2012 reported a type of bilayered photoanode with cubic CeO_2 NPs (with an average particle size of 400 nm) as mirror-like scattering thin layers was introduced as a submicrometer-sized CeO_2 thin layer (1.5 mm) on the top of a dense TiO_2 layer via a screen-printing technique, this approach resulted in a noticeable enhancement of PCE = 8.6% [75].

2.6.2.5 Iron (III) Oxide

Iron (III) oxide ($\alpha - Fe_2O_3$), commonly known as hematite, is an n-type s/c.Compared with ($\beta - Fe_2O_3$) and ($\gamma - Fe_2O_3$), a-phase is the most stable and frequently occurring polymorph with a rhombohedral-hexagonal structure and poor charge carrier mobility ($0.2\ cm^2\ V^{-1}\ s^{-1}$). Although ($\alpha - Fe_2O_3$) is mainly preferred as a CE in DSSCs [76], it

can also be used as an ETL owing to its relatively low bandgap energy of about 2.2 eV for sunlight harvesting.
A study based on the synthesis of ($\alpha - Fe_2O_3$) NPs and their use in DSSCs as a photoelectrode material was reported by Cavas et al. in 2013 [77]. The synthesized ($\alpha - Fe_2O_3$) films with a 2.21-eV bandgap were used to fabricate Ru-sensitized solar cells. It was observed that the efficiency of the cells increased with an increase in the light intensity. For instance, the efficiency of 0.005%, 0.011%, and 0.014% was determined for the light intensity of 50, 100, and 150 mW cm^2 , respectively. In 2014, Ocakoglu et al immobilized TiO_2 and ($\alpha - Fe_2O_3$) NPs with a multilayer structure operated at the highest quantum efficiency and generated the largest Voc. The ($\alpha - Fe_2O_3$)/PSI-LHCI biophotoanode yielded the highest overall efficiency (PCE =0.17%), the highest FF of 0.56, and the largest anodic photocurrent (Jsc = 56.9 mA) [78].

2.6.2.6 Niobium Pentoxide

As a functional metal oxide, niobium pentoxide (Nb_2O_5) is an n-type transitional s/c with an oxygen stoichiometry-dependent bandgap ranging from 3.4 to 4.0 eV and a high dielectric constant (between 33 and 40). Furthermore, it has a higher CBE than TiO_2 (it lies at least 250 mV above that of TiO_2), and therefore it is possible to attain a higher Voc and efficiency [79]. One of the first studies of the application of Nb_2O_5 in DSSCs as an ETL was reported by Guo et al. in 1999 [80]. For the cell with a 4.9 cm^2 active area, the Isc, Voc, FF, and overall PCE measured under 100 W cm^-2 light irradiation were reported to be 1.09 mA cm^-2, 0.63 V, 0.39, and 2.5%, respectively, whereas these values were Isc = 1.6 mA cm^-2, Voc = 0.57 V, FF = 0.56, and PCE =5.0% under the same light intensity for the 0.2 cm^2 device.
Another comparative study was reported by Ou et al. in 2012 [79]. For the same thicknesses of 4 mm, the DSSC based on the crisscross nanoporous Nb_2O_5 layer fabricated by electrochemical anodization showed a higher efficiency(4.1%). The highest efficiency of about 6% was reported by Zhang et al. in 2012, with 11.2-mm-thick, hydrothermally grown Nb_2O_5 nanorods with a relatively high surface area of 71 m^2 g-1, the Isc, Voc, FF, and overall PCE measured were reported to be 12.20 mA cm^-2, 0.75 V, 66, and 6.03%, respectively [81].

2.6.2.7 Zinc Oxide

As a natural n-type s/c, ZnO, which has a wide direct bandgap of about 3.3 eV, is one of the most promising metal oxides for DSSC applications, next to TiO_2. The potential use of ZnO in DSSC is gaining interest in the scientific and industrial communities, largely owing to its electronic band position (similar to TiO_2), large excitation binding

energy (60 meV at room temperature), and high electron mobility (one to two orders of magnitude greater than that of anatase TiO_2) [82]. In earlier work carried out by Rao and Dutta, ZnO-based DSSCs were fabricated using hydrothermally synthesized ZnO NPs by spray deposition [83].
The DSSC with a nanocrystalline film thickness of about 4.3 mm yielded an efficiency of approximately 2.8% for a cell area of about 3.2 cm^2, whereas the DSSC with a cell area about 1 cm^2 with a photo-electrode thickness of approximately 4.5 mm was reported to be 4.7% (an enhancement of about 60%). An unprecedented PCE of 7.5% (Voc = 640 mV, Jsc = 19.8 mA cm^-2, and FF =0.59) for ZnO ETL-based DSSCs was achieved by Memarian et al [84]. Although this value is the highest efficiency, to the best of our knowledge, this is still far from the record efficiency for TiO_2.

TABLE 2.3: Photovoltaic Performances Summary of different types Binary oxides used as an ETM in DSSC

Photo-anodes (Binary oxide)	Structure	JSC (mA/cm^2)	V_{OC} (V)	FF	$\eta(\%)$
Tin(IV) Oxide (SnO_2)	P25-5S-SnO_2-HMSs	20.1	0.75	0.63	9.53
Tungsten Trioxide (WO_3)	$WO_3/TiCl_4$ treatment	6.75	0.457	0.5	1.51
Cerium(IV) Oxide (CeO_2)	TiO_2–CeO_2	19.3	0.69	65	8.6
Iron(III) Oxide (Fe_2O_3)	Fe_2O_3/PSI-LHCI	56.9	0.321	0.56	0.17
Niobium Pentoxide (Nb_2O_5)	Nb_2O_5 nanorods	12.2	0.75	66	6.03
Zinc Oxide (ZnO)	ZnO comp/ZnO	19.8	0.64	0.59	7.5
Titanium dioxide (TiO_2)	TiO_2	1.7	0.87	0.77	12.5

2.6.3 Ternary oxides materials used in DSSC

Besides the non-TiO_2 single oxides. Ternary metal oxides such as $CaTiO_3$ [85], $BaTiO_3$ [86], $SrTiO_3$ [87][88], $BaSnO_3$ [89][90] Zn2SnO_4 and Zn2TiO_4 have been applied for the DSC semiconductor electrodes, and they are mainly studied as a photoanode materials for DSSC (Figure 2.13). Ternary metal oxides or also known perovskite oxides which has the general stoichiometry (ABX_3), where "A" and "B" are cations and "X" is an anion where can have a variety of charges [91]. Calcium titanium oxide ($CaTiO_3$) was the first perovskite discovered in the Ural Mountains of Russia by Gustav Rose in 1839, and perovskite was named after Russian mineralogist Lev Perovski (1792–1856), which have the same perovskite structure as the hybrid perovskite absorber in PSCs [111].
These perovskite-types double oxides, are more attractive than simple oxides due to their high durability, good chemical affinity, proper band alignment and high electron mobility, as their electrical properties and band structure can be easily modified by alternating the composition.

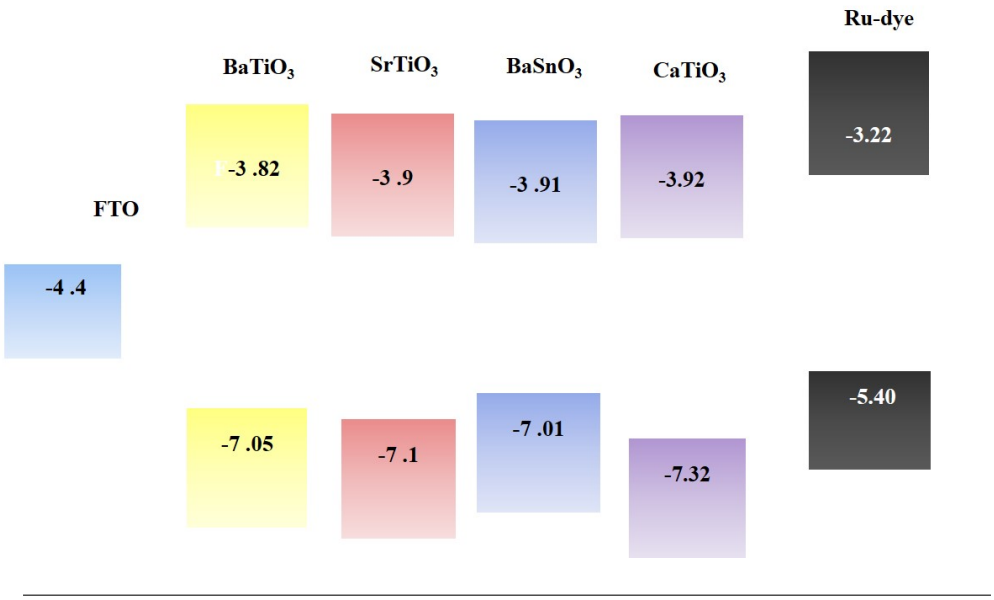

FIGURE 2.13: Energy-level diagrams of various binary metal oxides and ruthenium, used as ETM and light-harvesting material, respectively, in DSSCs.

2.6.3.1 Calcium titanate $CaTiO_3$

Fabrication of dye sensitized solar cell based on $CaTiO_3$ modified TiO_2 electrode has been investigated by Shuming Yang et all [85]. The photocurrent-photovoltage characteristics of Sandwich type solar cells based on N3 sensitized TiO_2 and $TiO_2/CaTiO_3$ electrodes increasing with increasing the deposition time of $CaTiO_3$ layer, the dye amount on electrode surface would decrease when $CaTiO_3$ layer is thin, resulting in decreased photocurrent or efficiency. As a result, the photo-electrochemical properties of the modified electrodes is crucial to proper thickness of $CaTiO_3$ layer. The highest conversion efficiency is 9.23% under irradiation of 100 mW $/cm^{-2}$ white light, obtained with an open-circuit voltage (Voc) of 0.654V and a short-circuit current density (Jsc) of 22.67 (mA/cm^2) in $TiO_2/CaTiO_3$ (45 min) electrode.

2.6.3.2 Barium titanate ($BaTiO_3$)

$BaTiO_3$ is an n-type semiconductor, shows band gap energy closer to that of TiO_2 (Eg=3.2 eV). Hierarchical barium titanate ($BaTiO_3$) micro flowers have been successfully grown on the conducting glass substrates, which has demonstrated recently as an useful functional material in the construction of dye sensitized solar cell (DSSC) photoanodes and showed an open-circuit voltage (Voc), short-circuit current density (Jsc) and maximum power conversion efficiency (PCE) of 0.7 (V), 12.34 (mA/cm^2) and 5.13%

respectively , measured under one sun illumination conditions. Besides, incident photon to current conversion efficiency (IPCE) and UV-visible absorption analyses have confirmed that the superior light harvesting capability of $BaTiO_3$ micro flowers over TiO_2 nanoparticles is observed in DSSC due to their favourable morphological features and increased visible light absorption properties along with the superior charge transport characteristics of nanorods [86].

2.6.3.3 Strontium titanate ($SrTiO_3$)

The nanostructured $SrTiO_3$ electrode was sensitized with dye N3 and its photovoltage-photocurrent curves were measured in three electrolytes composition PN, PN/Acac, and Acac [87]. The N3- sensitized $SrTiO_3$ showed the highest open-circuit voltage (Voc) of 0.6 (V) and short-circuit current density (Jsc) of 0.41 (mA.cm^{-2}). In good agreement with the electrochemical measurements that the nanostructured $SrTiO_3$ electrode has the flat band edge well matching with the excited state of N3. Shelly Burnside et all, have utilized $SrTiO_3$ as a working photoelectron-chemical solar cells. At (AM 1.5), Photocurrents measured in the $SrTiO_3$ cells were 3(mA/cm2), roughly 1/3 those measured with TiO2 (anatase)-based cells. Measured open circuit voltages were roughly 0.789 V, which is 100 mV higher than in solar cells produced using nanocrystalline titanium dioxide (anatase), with an efficiency of 1.8 % [88].

2.6.3.4 Barium stannate ($BaSnO_3$)

Highly crystalline $BaSnO_3$ nanoparticles have been achieved as the photoanode for a DSSC solar cell with an overall energy conversion efficiency of 5.2% which is higher than the efficiency of the TiO_2 cell (4.5 %), the overall energy conversion efficiencies for DSSCs using $BaSnO_3$ nanoparticles increased as the film thickness increased and became saturated for thicknesses greater than approximately 40 mm. The high photovoltaic performance that was obtained from the DSSC based on the 43 mm-thick of $BaSnO_3$ film.The photoelectrode was also fabricated without any additional functional layers or treatments to enable the accurate examination of the photovoltaic properties of the $BaSnO_3$ film itself. A porous nanoparticle film of $BaSnO_3$ was immersed into a solution of N719 dye, film were shown to have a larger amount of adsorbed dye than the TiO_2 film, which led to a higher open-circuit voltage (Voc) of 0.60 (V) and short-circuit current density (Jsc) of 13.1 (mA.cm^{-2}) [89].
Seong Sik Shin et all, reported report a new highly efficient DSSC using perovskite $BaSnO_3$ (BSO) nanoparticles treated by $TiCl_4$ Material, which found that $TiCl_4$ formed an ultrathin TiO_2 layer on the BSO, The formation of the TiO_2 shell layer improved the charge-collection efficiency by enhancing the charge transport and suppressing the

charge recombination, leading to the highest conversion efficiency of 5.5% after a $TiCl_4$ treatment. The conversion efficiency increased further to 6.2% by increasing the thickness of the BSO film, which is one of the highest efficiencies from non-TiO_2-based DSSCs [90].

2.6.3.5 Zinc orthotitanate (Zn_2TiO_4)

Zn_2TiO_4 films have been synthesized for applications in DSSCs and are shown to offer a reasonable functioning as an electron acceptor with the best preliminary performance reported so far. The increase in the short-circuit current density and open-circuit voltage with increasing film thickness of the active layer is clearly visible from the J–V curves, the increase in the fill factor is really minor. The photovoltaic properties of (Jsc = 4.6 mA.cm^{-2}, Voc = 720 mV, FF=0.436 and power conversion efficiency of 1.5%) are very promising as a preliminary result and is the best announced so far with Zn_2TiO_4 films synthesized via sol–gel technique. However, Kuhu Sarkar et [91] all postulate improvement in power conversion efficiency of Zn_2TiO_4 based DSSCs in near future with more optimized device fabrication procedure. Hence, the development of Zn_2TiO_4 as a new functional material parallel to conventional inorganic metal oxides in large-scale electro optical applications is foreseen.

2.6.3.6 Zinc titanate ($ZnTiO_3$)

For the first time, $ZnTiO_3$ applied as an innovative photoanode material in quantum-dot-sensitized solar cells (QDSSCs) has been systematically researched both theoretically and experimentally by Jing Yu et all[92]. The electron mobility (150-400 cm^2/vs) of this material, achieved via the deformation potential theory, is much higher than that of most known photoanodes, including TiO_2 and ZnO which have been heavily researched. The preparation of QDSSCs with the structure of $ZnTiO_3$/CdS/CdSe yielded a high energy conversion efficiency of 1.95% and a large short-circuit current density of 5.96 mA/cm^2, which are also superior to the characteristics of other emerging photoanode materials, such as SnO_2, Zn_2SnO_4, $BaTiO_3$, and so on, indicating the good potential of this material for using in QDSSCs.

Figure 2.14, shows a strategy for efficiently finding new metal oxides to be used as ETMs in DSSCs [93]. First of all, metal oxide candidates having appropriate electronic properties are searched via a computational method based on density functional theory (DFT). As mentioned above, metal-oxide candidates for ETMs should possess favourable conduction band and valence band positions, superior electron or hole mobility, and conductivity. From the DFT calculations, we can obtain information about

TABLE 2.4: Photovoltaic Performances Summary of different types Ternary oxides used as an ETM in DSSC

Photo-anodes (Binary oxide)	Structure	JSC(mA/cm^2)	V_{OC} (V)	FF	$\eta(\%)$
Calcium titanate ($CaTiO_3$)	$TiO_2/CaTiO_3$/N3	22.67	0.654	0.62	9.23
Barium titanate ($BaTiO_3$)	$BaTiO_3$/N719	12.34	0.77	0.54	5.13
Strontium titanate ($SrTiO_3$)	$SrTiO_3$/N3	3	0.789	0.70	1.8
Barium stannate ($BaSnO_3$)	$BaSnO_3$/N719	15.5	0.62	0.63	6.2
Zinc orthotitanate (Zn_2TiO_4)	Zn_2TiO_4/-	4.6	0.724	0.436	1.5
Zinc titanate ($ZnTiO_3$)	$ZnTiO_3$/CdS/CdSe	5.96	0.59	0.56	1.59

the electronic structure as well as the intrinsic properties of various metal oxides such as bandgap, band structure, Fermi energy, density of states, effective mass of electron and hole, and carrier density [94]. Because DFT is based on the chemical compositions and structures of materials without the use of intervening models, it is possible to predict the electronic properties of possible combinations of binary and ternary metal oxides from the periodic table using DFT [95].Oxide ETMs can perform better if they are properly doped or coated in their surfaces, because the interface between the ETM and the absorber layer is a crucial factor in determining crystal growth and charge transport behaviour[96].

2.6.4 Developments in electrolytes

2.6.4.1 Liquid electrolyte

As demonstrated over the past several years, the iodide–triiodide (I_3^-/I^-) electrolyte has been recognized as the most universal redox shuttle because of its satisfactory kinetic properties, such as fast oxidation of (I^-) at the photoanode/electrolyte interface for efficient dye regeneration and slow reduction of (I_3^-) at the electrolyte/counter electrode interface for high carrier collection, excellent infiltration, relative high stability, low cost and easy preparation. To date, the PCE of (I_3^-/I^-) electrolyte-based DSSCs has been roughly 11% [97]. Despite this, several shortcomings exist for the (I_3^-/I^-) electrolyte. Disadvantages such as the absorption of visible light at 430 nm, corrosion of the noble metal counter electrode (e.g. Pt, Au), and an upper limit on VOC of 0.9 V, significantly restrict further development of DSSCs using this electrolyte system [98]. As a result, several alternative electrolytes have been investigated, including Co(II/III) polypyridyl complex, ferrocenium/ferrocene (Fc/Fc^+) couple, Cu(I/II) complex, and thiolate/disulfide mediator [99]. However, liquid electrolytes still show

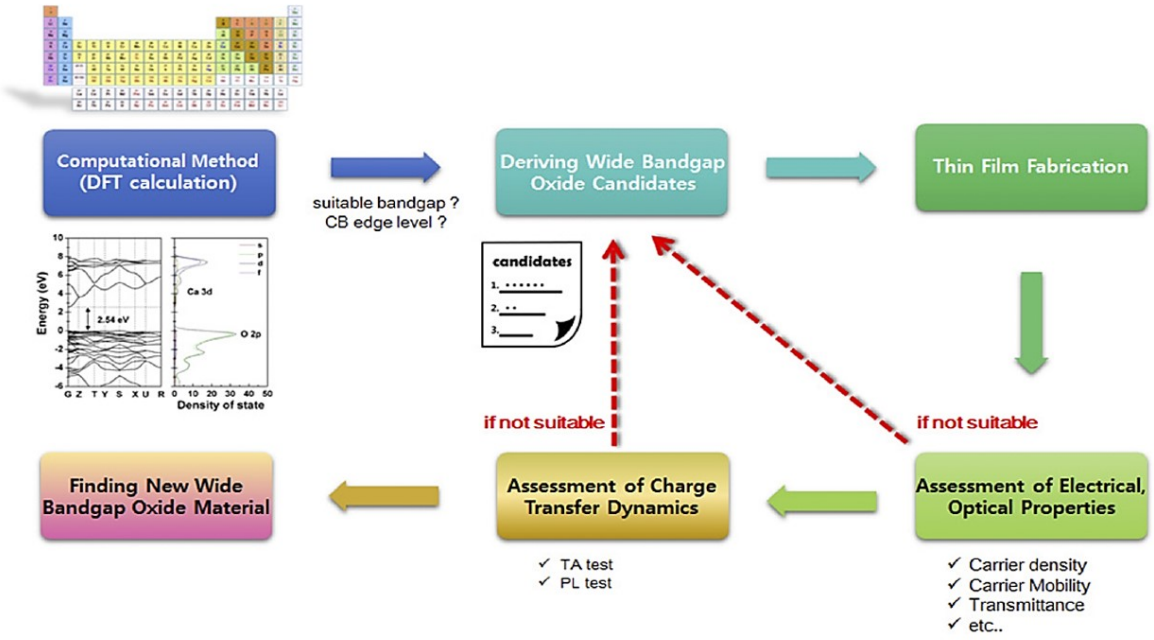

FIGURE 2.14: Flowchart for finding a new wide bandgap metal oxide for using as an ETM in DSSCs.

a massive problem in stability and durability, which can easily evaporate under the sunlight and leads to small DSSC lifetime.

2.6.4.2 Quasi-solid electrolyte

In the case of liquid electrolytes, sealing problems and long-term durability substantially hinder the practical application of DSSCs. Therefore, efforts have been directed toward alternatives to liquid electrolytes, that is, quasi-solid-state electrolytes and solid-state electrolytes [100]. Ionic liquids (e.g. 1-propargyl-3- methylimidazolium iodide, bis(imidazolium) iodides and 1-ethyl-1-methylpyrrolidinium) and polymer gel (e.g. poly(ethylene oxide), poly(vinylidinefluoride) and polyvinyl acetate) containing redox couples are commonly used as quasi-solid-state electrolytes to overcome the volatilization and leakage problems of liquid electrolytes [101]. To date, the corresponding PCEs or DSSCs based on quasi-solid-state electrolytes have reached 8–9% [102] [103]. However, because of their thermodynamic instability under high temperature, quasi-solid-state electrolytes still suffer from solvent leakage, and thus also require careful sealing treatment when used in high temperature environments [104].

2.6.4.3 Solid-state hole transport conductor

Solid-state electrolytes, including various hole transporting materials (HTMs) have been extensively investigated as hole acceptors to replace liquid electrolytes [104]. Several inorganic p-type materials (e.g. CuI/CuSCN and $CsSnI_3$) and organic polymers (e.g. poly (3,4-ethylenedioxythiophene) (PEDOT), 2,20,7,70-tetrakis (N,N-di- 4-methoxy- phenylamino)-9,90-spirobifluorene (spiro-MeOTAD), poly (3-hexylthiophene) (P3HT)) have been successfully used in solid-state DSSCs (SS-DSSCs) [104][105][106]. CuI/CuSCN HTMs possess high hole mobility. However, fast crystallization rates result in poor filling into photoanode films, and thus SS-DSSCs show relatively low PCE of 3.8% [105]. $CsSnI_3$, possessing high hole mobility, low cost, abundant raw materials, and low-cost processing, is another promising p-type semiconductor HTM. Such electrolyte- based devices have yielded a PCE of up to 10.2% for SSDSSC in 2012 [107]. Spiro-MeOTAD is much better than other types of organic HTMs [108], and in 2013 produced a high PCE of 15% when used in perovskite-based SS-DSSCs [109].
However, low hole mobility and high manufacturing costs still inhibit the application of spiro-MeOTAD in SS-DSSCs. Good diffusion of HTMs into photoanode films and high conductivity for effective hole transfer are key issues for solid-state electrolytes in high performance SS-DSSCs.
Consequently, solid-state electrolytes will be the major focus for DSSC electrolyte research and industrialization in the future.

2.6.5 Developments in counter electrodes

The counter electrode (CE) in DSSCs has the important task of collecting electrons from the external circuit and catalysing the reduction of redox electrolyte or transporting holes in solid-state electrolyte. High conductivity for charge transport, good electrocatalytic activity for reducing the redox couple and excellent stability are the primary requirements for CE materials [98]. Noble metals, such as Pt, Au and Ag, are the most popular CE materials because of their high electrocatalytic activity (e.g. Pt) for the reduction of redox couples in liquid electrolytes or effective hole transfer in solid-state electrolytes (e.g. Au and Ag) [110]. However, noble metals are expensive and their corrosion in liquid electrolyte is a concern. Consequently, several alternatives have been extensively explored to replace noble metal CEs.

2.6.5.1 Carbon materials

Because of their low cost, good electrocatalytic activity, high electrical conductivity, high thermal stability and corrosion resistance, carbon materials (e.g. porous carbon, carbon nanotubes (CNTs) and graphene) have been intensively used as CEs and have

yielded high-performance DSSCs [111, 112, 113]. Recent studies have shown that combining two carbon materials, for example, porous carbon/carbon nanotubes [113], and carbon nanotube/graphene nano-ribbons [114], can further amplify the electrocatalytic activity of CEs. The interconnection of carbon materials and other types of CE materials is also a popular area of research.

2.6.5.2 Inorganic compounds

Sulfides (e.g. CoS_2, $CuInS_2$, Cu_2ZnSnS_4, Co_9S_8, Sb_2S_3, Cu_2S and $CoMoS_4$) [115, 116, 117, 118, 119, 120], carbides (e.g. TiC) [121], nitrides (e.g. TiN, ZrN) [122, 123], phosphides (e.g. Ni2P and Ni5P4) [124], tellurides (e.g. CoTe and $NiTe_2$) [125], and metal oxides (e.g. WO_2 and V_2O_5) [126] also been introduced as effective CE materials because of their promising application in low-cost and large-scale DSSCs. However, the performance and stability of inorganic compounds still need to be improved.

2.6.5.3 Conductive polymers

Because of their high conductivity, transparency, and stability, some conductive polymers including polyaniline (PANI), poly (3,4- ethylenedioxythiophene) (PEDOT), and polypyrrole (PPy) have been employed as CE materials for DSSCs; especially for transparent and flexible DSSCs [127, 128, 129]. Among these, PEDOT is the most commonly used CE material and doping of different components (TsO-, ClO-, poly (styrenesulfonate) (PSS) and polyoxometalate (POM)) into PEDOT is frequently employed to increase its solubility and electrical conductivity in DSSCs [130, 131]. Despite many available polymers to consider, cost and performance concerns remain. Further development of conductive polymer CE-based DSSCs is required.

2.6.5.4 Composites

Composite CEs, which are typically composed of two or more components that combine the merits of each component into one, have been widely investigated. In particular, composites of carbon [132] materials and other organic/inorganic materials such as graphene- Pt/TaON/NiS2/NiO//TiN/PPy [133, 134, 135, 136, 137, 138] and carbon nanotube-Pt/TiN/NiS/WS2/PEDOT:PSS have been studied [139, 140, 141].

2.6.6 Advantages and Disadvantages of DSSC

2.6.6.1 Advantages

In a DSSC, the semiconductor is used mainly for charge transport the photo electrons are supplied by a different natural source (dyes). DSSCs work even in a wide array

of lighting conditions. Hence they are very popular under cloudy weather conditions, where traditional cells would be a failure. The cut-off in DSSC is so low they have been suitable for indoor and outdoor usage. Dye sensitized solar cells are the third-generation solar technology and are used as rooftop solar collectors.
The efficiency production of DSSCs is around 11%, as compared to thin-film technology cells which are in between 5% and 13%. DSSCs operate at low internal temperatures as they are built up with only a thin layer of conductive plastic on the front side to allow radiation of heat much easily quickly. Also the cell's mechanical structure is in such a way that it indirectly leads to higher efficiencies in higher temperatures. DSSCs manufacturing requires a low-energy consumption, high-efficiency, roll-to-roll manufacturing technique. DSSCs use inexpensive and eco-friendly nanomaterial. Indoor modules of DSSCs are highly flexible, light weight and durable. DSSC can also be applied to metal and glass substrates as it is produced on a thin film, flexible, robust, plastic substrate.

2.6.6.2 Disadvantages

For large-scale deployments where higher-cost higher-efficiency cells are more viable, DSSCs are not considered as a best option. The sharp cut in silicon solar panels costs led other types of solar technology like Solar Thermal and Thin Film Technology taking a back seat. Dye sensitized solar cell design use the liquid electrolyte, which is not very stable at varying temperatures and freezing the electrolyte at low temperatures cut the power production and cause physical damage. When the liquid expands at higher temperatures, sealing the panels becomes a very difficult task. DSSCs electrolyte solution contains volatile organic solvents which must be carefully sealed. Research in replacing the liquid electrolyte with a solid electrolyte is ongoing. Iodide/triiodide can cause the severe corrosion to the sealing materials which limits the use of DSSCs.

TABLE 2.5: Comparison between silicon solar cell and dye-sensitized solar cell (dssc)

	Semiconductor Solar Cells	Dye-Sensitized Solar Cells
Transparancy	Opaque	Transparent
Pro-environment	Normal	Great
Power generation cost	High	Low
Power generation efficiency	High	Normal
Color	Limited	Varios

2.7 Conclusion

In summary, after a brief introduction of solar cells history and solar photovoltaic technologies we tried to focus on dye sensitizer solar cell technology, including work principle of DSSC, recent advances in the components of DSSCs. These include the photoanode, sensitizer, electrolyte, and counter electrode, and its recent improvements and developments in power conversion efficiency.

The status and advances of the different types of sensitizers used in DSSCs, including Ru-complex dyes, metal-free organic dyes, QD sensitizer and perovskite-based sensitizer have been discussed in this chapter, These sensitizers play a crucial role in the efficiency of DSSC and PSCs, which concluded that using perovskite-based sensitizer such as $MAPbI_3$ leads to achieved a high efficiency in PSCs nearly 21%. Titanium dioxide (TiO_2) nanoparticle has been dominated and became the most popular photoanode and electron transport material (ETM) for DSSCs, mainly due low cost, stability, catalytic activity and easy to prepare. However, the search for suitable binary or ternary metal oxides have together been investigated to provide a viable route toward enhancing the efficiency and stability of DSSCs and PSCs.

However, the major challenge in the fabrication and commercialization of DSSCs is the low conversion efficiency and stability of the cell. The degradation of the cell based on dye sensitization, undesirable electrolyte properties and poor contact with the electrodes are the main causes of the poor performance of DSSCs. To enhance the performance of the DSSCs, several research directions are suggested: (i) improving the dye stability by finding the optimum parameters to slow the dye degradation; (ii) improving the dye structure to absorb more light at longer wavelengths, 780-2500 nm (the near-infrared region, NIR); (ii) improving the morphology of semiconductors to attaining the best electronic conduction to reduce the dark current; (iv) using dye and electrolyte additives to enhance the cell performance; and (v) improving the mechanical contact between the two electrode. Thus, the choice of materials is very important in the fabrication and deployment of DSSCs because the conversion efficiency and stability of the DSSC do not relate to only one factor.

In next Chapter we have studied the performance of $ZnTiO_3$ perovskite material as an ETM in DSSC in term of surface area and electron mobility as well as energy band levels of the system using Material Studio software.

Chapter 3

Overview to Materials Studio Software

3.1 Materials Studio Software.

Materials Studio is a complete modelling and simulation environment designed to allow researchers in materials science and chemistry to predict and understand the relationships of a material's atomic and molecular structure with its properties and behaviour based on Density functional theory DFT. Using Materials Studio, researchers in many industries are engineering better performing materials of all types, including pharmaceuticals, catalysts, polymers and composites, metals and alloys, batteries and fuel cells, and more.
Materials Studio is the world's most advanced, yet easy to use environment for modelling and evaluating materials performance and behaviour. Using Materials Studio, materials scientists experience the following benefits:

- **Reduce Costs:** Materials Studio customers have indicated a reduction of up to 10 times in the number of experiments required to introduce a new material.
- **Improve Efficiency:** Automate repetitive or tedious modeling tasks by creating reusable modeling and simulation protocols.
- **Collaborate:** Capture and share expert knowledge and methods to make computational science more consistent across organizational and geographic boundaries.
- **Solve Your Most Difficult Problems:** BIOVIA's staff of expert scientists assures timely support and expertise to help solve even the most challenging problems in materials science.

Materials Studio provides a complete range of simulation capabilities from quantum, atomistic, mesoscale, statistical, analytical and crystallization tools. Its' broad range of solutions enable researchers to evaluate materials at various particle sizes and time scales in order to predict properties more accurately and evaluate performance in the shortest time possible. BIOVIA Materials Studio 2019 is the latest release of BIOVIA's predictive science tools for chemistry and materials science research. Materials Studio empowers researchers to understand the relationships between a material's atomic and

molecular structure and properties in order to make more informed decisions about material research and development[142].

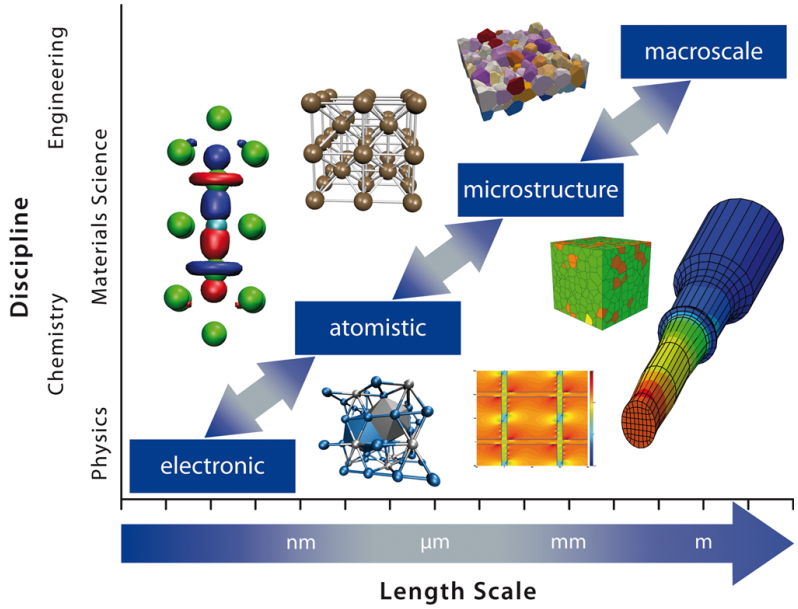

FIGURE 3.1: The different length scales.

3.1.1 Visualization and Statistics Software

Materials Studio Visualizer is complemented by a complete set of solution methods including quantum, atomistic (or "classical"), mesoscale, and statistical that enable researchers to evaluate materials at various particle sizes and time scales. It also includes tools for evaluating crystal structure and crystal growth.
Materials Studio allows you to easily build, modify, visualize and simulate a wide range of materials including:

- Polymers
- Surfactants
- Molecular/Inorganic crystals
- Corrosion inhibitors
- Zeolites

Materials Visualizer provides modeling, analysis, and visualization tools. Combined with its clear and intuitive graphical user interface, Materials Visualizer offers a high-quality environment into which you can plug any MS Modeling product.

Materials Visualizer offers a versatile and completely comprehensive modeling and visualization system. You can increase your understanding of materials and improve your communication of chemical information; visualize and model structures from chemical databases; build your own molecules and materials with fast, interactive sketching, building, and editing tools; calculate and display key structural parameters; display the results of calculations – animated dynamics trajectories, graph data, and molecular models; annotate models for pictures and diagrams and produce exceptionally high quality hard-copy output.
Materials Visualizer can run on any PC on your network, allowing scientists to use it when and where they need it. Whether used to run a range of MS Modeling modules or as a stand-alone modeling system, Materials Visualizer focuses computational and graphics power on the solution of scientific problems [143].

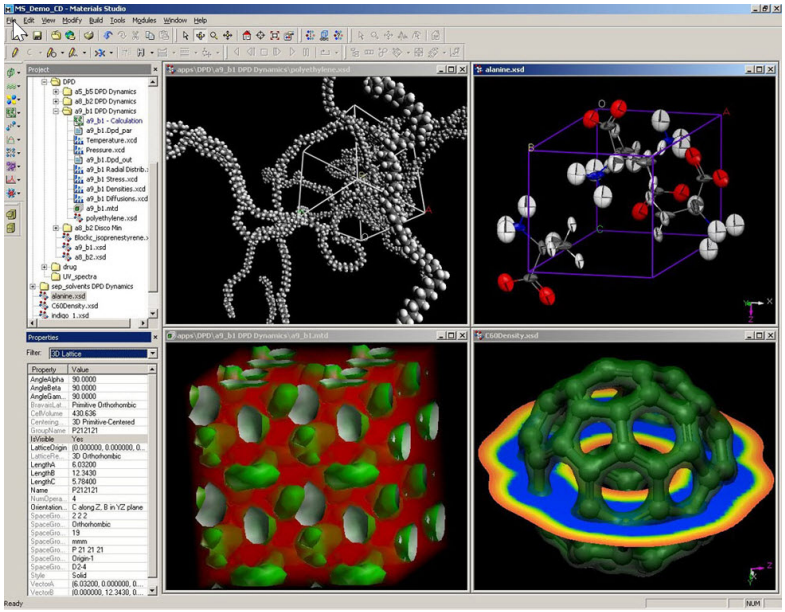

FIGURE 3.2: A screenshot of Materials Visualize.

3.1.2 Materials Studio Modules Descriptions

Materials Studio provides tools for modeling crystal structure and crystallization processes, for the study of polymer properties, catalysis, and the study of structure-activity relationships, in this section we briefly describe each Module and product in MS [142].

1. **Adsorption Locator**
   Adsorption Locator enables you to simulate a substrate loaded with an adsorbate or an adsorbate mixture of a fixed composition. Adsorption Locator is designed for the study of individual systems, allowing you to find low energy adsorption

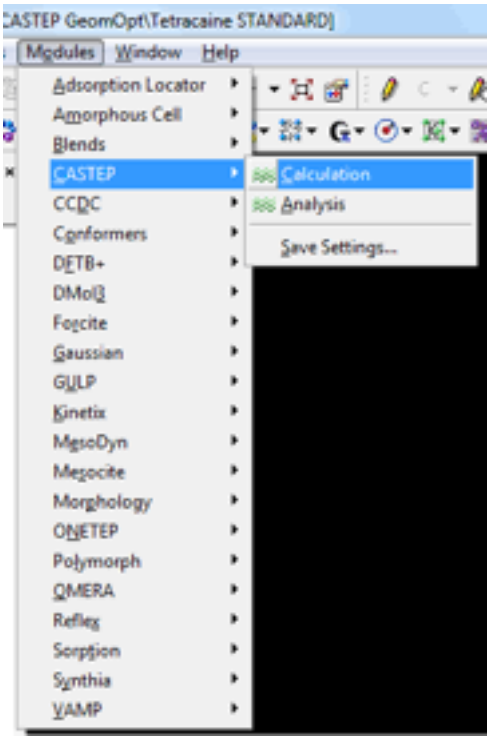

FIGURE 3.3: Materials Studio Modules

sites on both periodic and nonperiodic substrates or to investigate the preferential adsorption of mixtures of adsorbate components, for examlple. Adsorbates are typically molecular gases or liquids and substrates are usually porous crystals or surfaces, such as zeolites or carbon nanotubes, or amorphous structures, such as silica gel or activated carbon. Adsorption Locator identifies possible adsorption configurations by carrying out Monte Carlo searches of the configurational space of the substrate-adsorbate system as the temperature is slowly decreased.

2. **Amorphous Cell**
   Amorphous Cell is a suite of computational tools that allow you to construct representative models of complex amorphous systems and to predict key properties. By observing the relation between system structure and properties, you can obtain a more thorough understanding of the important molecular features, allowing you to better design new compounds or new formulations. Among the properties that you can predict and investigate are cohesive energy density, equation-of-state behavior, chain packing, and localized chain motions

3. **Blends**
   The product formulations that are most successful today tend to be complex mixtures. As a result, the properties affecting miscibility, mixing, compatibility, and adhesion play a critical role in the development of new products. Unfortunately,

the time required to develop new formulations in the laboratory can be significant. It is estimated that the average time required to fully test a new binary polymer mixture, for example, is three weeks. A direct method for estimating the free energy of mixing between formulation components could speed up this process considerably. Blends provides a way to shorten the discovery process by estimating the miscibility behavior of binary mixtures. These include solvent-solvent, polymer-solvent, and polymer-polymer mixtures. Blends predicts the thermodynamics of mixing directly from the chemical structures of the two components and, therefore, requires only their molecular structures and a forcefield as input.

4. **CASTEP**
   CASTEP is a state-of-the-art quantum mechanics-based program designed specifically for solid-state materials science. CASTEP employs the density functional theory plane-wave pseudopotential method, which allows you to perform first-principles quantum mechanics calculations that explore the properties of crystals and surfaces in materials such as semiconductors, ceramics, metals, minerals, and zeolites. Typical applications involve studies of surface chemistry, structural properties, band structure, density of states, and optical properties. CASTEP can also be used to study the spatial distribution of the charge density and wavefunctions of a system. In addition, you can use CASTEP to calculate the full tensor of second-order elastic constants and related mechanical properties of a crystal (Poisson coefficient, Lame constants, bulk modulus). The transition-state searching tools in CASTEP enable you to study chemical reactions in either the gas phase or on the surface of a material using linear synchronous transit/quadratic synchronous transit technology. These tools can also be used to investigate bulk and surface diffusion processes.
   CASTEP can be used effectively to study properties of both point defects (vacancies, interstitials, and substitutional impurities) and extended defects (for example grain boundaries and dislocations) in semiconductors and other materials.
   Furthermore, the vibrational properties of solids (phonon dispersion, total and projected density of phonon states, thermodynamic properties) can be calculated with CASTEP using either the linear response methodology or the finite displacements technique. The results can be used in various ways, for instance, to investigate the vibrational properties of adsorbates on surfaces, to interpret experimental neutron spectroscopy data or vibrational spectra, to study phase stability at high temperatures and pressures, and so on.

The linear response method can also be used to calculate the response of a material to an applied electric field - polarizability for molecules and dielectric permittivity in solids - and to predict IR spectra. CASTEP can be used to calculate the properties required to analyze the results of solid-state NMR experiments, that is, chemical shifts and electric field gradients on atoms of interest. A detailed review of the CASTEP NMR formalism and numerous examples of practical applications are discussed in Bonhomme et al [144].

5. **CCDC**
   The CCDC module allows you to query Cambridge Structural Database (CSD) instances installed locally or hosted on remote servers from Materials Studio.
   CCDC contains the following tools:

   - ConQuest Search provides an interface to the CCDC ConQuest query engine of the CSD database. You can search the CSD for instances of structure fragments loaded in Materials Studio or search the CSD using a structure reference or chemical name. Alternatively, you can transfer your substructure from Materials Studio directly into the ConQuest desktop application.
   - Motif Search allows you to analyze hydrogen bond motifs formed between particular functional groups in a crystal structure. You can search the CSD to identify observed interaction motifs and obtain their probability distribution. You can categorize a list of input crystal structures with respect to hydrogen bond motifs. The predicted hydrogen bond motifs can be scored against the statistical frequency of these motifs found in the CSD.

6. **Conformers**
   The Conformers module provides methods for searching the conformational space of nonperiodic molecular systems in order to derive a reasonable sampling of the low energy conformations. The primary degree of freedom explored is the set of rotatable torsion angles of the molecular system. The Conformers module can perform both systematic and stochastic (random) searches.
   Once you have performed a Conformers run and obtained a set of conformers, the Conformers module allows you to calculate a range of descriptors, enabling you to perform a detailed analysis of the structures. Conformers also gives you the option of performing an extended search on the output from a run. You can select a subset of the conformers produced by an initial Conformers run and carry out a secondary search around each of these structures.

7. **DFTB+**
   The Density Functional based Tight Binding (DFTB) method is based on a second-order expansion of the Kohn-Sham total energy in Density Functional Theory (DFT) with respect to charge density fluctuations. The zeroth order approach is equivalent to a common standard non-self-consistent (TB) scheme, while at second order a transparent, parameter-free, and readily calculable expression for generalized Hamiltonian matrix elements can be derived. These are modified by a self-consistent redistribution of Mulliken charges (SCC).
   Besides the usual "band structure" and short-range repulsive terms, the final approximate Kohn-Sham energy additionally includes a Coulomb interaction between charge fluctuations. At large distances this accounts for long-range electrostatic forces between two point charges and approximately includes self-interaction contributions of a given atom if the charges are located at one and the same atom. Due to the SCC extension, DFTB can be successfully applied to problems where deficiencies in the non-SCC standard TB approach become obvious.
   Materials Studio includes DFTB+, which is the latest implementation of the DFTB method. It is being developed in the group of Prof. Thomas Frauenheim at the Bremen Center for Computational Materials Science.

8. **DMol^3**
   DMol^3 combines computational speed with the accuracy of quantum mechanical methods to predict materials properties both reliably and quickly. Extremely versatile and can be applied to research problems in chemistry, materials science, chemical engineering, and solid state physics.
   The DMol^3 module allows you to model the electronic structure and energetics of organic and inorganic molecules, molecular crystals, covalent solids, metallic solids, and infinite surfaces.

9. **Amorphous**
   Forcite is a collection of molecular mechanics tools that allow you to investigate a wide range of systems. The key approximation is that the potential energy surface, on which the atomic nuclei move, is represented by a classical force-field. Forcefields are developed by parameterizing data from experiment and high level quantum mechanical calculations.
   Typically, Forcite is used to optimize the geometry of a system prior to a molecular dynamics simulation or a quantum mechanical calculation.

10. **Gaussian**
    Materials Studio's Gaussian® 2003 User Interface allows you to access the Gaussian 03 or Gaussian 09 server to model the structure and energetics of molecules using Hartree-Fock (HF) and density functional theory (DFT) methods. With Gaussian you can predict the structure, energies, thermodynamic properties, NMR and vibrational spectra of molecular systems.
    The Materials Studio Gaussian® 2003 User Interface currently only exposes a limited subset of Gaussian 03 and Gaussian 09 functionality. However, by using the Gaussian Job Files option, the full functionality of Gaussian can be accessed. Neither the Gaussian 03 nor Gaussian 09 server application is included in the Materials Studio installation and must be purchased separately from Gaussia
    A detailed description of the Gaussian program can be found on the Gaussian, Inc. website http://gaussian.com/

11. **GULP**
    The General Utility Lattice Program (GULP) is a program for performing a variety of simulations on 3D periodic solids, gas phase clusters, and isolated defects in bulk materials. In particular, GULP is designed to handle both molecular solids and ionic materials through the use of the shell model.
    GULP is able to perform a variety of tasks relating to three-dimensional solids. Although it started life as an attempt to produce an input file-driven program for interatomic potential fitting, it has now expanded to encompass energy minimization, phonon calculations, and other useful facilities. In many respects, GULP parallels the suite of codes THBFIT, THBPHON, CASCADE, and, to some extent, PARAPOCS. One major difference is that GULP tries to use the crystal symmetry both to make it easier to generate structures and, where possible, to speed up the calculations by only considering the asymmetric unit.
    GULP can also perform calculations on nonperiodic systems, subsuming what was once a separate program called CLUSTER. This facility is useful when calculating defect energies for molecular defects. It also allows the combined fitting of potentials to bulk and cluster information.

12. **Kinetix**
    Kinetix is a general purpose program for the simulation of chemical and physical processes taking place at crystal surfaces using kinetic Monte Carlo methods, KMC. The implementation of the KMC approach is based on the CARLOS program developed at Eindhoven Technical University. An in-depth discussion of the technology can be found on the Prof. Jansen's website https://www.tue.nl/en/.

13. **Mesocite**
    Mesocite is a collection of molecular mechanics tools that allow you to investigate a wide range of systems. The key approximation is that the potential energy surface, on which the beads move, is represented by a classical forcefield. Forcefields are developed by parameterizing data from experiment. Currently two forcefields are available in Mesocite:

    - MS Martini
    - Shinoda2007

    In addition it is possible to run Mesocite using custom forcefields. Mesocite provides the ability to run energy, geometry optimization, dynamics, and dissipative particle dynamics calculations on mesoscale systems.

14. **MesoDyn**
    MesoDyn is a state-of-the-art mesoscale simulation program. It is a dynamic variant of mean-field density functional theory, providing a coarse-grained method for the study of complex fluids, their kinetics, and their equilibrium structures at large length and time scales. MesoDyn can analyze these morphologies both quantitatively and qualitatively.
    Unlike earlier equilibrium approaches to the study of phase morphologies, MesoDyn recognizes the dynamic nature of the structures. The types of structures that MesoDyn enables you to study typically have dimensions in the range 10-100 nm. Such objects naturally self-assemble in materials such as soaps and detergents and contribute to the unique properties of such materials. These topological effects can also be seen in polymer materials, where processing often 'freezes in' complex structures that critically affect materials properties.

15. **Morphology**
    Morphology allows researchers both to study particle shape and to consider the effects of altering the growth rate of particular faces on crystal morphology. In particular, Morphology can look at the effect of tailor-made additives in modifying growth. Knowledge of shape and aspect ratio is essential to understanding packing, flow problems, clogging of filters, and other problems. The Morphology module can also provide insight into other properties, such as the texture of powders and polymorphism. Morphology's application areas include pharmaceuticals, agrochemicals, food sciences, petrochemicals, cements, and commodity and specialty chemicals.

16. **ONETEP**
ONETEP is a revolutionary quantum mechanics-based program designed specifically for calculations on large systems. ONETEP employs density functional theory (DFT) in the density matrix formulation. The density matrix is a quantity which is exponentially localized in insulators and its diagonal elements are equal to the charge density of electrons. In ONETEP, the density matrix is expressed in terms of special maximally localized functions, non-orthogonal generalized Wannier functions (NGWFs).
ONETEP is a linear scaling method, so that the time required for the total energy calculation increases linearly with the number of atoms. This scaling is a direct consequence of the localization of NGWFs. Typical applications of first-principles quantum mechanics calculations with ONETEP include studies of surface chemistry, structural properties, the configurations of large molecular systems, and the structure and energetics of nanotubes. ONETEP can also be used to study the properties of defects (vacancies, interstitials, substitution impurities, grain boundaries, and dislocations) in semiconductors and ceramic materials. A detailed description of ONETEP technology has been presented in a review by Skylaris et al [145]

17. **Polymorph**
Polymorph allows you to predict potential stable or metastable crystal structures of a given compound directly from the molecular structure. It has been developed for polymorph prediction of fairly rigid, non-ionic or ionic molecules composed mostly of carbon, nitrogen, oxygen, and hydrogen. The approach used in Polymorph is based on the generation of possible packing arrangements in all reasonable space groups to search for low lying minima in the lattice energy surface. Polymorph can be used in two ways:

    - When experimental powder data is available, it may be used to aid the identification of the correct crystal structure from the list of generated trial structures using the Powder Comparison feature and to refine the structural parameters using the Rietveld method in Reflex.
    - Ab initio prediction of polymorphs when experimental powder data is not available.

    Polymorph Analysis allows you to collate results from multiple Polymorph runs into a study table. Data can be sorted, filtered, and plotted. In addition, you can carry out further analysis of the results, including comparison of simulated and

experimental X-ray powder patterns and evaluation of crystal similarity between structures in the study table and a reference crystal.

18. **QMERA**
    QMERA is a program that allows combined quantum mechanical (QM) and molecular mechanics (MM) forcefield calculations to be performed using the ChemShell environment. ChemShell is a computational chemistry environment, based on the Tcl interpreter, that takes over the communication and data handling for hybrid QM/MM calculations, leaving the time-consuming energy evaluations to specialized external codes (visit the ChemShell home page for further details).
    Mixed QM/MM calculations involve the division of a system into two parts: the central "chemically active" QM region ("I"), and the surrounding "outer" MM region ("O"). Treating the "central" part of the system quantum mechanically allows the electronic structure and its changes (for example bond breaking and formation in a chemical reaction) to be modeled in a concise way. The remaining portion of the system is described using molecular mechanics, with the two regions being allowed to interact through use of appropriate potentials.
    QMERA provides both mechanical and electronic embedding schemes for treatment of the QM/MM interactions. Dangling covalent bonds between the QM and MM regions are capped with hydrogen 'link' atoms. Geometry and Transition state optimizations in QMERA can be carried out using a range of minimizers, including a linear-scaling delocalized coordinate algorithm. QMERA employs DMol3 as the QM server and GULP for the MM calculations.

19. **QSAR**
    The QSAR module is a comprehensive set of tools for creating statistical regression models between experimental information ('activity') and molecular level characteristics ('descriptors'). Additional functionality within the module allows the user to probe the diversity of the training set and correlations between individual descriptors and the activity.
    The descriptors that can be calculated include a wide range of properties. These can be supplemented by characteristics calculable with other modules: Forcite, VAMP, fast descriptors. These additional descriptors allow a wider range of material characteristics to be accurately modeled.

    - QSAR Statistics allows you to view and analyze your results
    - QSAR Models can be used to calculate dependent variables, descriptors, and properties from data in a study table.

20. **Reflex**
    Reflex simulates X-ray, neutron, and electron powder diffraction patterns based on models of crystalline materials. Reflex aids the determination of crystal structure, assists the interpretation of diffraction data, and is applied to validate the results of experiment and computation.
    Powder Diffraction allows you to monitor the effects of structural changes on powder patterns and to compare the patterns obtained from theoretical crystal structures directly with experimental diffraction data. A variety of experimental conditions and correction factors can be applied to provide close agreement between simulation and experiment. The Powder Diffraction tool can be used for X-ray, neutron, and electron radiation.

21. **Sorption**
    The Sorption module allows you to simulate a pure sorbate (or mixture of sorbate components) absorbed in a sorbent framework, that is, a three-dimensional periodic structure with pores of a size and shape suitable to accommodate the sorbate molecules. Typical examples of sorbents include microporous and mesoporous materials such as zeolites, aluminophosphates, clays, nanotubes, polymer membranes, silica gels, activated carbons, and metal-organic frameworks. Characterizing the sorption behavior of these materials is of importance in the fields of catalysis and separation technology.
    The information that can be obtained from Sorption simulations includes adsorption isotherms, binding sites, binding energies, global minimum sorbate locations, density and energy fields, energy distributions, sorption selectivities, solubilities, isosteric heats, and Henry constants.
    The Sorption module has been designed to be used by experimentalists as well as computational chemists. Output-analysis features such as automatic calculation and display of isotherms make it easy to directly compare Sorption data with experimental results.

22. **Morphology**
    The Synthia module allows you to make rapid estimates of polymer properties using empirical and semiempirical methods.
    Synthia can predict a wide range of thermodynamic, mechanical, and transport properties for bulk amorphous homopolymers and random copolymers. The key advantage of Synthia is that it uses connectivity indices, as opposed to group contributions, in its correlations; this means that no database of group contributions is required, and properties may be predicted for any polymer composed of any

combination of the following nine elements: carbon, hydrogen, nitrogen, oxygen, silicon, sulfur, fluorine, chlorine, bromine.

23. **VAMP**
    VAMP is a semi-empirical molecular orbital package for molecular organic and inorganic systems. VAMP is an ideal intermediate module between force-field and first principles methods and is capable of rapidly calculating many physical and chemical molecular properties. BIOVIA Materials Studio VAMP is optimized to be numerically stable and fast, enabling most calculations to be run interactivewly on a PC.

3.1.3 System Requirements for Materials Studio

As you use Materials Studio to create structures, run calculations, gather and analyze results, the disk space required will increase to allow storage of both results and interim job files on the server. You should ensure that the server you use for Materials Studio has enough disk space to accommodate your long term space requirements [146].

3.1.3.1 Materials Visualizer Requirements

This section describes the requirements of the Materials Visualizer only. The Materials Visualizer is the core client module in Materials Studio; providing modeling, analysis, and visualization tools. It cannot set up or launch jobs unless installed in conjunction with Materials Studio Server.

TABLE 3.1: Supported Operating Systems

Operating System	Supported Versions
Microsoft Windows Professional and Enterprise	10 (64-bit only) 7 SP1 (32-bit and 64-bit)

The hard disk space required for installation can vary between 1 GB for Materials Visualizer only and 4 GB if you install the complete Materials Studio server and client. The Materials Visualizer can only be installed on Windows. Additionalspace will be required ifsystem updates are necessary, for example for .NET, runtimes, and libraries. To achieve a more satisfying experience with Materials Studio, particularly in terms of the client software, it is highly recommended that your system be substantially better than the minimum specification above. This is particularly important if running server software locally on the same computer as the client software.

TABLE 3.2: Hardware Requirements

Component	Minimum Hardware	Recommended
Processor	Intel® Core™ i5 or equivalent	Intel Core i7 or equivalent
RAM	4 GB	16 GB
Available hard disk space for installation	1GB	4 GB
Display	1366 × 768 display resolution 24-bit	1920 × 1080 display resolution 32-bit

Attention to the following areas can make a significant improvement to your overall user experience and enjoyment of the software:

- Memory - the more RAM your computer has, the better.
- A good OpenGL® graphics card can make a significant difference to the graphics performance.
- The higher the display resolution, the more flexibility you will have in displaying and managing document and dialog windows.
- Mouse - although not absolutely necessary, a two-button mouse with a wheel or a touch pad is strongly recommended. It will make the more complex structure manipulations easier and increase your efficiency and enjoyment of Materials Studio.

For example, a PC with 16 GB RAM, a screen resolution of 1920 × 1080, and a good OpenGL graphics card should perform well. PC hardware capabilities are currently advancing so rapidly that a new commodity desktop PC would have significantly higher specifications than these.
If you are installing the Materials Visualizer and Materials Studio server on the same machine, it should satisfy the minimum server requirements.

3.1.3.2 Materials Studio Server Requirements

If you intend to run server applications in parallel on a Windows system that does not have a network connection, you should install the Microsoft Loopback Adapter by following instructions appropriate to your operating system.
The hard disk space required for installation can vary between 1 GB for Materials Visualizer only and 4 GB if you install the complete Materials Studio server and client. The Materials Visualizer can only be installed on Windows. Additional space will be required if system updates are necessary, for example for .NET, runtimes, and libraries.

TABLE 3.3: Supported Operating Systems

Operating System	Versions
Microsoft Windows Professional and Enterprise	Intel® Core™ i5 or equivalent and Intel Core i7 or equivalent
Microsoft Windows Server	2016 2012 R2
Red Hat Enterprise Linux	7/6
SuSE Linux Enterprise Server	11 SP4
CentOS	7

TABLE 3.4: Hardware Requirements

Component	Minimum Hardware	Recommended
Processor	Intel® Xeon® E5-1620 or equivalent	Intel Xeon Silver 41XX series or equivalent
RAM per core (at least two cores)	2 GB	8 GB
Available hard disk space for installation	4GB	4 GB

3.2 Conclusion

Materials Studio is software for simulating and modeling materials. It is developed and distributed by BIOVIA Company and is a complete modeling and simulation environment designed to allow researchers in materials science and chemistry to predict and understand the relationships of a material's atomic and molecular structure with its properties and behavior. Using Materials Studio, researchers in many industries are engineering better performing materials of all types, including catalysts, polymers, composites, metals, alloys, pharmaceuticals, batteries and more.
In our research we have utilized Material studio to perform and improve the properties of photo-anodes in dye sensitized solar cells application such as: the behavior of aggregation and adsorption of dyes on the photo-anodes, the electronic and optical properties of DSSC components using some of modules and codes in Material studio software as CASTEP, Adsorpor locator and Dmol^3. This has helped us to understand the interactions between dyes and photo-anodes and how to improve the performances of each layer and component in dye sensitized solar cell which leads to a high efficiency of DSSC.

Chapter 4

Investigation of $ZnTiO_3$ perovskite for DSSC applications

4.1 Introduction

To understand new materials, it is important first to determine their electronic states. Most material properties are a consequence of the behaviour of electrons. This applies not only to electrical properties, such as whether the material is a metal, a semiconductor, or an insulator, but also such characteristics as melting point, boiling point, modulus of elasticity, and chemical reactivity. Optical and magnetic functions can also be explained in terms of electronic states.

First-principles calculation (simulation) is an essential tool for determining these electronic states. This method uses quantum mechanics (first principles) as the sole basis to calculate electronic states, without resorting to empirical parameters determined by experiment. Electronic states are calculated entirely from the atomic species and their positions. If necessary, the positions of atoms can be determined by searching for minimum-energy configurations. Because no empirical parameters are necessary to obtain results in agreement with experiments, even unknown materials that do not yet exist can be calculated with confidence. That is, first-principles calculation can be used not only to understand existing materials, but also as a valuable tool for theoretical materials design tasks, such as predicting the physical properties of unknown materials in advance of experiment, narrowing down promising candidate materials, and predicting optimal composition. While a wide range of calculation methods fall under the term "first-principles calculation," density functional theory (DFT), which is based on the calculation of electron density distributions, is widely used because of its speed and accuracy.

DFT has become very popular for calculations in solid state physics since 1970s. Compare to other methods dealing with the quantum mechanical multibody problems,

LDA give satisfactory results with experimental data. But in quantum Chemistry area, DFT was still not accurate until 1990s, when the approximate ion methods were greatly refined to better model the exchange-correlation interaction. DFT is now a leading method for electronic structure calculations in many areas. However, it's still difficult to use DFT to treat the strongly correlated systems, band gap in semiconductors, and strong dispersion systems. So the development of DFT is going on [147].

TiO_2 and ZnO binary oxide films are extensively investigated as photo-anodes in dye-sensitized solar cells (DSSCs), due to their large surface area, high electron mobility and chemical stability features. Since both of TiO_2 and ZnO systems have their own advantages, combining both materials may yield a new hybrid system with higher performance. The perovskite $ZnTiO_3$ is expected to combine the benefits of both separate TiO_2 and ZnO systems, and is worth to study. The $ZnTiO_3$ perovskite is chosen here as ETM in DSSCs. It has electron mobility in the range (150e400 cm^2/V) [148],which is much higher than those in many known photoanodes, including TiO_2 and ZnO.

In this chapter , the interaction between N3 dye molecule and $ZnTiO_3$ perovskite surfaces is investigated. The ZnTiO3 ability to provide higher surface area than either ZnO or TiO_2 is assessed. The dye adsorption energy (Eads) onto $ZnTiO_3$ surface, compared to ZnO and TiO_2, is calculated. Both surface area and adsorption energy are necessary features for enhanced electron injection efficiency between the excited dye and the semiconductor conduction band, in DSSC systems.

4.2 Perovskite notion

Perovskite materials have emerged as the most promising and efficient low-cost energy materials for various optoelectronic and photonic device applications.
[149] The mineral perovskite $CaTiO_3$ in figure 4.1 is named after a Russian mineralogist, Count Lev Aleksevich von Perovski, and was discovered and named by Gustav Rose in 1839 from samples found in the Ural Mountains. Since then considerable attention has been paid to the perovskite family of compositions.

The general chemical formula used to describe the perovskite materials is $\mathbf{ABX_3}$ is shown in Figure 4.2, where A and B are cations with A larger than that of B and X is the anion usually oxides or halogens [150].In other hand, ABX_3 perovskite can be described as consisting of corner sharing $[BX_6]$ octahedra with the A cation occupying the 12-fold coordination site formed in the middle of the cube of eight such octahedra. The unique physical properties of perovskite materials such as:

FIGURE 4.1: Crystals of $CaTiO_3$ perovskite on matrix.

- high-absorption coefficient
- long-range ambipolar charge transport
- low exciton-binding energy
- high dielectric constant
- ferroelectric properties...etc.

Different classes of perovskite materials, such as inorganic oxide perovskites, alkaline metal halide perovskites and organic metal halide perovskites have gained a huge interest in optoelectronic and photovoltaic applications.

4.3 $ZnTiO_3$ perovskite

Dulin et Rase reported that there are three compounds existing in ZnO–TiO_2 system, including hexagonal $ZnTiO_3$, cubic Zn_2TiO_4 and cubic $Zn_2Ti_3O_8$ [151].
Zinc titanate ($ZnTiO_3$) has been widely investigated and useful candidate for applications in many fields such as:

- catalytic sorbent for desulfurization of hot coal gases[152].
- microwave dielectric ceramics [153, 154].
- paint pigment [155].

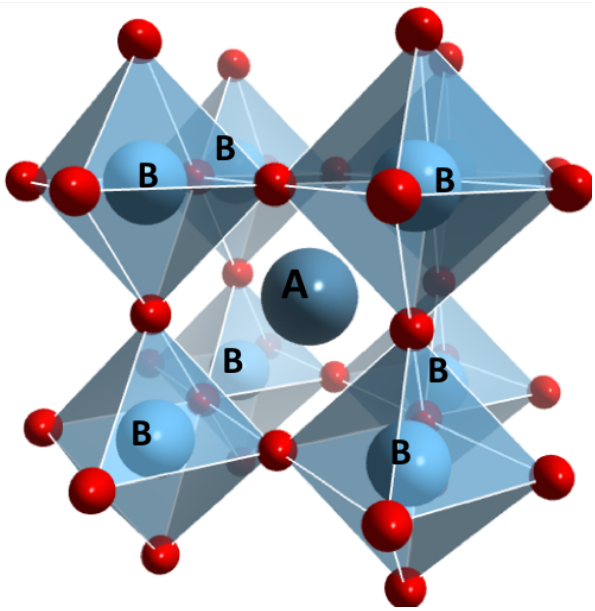

FIGURE 4.2: ABX_3 Perovskite structure, in which organic or inorganic cations occupy the A sites, whereas metal cations and halides occupy the B and X sites,respectively.

- gas sensors for the detection of NO, CO [156].
- nd photoluminescence materials [157].

However, in this work , **$ZnTiO_3$** hexagonal perovskite (see figure 4.3) is investigated as a photo-anode, with N3 ruthenium dye, to design a new photo-anode for dye sensitized solar cells (DSSCs).

4.4 Prediction of adsorption energies of (COOH@Oxides) systems.

As a first step and prior running any heavy calculation in Material studio software, we have utilized a module which called Adsorption Locator, it can be used as a preparatory and screening tool in two ways:

- to generate adsorbed configurations automatically, which can subsequently be used as starting points for DFT calculations.
- to use the forcefield method to obtain a ranking of the energies for each generated configuration, thereby indicating the preferred adsorption sites.

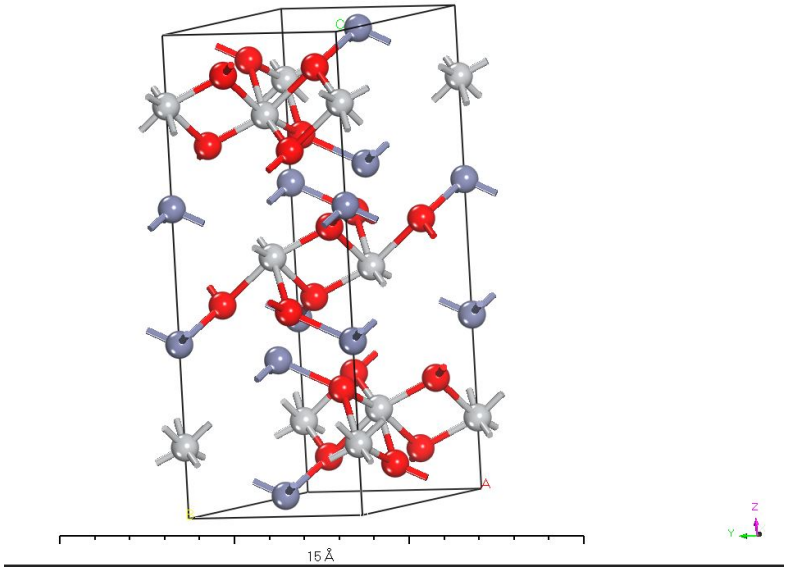

FIGURE 4.3: $ZnTiO_3$ hexagonal perovskite structure, in which Zn, Ti and O atoms are in gray, violet and red colors respectively.

That is well known from the literature, the adsorption of adsorbates onto substrates occurs through Carboxyl groups (COOH) of dyes which would be linked to substrate surface by three possible adsorption modes [158] (Figure 4.4):

- bidentate bridging (BB) mode.
- chelating (BC) mode.
- ester (ME) mode.

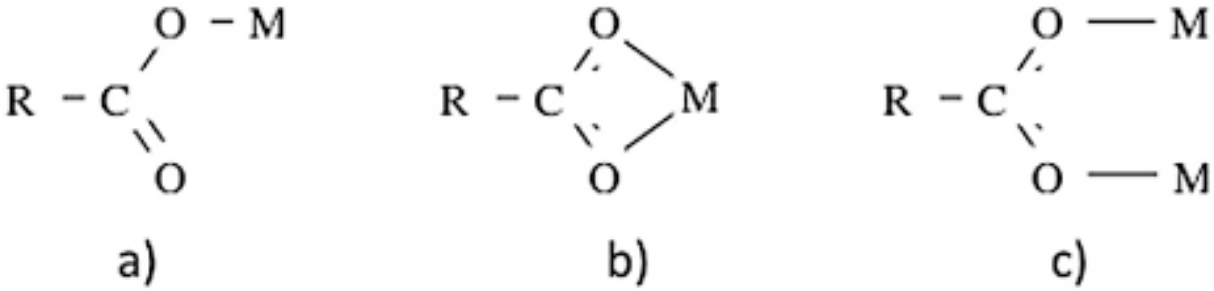

FIGURE 4.4: Graphical representation of the three possible carboxylate bonding modes: (a) monodentate ester-like, (b) bidentate chelating, (c) bidentate bridging.

In the first calculation, the rethunium dye (N3) has been reported as an adsorbate in our systems. However, we have only selected the (COOH) Carboxyl group molecule from the dye instead of the whole N3 dye molecule to study the prediction of energy

adsorption and the location of adsorption sites onto three different types of (101) surfaces substrate such as TiO_2 anatase, ZnO and $ZnTiO_3$ metal oxides (Figure 4.5).// The objective of this primary study is to explain the mechanism of adsorption, and therefore offer theoretical tool regarding the understanding of mechanism of (COOH) Carboxyl group.

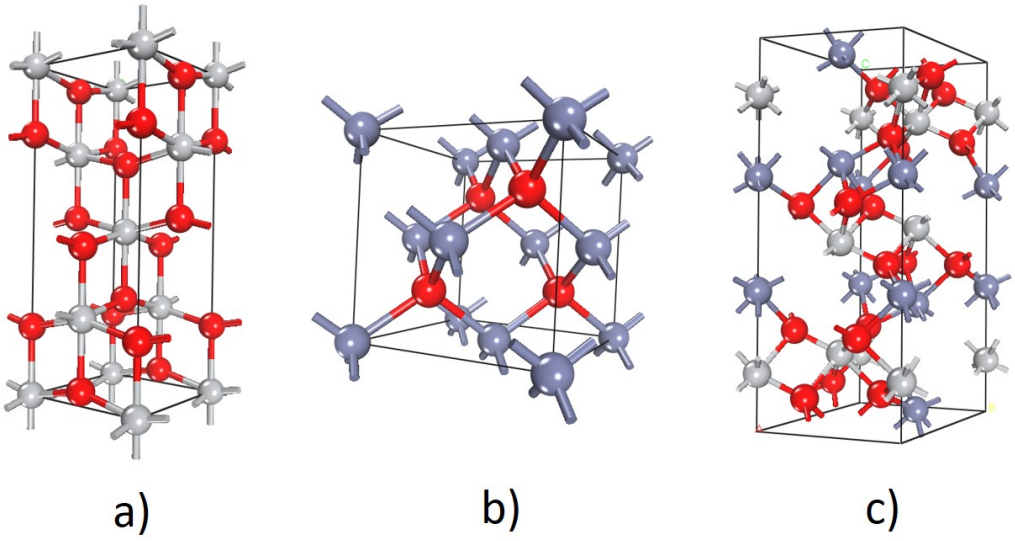

FIGURE 4.5: Structures of metal oxides a) TiO_2 anatase oxide b) ZnO oxide c) $ZnTiO_3$ perovskite

4.4.1 Model and computational details

The (COOH) Carboxyl group molecule have been optimized before adsorbing it onto the metal oxides surfaces (Figure 4.6), from material studio we select Forcite Calculation Module, on the Setup tab we change the Task to Geometry Optimization and then the Quality of calculation to Ultra-Fine, the covergence tolerance of energy, force and displacement are set to 2x10^{-5} kacl/mol, 0.001 kcal/mol/Åand 1x10^{-5} Åoptimization respectively. After that, Select the Energy tab and change the Forcefield to COMPASS and summation method of electrostatic and van der waals to Atom based the we lick the Run button.

For Metal oxides such as TiO_2, ZnO, $ZnTiO_3$, we cleave surface cutting to 101 (h k l) crystal plane, then we increase the Fractional Thickness to 5.The choice of the cutoff will always be a trade off between the accuracy and the time required for the calculation .However, The number of layers in the structure should be chosen so that the depth of the surface is greater than the non-bond cutoff used in the calculation. Using 5 layers of metal oxides gives a sufficient depthnthat the (COOH) Carboxyl group

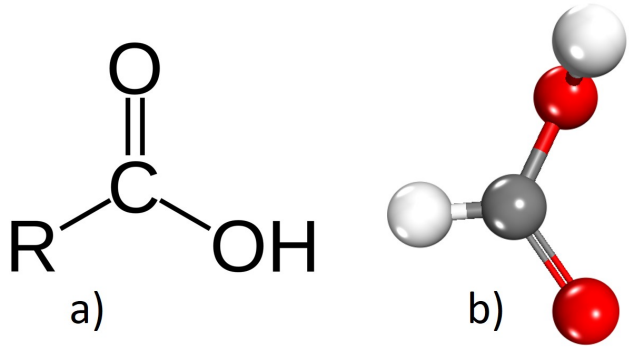

FIGURE 4.6: Carboxyl group (COOH) molecule, a) Structure of Carboxyl group , b) Carboxyl group geometry before optimization.

molecule will only be involved in non-bond interactions with metal oxides in the layer of the surface, without increasing the calculation time unreasonably. Next we build a 2x3x2 supercell in order to expose a more realistic surface area for docking the Carboxyl group molecules.In addition, the structure should be converted to have 3D periodicity, in this case, a distance of (20Å) has been applied between the metal oxides surfaces layer and the next layer beyond the vacuum, which is sufficient to prevent any non-bond interactions between the next repeat unit and either the metal oxide surface or the (COOH) molecule.(Figure 4.7).

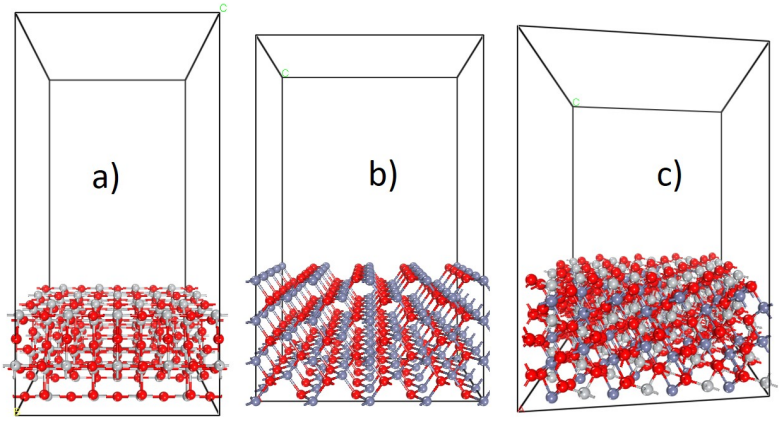

FIGURE 4.7: Metal oxides (101), surfaces with a thickness of 10Å, showing (a) TiO_2 b) ZnO c) $ZnTiO_3$ perovskite

To set up the Adsorption Locator calculation, from Energy tab we define the quality of calculation to Ultra-Fin and the forcefield type to COMPASS,then we specify the region around the substrate by atom set method, in which adsorbate configurations will be sampled. Concerning of maximum adsorption distance between substrate and adsorbate is unchecked, that is mean the adsorption locator will use a reasonable default

value for this distacne to allows the system to develop new configurations of (COOH @ Oxide systems). If the maximum adsorption distance is too short some configurations will not be accessible, and if it is too long no new configurations will be added.
In order to ensure that the energy results returned by Adsorption Locator are accurate, we have identified a suitable forcefield and we have used exactly the same energy and minimization settings in the Adsorption Locator run that we used to optimize the input structure of (COOH) Carboxyl group as the adsorbate components.

4.4.2 Geometry optimization of (COOH)

The geometry optimization process of (COOH) Carboxyl group is carried out using an iterative process, in which the atomic coordinates are adjusted until the total energy of a structure is minimized. Geometry optimization is based on reducing the magnitude of the calculated forces until they become smaller than defined convergence tolerances. Figure 4.8 shows the optimized structure of (COOH) Carboxyl group.

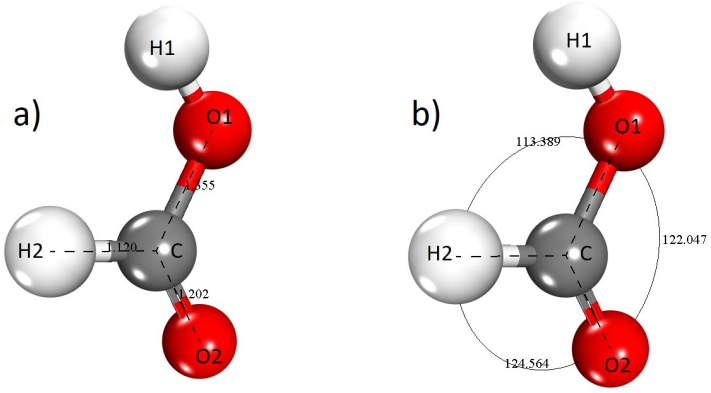

FIGURE 4.8: Geometry optimization form of (COOH) , a) bond length in (Å),b) bond angles in (deg).

Calculated bond length (angstrom) and angles (degrees) have been investigated in Table 4.1.However, the computed values of bonds and angles are slightly different to that From the Cambridge [159] Crystallographic Data Centre file, which indicates that Forcite calculation module in Material studio is efficient at geometry optimization of molecules.

TABLE 4.1: The mean structural parameters of (COOH) Carboxyl group

	value of bond length (Å)			value of bond angle (deg)		
	C-O1	C-O2	C-H2	H2-C-O1	H2-C-O2	O1-C-O2
Our simulation	1.335	1.202	1.2	112.389	124.564	122.047
ref [159]	1.31	1.21	-	112	123	-

Figure 4.9 shows the optimization energy curves for (COOH) Carboxyl group before adsorped onto the metal oxides surfaces. The initial structure total energy of (COOH) was 59.37 kcal/mol, after optimization the total energy has reduced to -17.81 kcal/mol under selected geometry optimization parametres in section 4.4.1.

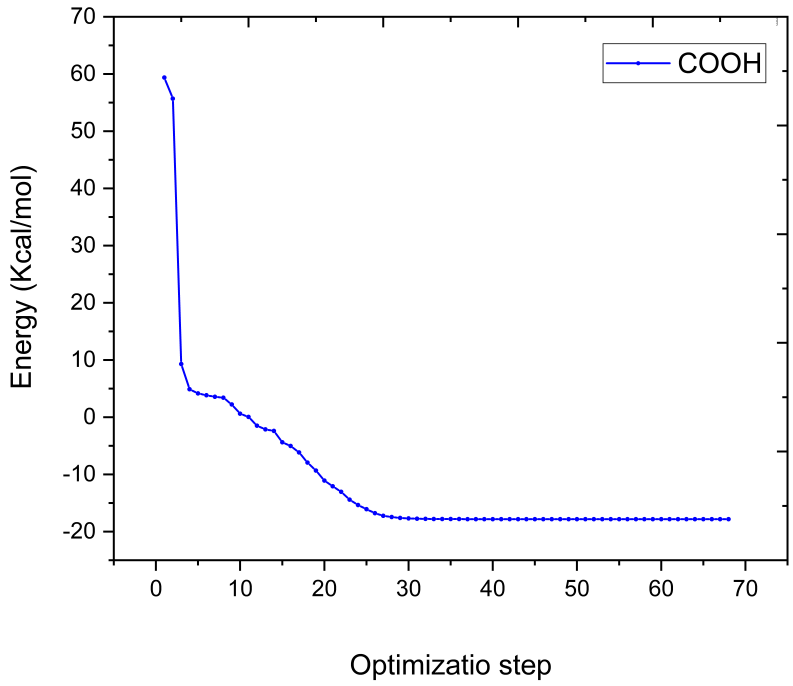

FIGURE 4.9: Optimization energy of the Carboxyl group (COOH) using Forcite calculation module

4.4.3 Monte-Carlo Simulation.

In this computational work, possible adsorption configurations have been identified by carrying out Monte Carlo searches (Described in Chapter 3 section **??**) of the configurations space and find the lowest energy for the whole system of the (Carboxyl group / Metal oxides(101) Surfaces) in Adsorption Locator module, as The temperature is first increased steeply to a high value, then it is slowly decreased to the final

value, allowing the system to settle to a state of minimal energy. The process can be repeated in a number of cycles to allow the system to explore states of still lower energies [160].
Adsorption Locator is a relatively new module in Materials Studio, and has already been used in a variety of cases to identify binding sites and study their energetics,for instance, of organic molecules on metal surfaces and nanoparticles.
The binding energy between the Carboxyl group and Metal oxides(101) Surfaces were calculated using the following equation [161]:

$$E_{ad} = E_{total} - (E_{surface} + E_{adsorbate}) \tag{4.1}$$

Where;
E_{total} is the total energy of the oxide surface and Carboxyl group.
$E_{surface}$ is the energy of the oxide surface without the Carboxyl group, and
$E_{adsorbate}$ is the energy of the Carboxyl group without the oxide surface.

4.4.3.1 Adsorption of COOH on TiO_2(101)

Outputs calculated by the Monte-Carlo simulation for adsorption energies of COOH molecule on TiO_2 (101) surface is shown in Table 4.2.The initial conditions are such that the substrate has a zero energy and COOH -O17.81572 kcal/mol. Data within the Table 4.2 include total energy, in kcal/mol[1], of the Carboxyl group/ TiO_2 (101) configurations. The total energy is defined as the sum of the energies of the Carboxyl group, the rigid adsorption energy and the deformation energy. In this study. In addition, adsorption energy in kcal/mol, reports energy released (or required) when the relaxed COOH molecule in aqueous solution are adsorbed on the TiO_2 (101) surface. The adsorption energy is defined as the sum of the rigid adsorption energy and the deformation energy for the COOH molecule. The rigid adsorption energy reports the energy, in kcal/mol, released (or required) when the unrelaxed COOH molecule (before the geometry optimization step) are adsorbed on the TiO_2 (101) surface. The deformation energy reports the energy, in kcal/mol, released (or required) when the adsorbed COOH molecule are relaxed on the TiO_2 (101)surface. Table 4.2 shows also that (dEads/dNi), which reports the energy, in kcal/mol, of TiO_2–Carboxyl group configurations where one of the COOH molecules has been removed.

TABLE 4.2: The output and descriptors calculated by the Monte Carlo simulation of Carboxyl group confirmations on TiO_2 anatase (101) surface

Structures	Total energy	Adsorption energy	Rigid-ads energy	Deformation energy	Carboxyle dEad/dNi
TiO2 (1 0 1)	0				
Carboxyle	-17.81572				
COOH/TiO2 - 1	-538.84941	-521.0337	-575.8295	54.79581	-521.0337
COOH/TiO2 - 2	-507.35364	-489.53792	-521.61447	32.07655	-489.53792
COOH/TiO2 - 3	-480.5224	-462.70668	-481.60359	18.89691	-462.70668
COOH/TiO2 - 4	-474.27069	-456.45498	-489.92254	33.46757	-456.45498
COOH/TiO2 - 5	-471.28584	-453.47012	-492.2884	38.81829	-453.47012
COOH/TiO2 - 6	-471.27308	-453.45736	-490.17787	36.7205	-453.45736
COOH/TiO2 - 7	-467.68124	-449.86552	-499.77467	49.90915	-449.86552
COOH/TiO2 - 8	-467.52649	-449.71078	-467.59147	17.88069	-449.71078
COOH/TiO2 - 9	-466.39109	-448.57537	-486.32315	37.74777	-448.57537
COOH/TiO2 - 10	-459.96987	-442.15415	-477.6321	35.47794	-442.15415
COOH/TiO2 - 11	-451.10495	-433.28924	-458.65108	25.36185	-433.28924
COOH/TiO2 - 12	-450.1552	-432.33948	-492.24549	59.906	-432.33948
COOH/TiO2 - 13	-450.05055	-432.23484	-456.10857	23.87373	-432.23484
COOH/TiO2 - 14	-447.92493	-430.10922	-477.70616	47.59694	-430.10922
COOH/TiO2 - 15	-445.72573	-427.91002	-462.96579	35.05577	-427.91002
COOH/TiO2 - 16	-442.70834	-424.89263	-458.08364	33.19102	-424.89263

It is quite clear from 4.2 that the value of adsorption energy of different configuration structure are negative. However, the sign (-) means that the attraction between COOH and TiO_2 (101) srface could spontaneously occur, (adsorption takes place). The resultant configuration with the lowest and largest adsorption energies of the 16 possible configurations for COOH was -521.03 kcal/mol (-22.60 eV) and -424.89 kcal/mol (-18.42 eV) respectively. indicating the system with the most stable and stronger adsorption. A typical adsorption energy distribution of COOH adsorbed on TiO_2 (101) surface consisting of the total energy, average total energy, Van der Waals energy, electrostatic energy and intermolecular energy, using Monte Carlo simulations, is depicted in Figure 4.10.

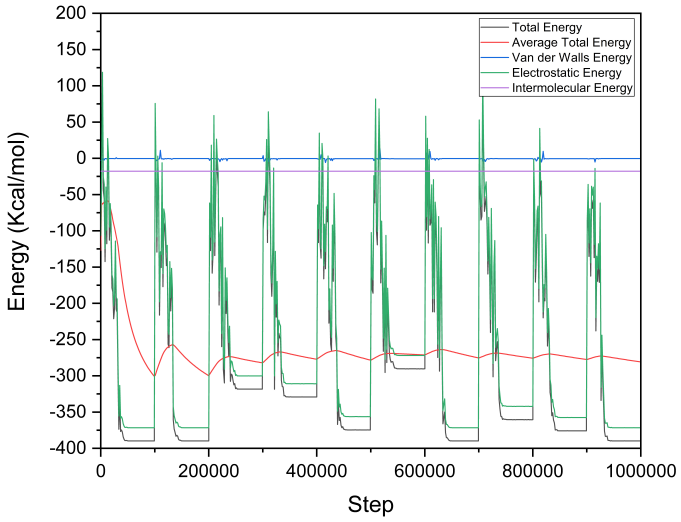

FIGURE 4.10: Energy profile of COOH molecule adsorbed on TiO_2 (101) surface.

The Metropolis Monte Carlo method in adsorption locator calculation provides four step types for a canonical ensemble: conformer, rotation, translation and regrowth. Side and top views of stable adsorption configurations of COOH adsorbed on TiO_2 (101) using adsorption locator is given in Figure 4.11.

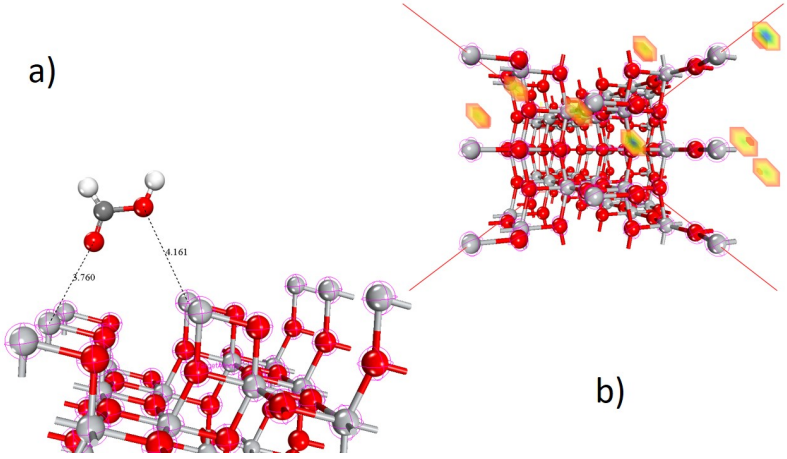

FIGURE 4.11: Equilibrium adsorption configurations obtained by adsorption locator module for one molecule of COOH adsorbed on TiO_2 (101). (a) The band distance between Ti-O atoms, (b) field of adsorption sites

In Figure 4.11 (a), shows the most suitable COOH molecule conformation adsorbed onto the TiO_2 (101) surface substrate, the distance between Ti atoms in TiO_2 (101) surface and O atoms in the COOH is 3.760Åand 4.161Å. In other hand, Figure 4.11 (b), displays a field of adsorption sites, the more likely adsorption areas are shown in green and less likely sites appear red color.

4.4.3.2 Adsorption of COOH on ZnO(101)

During the course of Monte Carlo simulation, adsorbate COOH molecule are randomly rotated and translated around the ZnO (101) substrate.
The configuration that results from one of these steps is accepted or rejected according to the selection rules of the Metropolis Monte Carlo method.The results of the simulation which is presented in a bar graph in Figure 4.12 shows that, the (COOH@ZnO(101)) system could have 192 different locations (sites) have different adsorption configuration. The largest and lowest negative adsorption energies value is -222.53 kcal/mol and -122.69 kcal/mol respectively.

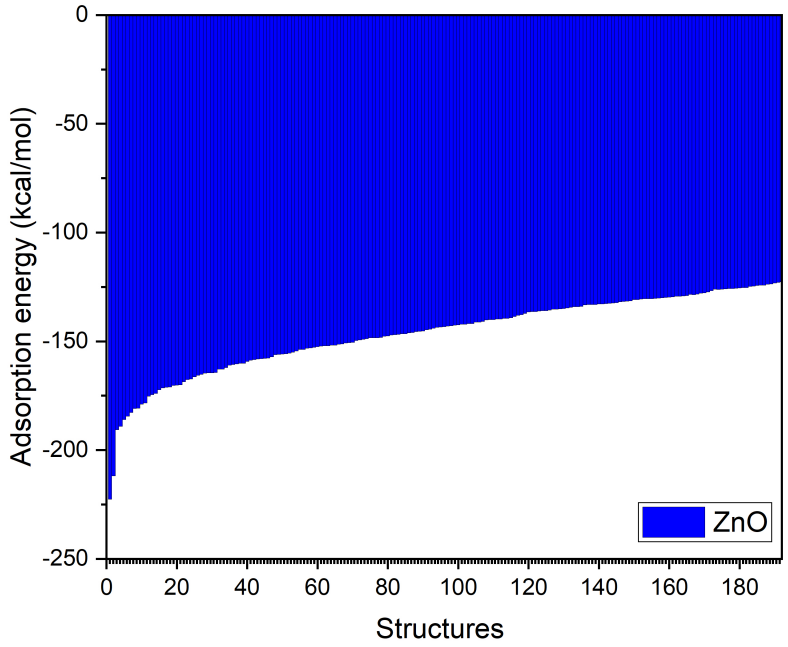

FIGURE 4.12: Adsorption energies of COOH adsorbed on Zno (101) surface.

Adsorption energy distribution of COOH adsorbed on ZnO (101) surface consisting of the total energy, average total energy, Van der Waals energy, electrostatic energy and intermolecular energy, using Monte Carlo simulations, is depicted in Figure 4.13.
The stable adsorption configurations of COOH adsorbed on ZnO (101) substrate using adsorption locator is given in Figure 4.14. As we can be seen from Figure 4.14 (a), the most suitable COOH molecule adsorbed onto the ZnO (101) surface substrate, the distance between Zn atoms in ZnO (101) surface and O atoms of Carboxyle group COOH is 4.141Åand 5.313Å. 4.14 (b),displays a field of adsorption sites, the more likely adsorption areas are shown in green and less likely sites appear red color.

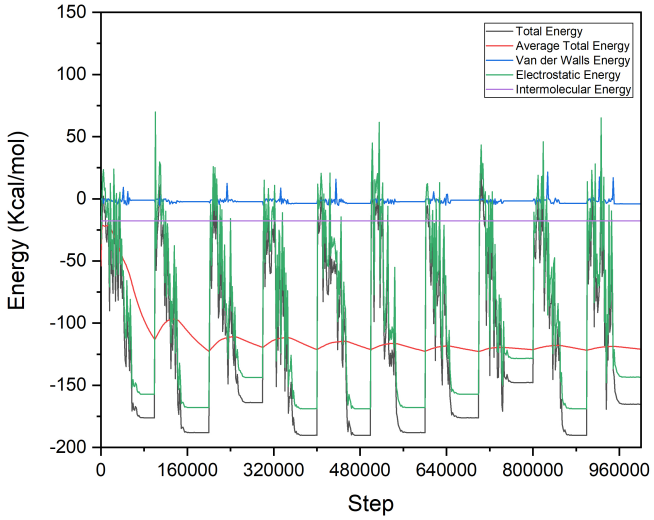

FIGURE 4.13: Energy profile of COOH molecule adsorbed on ZnO (101) surface.

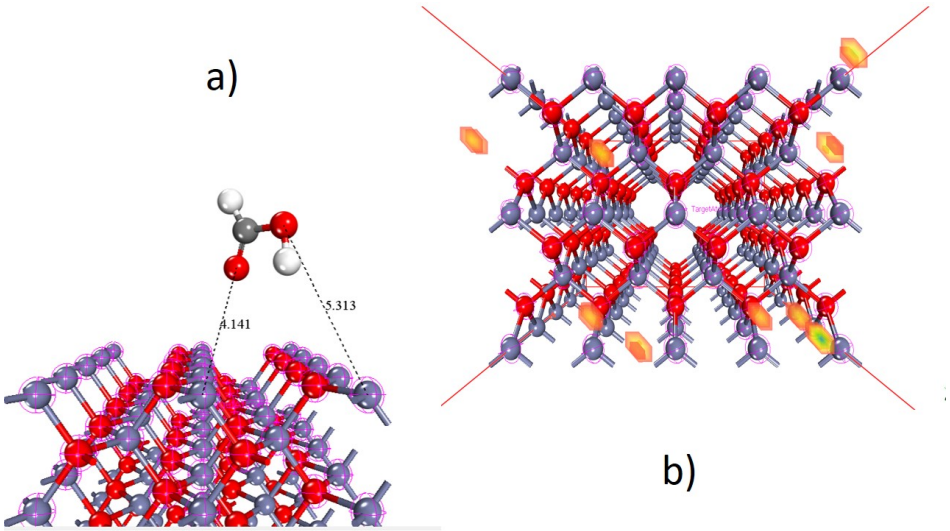

FIGURE 4.14: Equilibrium adsorption configurations obtained by adsorption locator module for one molecule of COOH adsorbed on ZnO (101). (a) The band distance between Zn-O atoms, (b) field of adsorption sites.

4.4.3.3 Adsorption of COOH on $ZnTiO_3$ (101)

The initial conditions are such that the substrate has a zero energy and COOH -17.81 kcal/mol. The resultant configuration with the lowest and largest adsorption energies of the 163th possible configurations of COOH onto $ZnTiO_3$ (101) surface were -305.30 kcal/mol and -405.25 kcal/mol respectively , where 163th possible configurations shows the adsorption power for COOH molecule on $ZnTiO_3$ (101) . Figure 4.15.

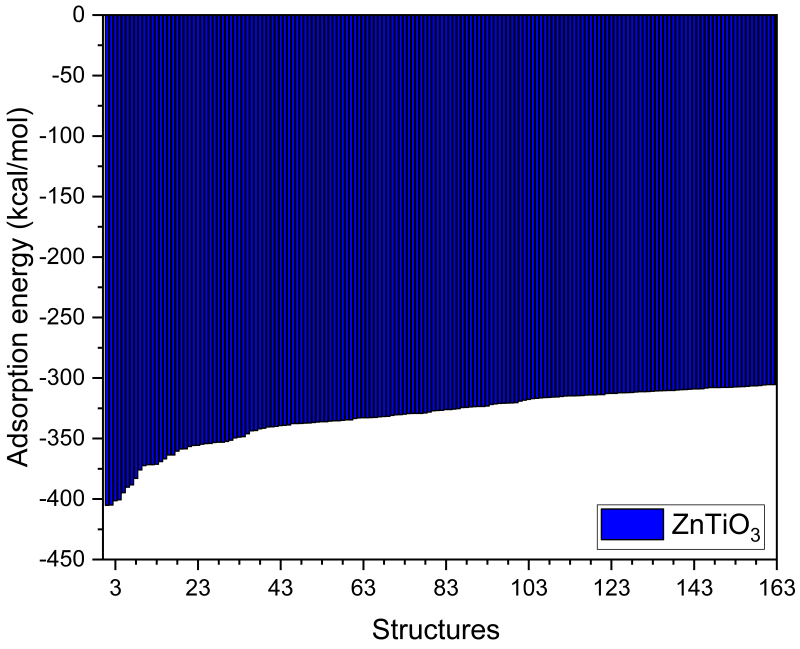

FIGURE 4.15: Adsorption energies of COOH adsorbed on $ZnTiO_3$ (101) surface.

A typical adsorption energy distribution of COOH adsorbed on $ZnTiO_3$ (101) surface con-sisting of the total energy, average total energy, Van der Waals energy, electrostatic en-ergy and intermolecular energy, using Monte Carlo simulations, is depicted in Figure 4.16.

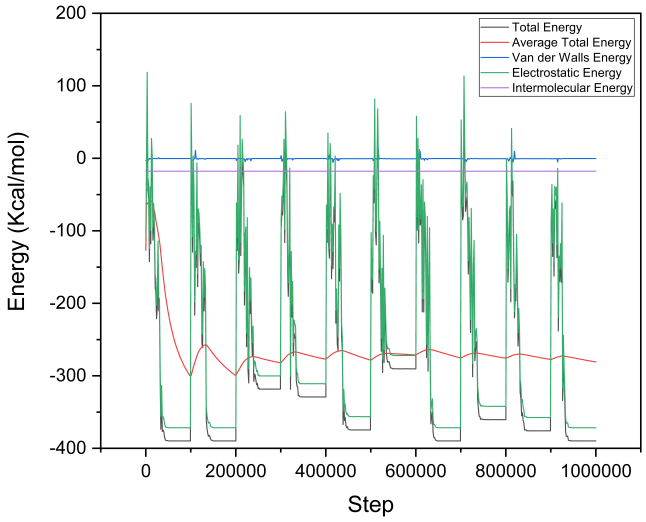

FIGURE 4.16: Energy profile of COOH molecule adsorbed on $ZnTiO_3$ (101) surface.

Figure 4.17 shows The stable adsorption configurations of COOH adsorbed on $ZnTiO_3$ (101) substrate using adsorption locator and the most suitable COOH molecule adsorbed onto the $ZnTiO_3$ (101) surface substrate, figure4.17 (a) illustrate the distance between (Zn and O) and (Ti and O) atoms in $ZnTiO_3$ (101) surface with is 5.075 Åand 4.648Årespectively. Figure4.17 (b),displays a field of adsorption sites, the more likely adsorption areas are shown in green and less likely sites appear red color.
According to the grand canonical ensemble Monte Carlo method adsorption model established for COOH Carboxyl group in the metals crystal surfaces adsorption calculation results, compared to COOH on TiO_2(101), ZnO (101) and $ZnTiO_3$ (101) surfaces, the COOH in TiO_2 (101) crystal face is stronger, the energy adsorption was calculated as the largest (-521.03 kcal/mol)and the length of O-Ti bond in COOH@TiO_2 is the shortest (3.760Å).

However, in ZnO (101) surface, COOH molecule could have more different locations (192 sites) have different adsorption configuration than in TiO_2 and $ZnTiO_3$ and ,but has low energy adsorption values, In Contrast, $ZnTiO_3$ (101) has showed to be more compatible with COOH molecules in aggregation which could have more than 160 sties for adsorption configuration and an energy adsorption up to 400 kcal/mol, leads to a high energy adsorption surface area with COOH.

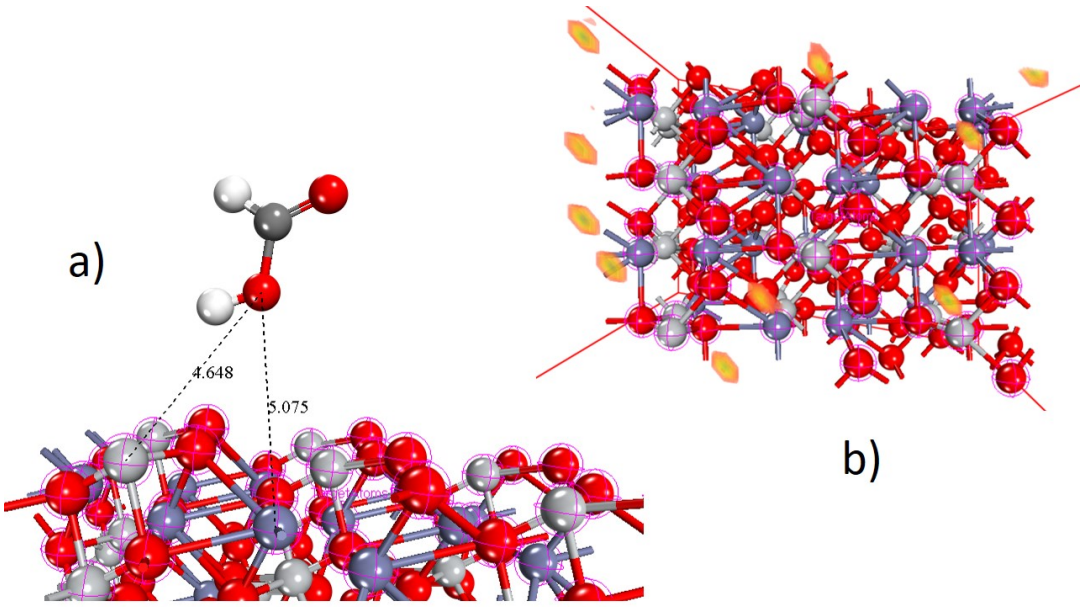

FIGURE 4.17: Energy profile of COOH molecule adsorbed on $ZnTiO_3$ (101) surface.

4.4.4 Conclusion.

Computational studies (Adsorption Locator) help to find the most stable dye conformation and adsorption sites for a broad range of materials. This information can help to gain further insight on dyes aggregation onto metal oxides in DSS, such as the most likely point of adsorption of dye on a photo-anode surface, the most stable site of dye adsorption, adsorption density of the dye and the binding energy of the adsorbed layer. According to Monte Carlo simulation method, the possible configurations number of carboxyl-group on metal oxide is ranked as $COOH@TiO_2 < COOH@ZnTiO_3 < COOH@ZnO$ and, In contrast, the largest energy adsorption of each system is classified as $COOH@TiO_2 > COOH@ZnTiO_3 > COOH@ZnO$, these results articulate that ,$ZnTiO_3$ Perovskite has collected between the two features that have been discovered in TiO_2 and ZnO metal oxides, $ZnTiO_3$ has experienced an adsorption energy value of -9.65eV and a configuration number of adsorption around 163 sites.

4.5 Adsorption of N3 ruthenium dye onto $ZnTiO_3$ (101) and (110) surfaces

Several perovskite (ternary metal oxides) semiconductors, such as $SrTiO_3$, $CaTiO_3$, $BaTiO_3$ and $ZnTiO_3$, have also been extensively investigated as photoanode materials for DSSCs. Despite that, TiO_2 is still one of the most studied systems due to its wide-band gap, electron mobility, transparency and high stability.

Ruthenium complex dye, cis-di(thiocyanato)-bis(2,2)-bipyridyl- 4,4(-dicarboxylate) ruthenium(II) (commonly known as N3) was used as an adsorbate onto these semiconductors. Lu et al. [162] studied the mechanism of N3 adsorption on rutile and anatase TiO_2 surfaces: (101), (001) and (100). Finnie et al. [163] reported that the carboxylic groups (eCOOH) of dyes are linked to TiO_2 surface by three possible adsorption modes, namely bidentate bridging (BB) mode, bidentate chelating (BC) mode and monodentate ester (ME) mode. ZnO has energy band gap value and conduction band edge position comparable to those of TiO_2 [164]. Moreover, ZnO is advantageousnover TiO_2 with its larger surface area. The N3 dye relative uptake onto ZnO is thus higher than onto TiO_2 [[165],[166], [167]]. However, the efficiency of DSSCs based on ZnO nanostructure is lower than that for DSSCs based on TiO_2 [168]. Since both of TiO_2 and ZnO systems have their own advantages, combining both materials may yield a new hybrid system with higher performance. The perovskite $ZnTiO_3$ is expected to combine the benefits of both separate TiO_2 and ZnO systems, and is worth to study. The $ZnTiO_3$ perovskite is chosen here as ETM in DSSCs. It has electron mobility in the range (150e400 cm^2/V) [169],which is much higher than thos in many known photoanodes, including TiO_2 and ZnO systems.

In the section, the interaction between N3 dye molecule and $ZnTiO_3$ perovskite surfaces is investigated. The $ZnTiO_3$ ability to provide higher surface area than either ZnO or TiO_2 is assessed. The dye adsorption energy (Eads) onto $ZnTiO_3$ surface, compared to ZnO and TiO_2, is calculated. Both surface area and adsorption energy are necessary features for enhanced electron injection efficiency between the excited dye and the semiconductor conduction band, in DSSC systems.

4.5.1 Model and computational details

The ground state geometry of N3 ruthenium dye has been optimized in ethanol solution and in gas phase using density functional theory (DFT) [170] with hybrid B3LYP-DNP [171] functional as implemented in DMOL3 computer code [172],[173]. The DNP

basis set (including polarization d-function) was selected, which is equivalent to the Gaussian09 6-31G(d, p) basis set with higher accuracy than other basis sets [174],[175]. The UV-Vis spectra of the dye were calculated using time-dependent density functional theory (TD-DFT) [176]. For the geometry optimization and optical properties, the convergence tolerance of energy was 1.0 x 10^5 Ha, and the maximum force was 0.0002 Ha/Åwith maximum displacement 0.0005 Å.

The geometry optimization and electronic properties of bulk $ZnTiO_3$ were performed using CASTEP code [177]. The BFGS algorithm and the generalized gradient approximation (GGA) of PBE scheme were employed [175]. DFT-D approach [178] was applied to treat the weak van derWaals (vdW) interactions between $ZnTiO_3$ atoms. The cut-off energy is considered to be 500 eV. For k-points sampling of the first Brillouin zone a k-point meshing of 8 x 8 x 2 as implemented with Monkhorst and Pack mesh grid [175] was used. Geometry optimization energy tolerance was set to 1.0 x 10^{-5} eV/atom and maximum Hellmanne-Feynman force was set to be 0.0003 eV/Å.

The two complexes of N3@$ZnTiO_3$ were made up by cleaving the bulk of zinc titanate crystal on two surfaces (101) and (110). Åthreeatomic layer super cell containing p(4 x 4) and p(3 x 3) surface unit cells were adopted to simulate the $ZnTiO_3$ (101) and (110) surfaces, which include (32 Zn atoms, 32 Ti atoms and 96 O atoms) and (36 Zn atoms, 36 Ti atoms and 108 O atoms) respectively.

4.5.2 Structure of the dye: geometry optimization

The geometry optimization of N3 dye is illustrated in Table 4.18. Ruthenium (II) ion is linked with four N atoms of two (2,2- bipyridine) (4,4-dicarboxylic acid ligands and two N atoms of two SCN ligands. In comparison, the dye structural parameters were compared with experimental data in Figure 4.3. Due to several conditions with the model in computational study, the calculated structure parameters are slightly different from the experimental results. The experimental structure parameters were obtained in the solid phase [179], while the calculated values were acquired in gas phase or in ethanol solutions. The experimental values are used for comparative purposes. Figure 4.3 shows that the structure parameters of R (Ru-N3) and R (Ru-N6) in gas and ethanol solution are closer to the experimental values compared to R (Ru-N1, N2, N4 and N5). However, the computational structural parameter values of N3 dye in ethanol solution are slightly different from gas phase.

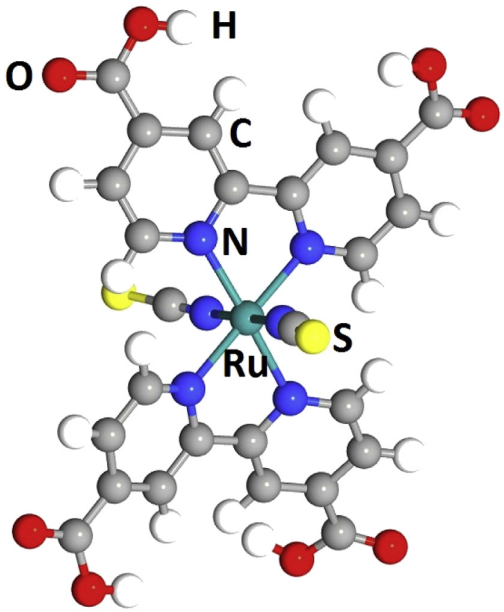

FIGURE 4.18: Optimization of N3 Ruthenium dye obtained by using B3LYP functional in ethanol solution..

TABLE 4.3: Experimental vs computational structural parameter values of N3 dye.

Structure parameters	Expt [179]	Computational results	
	Solid state (Å)	N3 gas phase (Å)	N3 in ethanol solution (Å)
R (Ru-N1)	2.03	2.19	2.18
R (Ru-N2)	2.03	2.18	2.17
R (Ru-N3)	2.05	2.06	2.06
R (Ru-N4)	2.04	2.16	2.17
R (Ru-N5)	2.04	2.17	2.17
R (Ru-N6)	2.04	2.09	2.08

4.5.3 Boundary conditions for molecular orbital

For N3 dye properties calculations, different DFT softwares, based on various functional approaches and basis sets,were used as shown in Table 4.4. HOMO and LUMO energies of ruthenium dye in ethanol solution comprise -5.44 eV (-0.20 Hartree) and -3.81 eV (-0.14 Hartree) respectively, whereas HOMO orbital energy level in gas phase is -5.71 eV (-0.21 Hartree) and LUMO is -4.08 eV (-0.15 Hartree). The HOMO levels are similar in both phases and in experimental data, with significant differences in LUMO level between gas, ethanol solution and experimental result. On the other hand, the

TABLE 4.4: Electronic and optical properties of N3 dye calculated in gas phase and ethanol solution, compared with other reported experimental and computational results based on DFT method.

				HOMO (E-dye)		LUMO (E*dye)		Band Gap (L-H)	Absorption peaks in UV/Vis spectra	
Type of Dye	Software	Basis set	Phase	Ha	eV	Ha	eV	eV	λ_1 nm (eV)	λ_2 nm (eV)
Ruthenium Dye R3	MS-DMol3	B3LYP - DNP	gas	-0.21	-5.71	-0.15	-4.08	1.63	537 (2.30)	650 (1.91)
	MS-DMol3	B3LYP-DNP	ethanol	-0.2	-5.44	-0.14	-3.81	1.63	522 (2.37)	641 (1.93)
	Gaussian03	B3LYP-3-21G	gas	-0.19	-5.17	-0.13	-3.53	1.63	391 (3.17)	650 (1.90)
	Gaussian03	B3LYP-3-21G	ethanol	-0.2	-5.44	-0.1	-2.72	2.72	285 (4.35)	543 (2.28)
	ADF	STO	gas	-0.16	-4.58	-0.15	-4.08	0.5	496 (2.5)	984 (1.27)
	ADF	STO	ethanol	-0.16	-4.58	-0.13	-3.51	1.12	433 (2.86)	629 (1.97)
	Experimental	-	ethanol	-0.2	-5.2	-0.13	-3.52	1.68	385 (3.22)	530 (2.33)

present calculated band gap value (LUMO - HOMO = 1.63 eV) for N3 dye in ethanol solution was more comparable to experimental value (1.68 eV) [180] than literature values (2.72 eV) and (1.12 eV). The slight differences in values of HOMO and LUMO levels, between experimental and theoretical values, are due to the density functional theory (DFT) method itself.

As mentioned in computational details, the B3LYP-DNP (including d-function polarization) basis set in MS-DMol3 software is equivalent to the B3LYP-3-21G/6-31G(d,p) basis sets in Gaussian09 software. Thus the discussion of the optical and electronic properties of N3 dye in different basis sets confirms the comparability between the two basis sets. Moreover, it is widely accepted that the calculation data are not always in good agreement with the experimental data, but DNP basis set is much better yield a good agreement with the experimental data than 3-21G (d,p) basis set in ethanol phase (see Table 4.4) such as band gap and HOMO and LUMO energies.

4.5.4 Absorption spectra of N3 dye

4.5.4.1 Before adsorption

An efficient solar cell sensitizer should adsorb strongly to the oxide semiconductor surface via anchoring groups, and exhibit intense absorption in the visible region of the spectrum [181]. The GGA-PPE approach using solvation model simulates the UV-Vis absorption spectra 400-800 nm of N3 dye in gas phase and ethanol solution (Figure 4.19). The λ (522 nm) for N3 dye in ethanol solution is higher in energy and intensity

than λ (537 nm) in gas phase. In contrary, bands for N3 in gas phase (λ at 650 nm) and for ethanol solution ((λ at 641 nm) have comparable intensities and wavelength values. The first higher in-solution absorption peak (λ 522 nm is located between 450 and 600 nm, as the highest experimental intensity for N3 dye [182]. Furthermore, solvent has an impact on UV spectra [**?**]. The presence of specific and non-specific interaction between the solvent and the solute molecules is responsible for the change in the molecular geometry and electronic structure of the solute, as shown in Table 4.4. Therefore, in comparison with gas phase, the blue shift of the absorption spectra in ethanol is due to the effect of solvation mode through interactions between the N3 dye (solute) and ethanol solvent molecules.

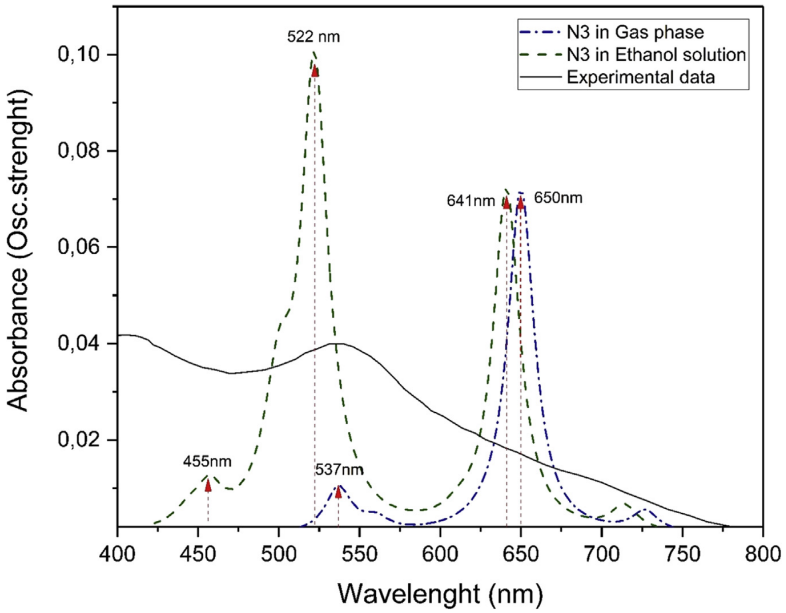

FIGURE 4.19: The UV/Vis absorption spectra of N3 dye before and after adsorption on (110) and (101) ZnTiO3 .

4.5.4.2 After adsorption

The anchoring modes of dyes onto the photoanode of DSSC may affect the absorption spectra. UV-Vis spectra of the N3 dye adsorbed on both (110) and (101) $ZnTiO_3$ perovskite surfaces are displayed in Figure 4.20. This figure shows a considerable difference between UV-Vis spectra for the free and the adsorbed N3 dye systems. However, in N3 dye adsorbed on (110) surface case, there is a red shift in absorption spectra and a peak with largest wavelength is located at 525-650 nm. Hence, the wavelength corresponding to the maximum absorption is 725 nm. In contrast, when the ruthenium dye is aggregated onto (101) surface, the absorption peaks shift to 650-900 nm wavelength compared to 400-725 nm in free dye case.

In addition, the maximum intensity absorption peak is located at 773 nm,which is calculated to be higher than that for free dye as well. The UV-Vis spectral differences confirm an efficient interaction between N3 and Zinc titanate oxide, by virtue of the carboxylic functional groups present in the N3 dye molecule. According to λ_{max}, the oscillator strength (f) is another feature to enhance the power conversion efficiency (PCE). The light harvesting efficiency (LHE) is related to oscillator strength, at its λ_{max}, as described equation 4.2 [**?**]:

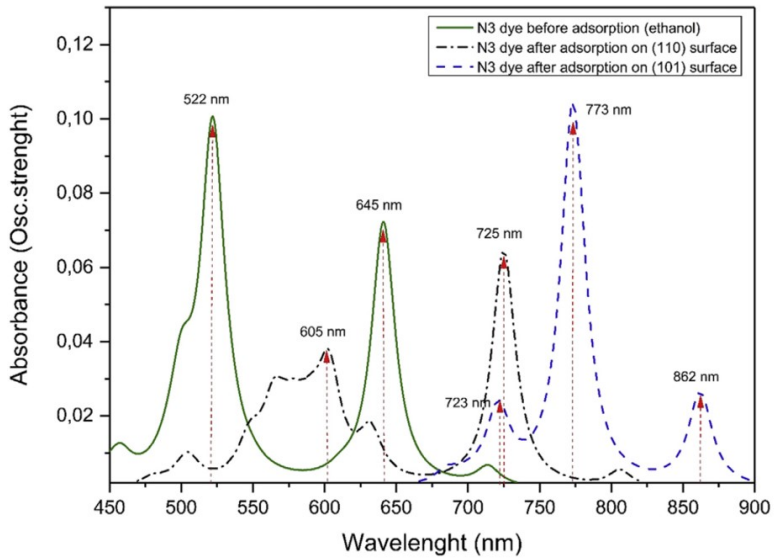

FIGURE 4.20: The UV/Vis absorption spectra of N3 dye in gas and ethanol solution.

$$LEH(\lambda) = 1 - 10^{f} \tag{4.2}$$

TABLE 4.5: The LHE values of free and adsorbed dye in gas and ethanol solution.

		λmax nm	**Oscillator strength**	**LEH**
Gas phase	Free dye	537 (650)	0.01 (0.073)	0.02 (0.15)
Ethanol solution	Free dye	522 (641)	0.10 (0.070)	0.19 (0.14)
	Adsorbed dye on (110) surface	725	0.06	0.13
	Adsorbed dye on (101) surface	773	0.11	0.22

The LHE values of free and adsorbed dye in gas and ethanol solution are listed in Table 4.5. In ethanol solution, the calculated LHE for N3 dye (0.20) is higher than (0.02) in gas phase, due to the largest oscillator strengths of 0.10 and 0.01 for the two systems, respectively. However, LHE of two absorption peaks between 600 and 700 nm wavelengths were 0.15 in gas phase and 0.14 in ethanol solution, which is a slight difference. These results indicate that the solvation mode significantly affects the LHE value. In case of N3 dye attached to $ZnTiO_3$ film surface, the LHE of N3/(110) and N3/(101) were 0.13 and 0.22, respectively, which is higher than values of (101) surface. This means that, the adsorption behavior of N3 dye onto the photoanode may improve the LHE and consequently the power conversion efficiency (PCE) of DSSCs.

4.5.5 Electronic structure of $ZnTiO_3$

The lattice parameters and structural properties of hexagonal $ZnTiO_3$ have been computed using different functional approaches as listed in Table 4.6 and schematized in Figure 4.21. It is clear that the present calculations are in good agreement with experimental values. Indeed, GGA-PBE approach including TS scheme for DFT-D correction method [183] is the best function leading to closest value to experimental data.

TABLE 4.6: The structural properties of hexagonal $ZnTiO_3$ calculated by different functional approach.

Functional	**Lattice parameter values (Å)**			**Band Gap value (eV)**
	a	b	c	
GGA-PBE	5.12	5.12	14.06	3.1
GGA-PBE/Grime	5.18	5.18	14.2	3.53
GGA-PBE /TS	5.08	5.08	14.2	3.12
Experimental [184]	5.07	5.07	13.92	3.18

The band structure graph in Figure 4.22a indicates that $ZnTiO_3$ perovskite has a direct energy band gap located in the high point symmetry of M = (0 0.5 0), which corroborates with the experimental value (3.18 eV), as summarized in Table 4.6 [184]. The partial density of state of pure $ZnTiO_3$ surface, displayed in Figure 4.22b, involves 2p states of oxygen (O), 3d states of zinc (Zn) and 3d state of titanium (Ti). The valence band maximum (VBM) is bordered by oxygen atom, while the Ti atom determines the conduction band maximum (CBM). Consequently the zinc titanate has an energy band gap quite similar to that for TiO_2 (3.20 eV) [185], due to the fact $ZnTiO_3$ involves both ZnO and TiO_2[186].

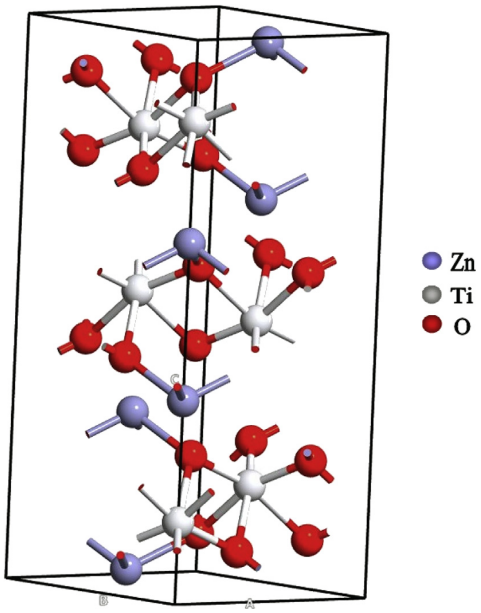

FIGURE 4.21: The crystal structure of $ZnTiO_3$ optimized by GGA-PBE-TS functional.

4.5.6 Adsorption of dye onto $ZnTiO_3$(101) and (110) surfaces

Adsorption energy (Eads) values of N3 dye on $ZnTiO_3$ in (101) and (110) surfaces were also computed using Dmol3 code. In Figure 4.23, the electronic density is higher in (101) surface (2D view) than in (110). Therefore, the adsorption energy on (101) surface is larger than on (110) surface. The adsorption of the dye on the semi-conductor surface is believed to occur in three modes. The bidentate bridging (BB) adsorption model is considered as the most stable and favorite mode, with one proton attached to the closer surface oxygen [187]. Stronger chemisorption enhances the electron injection from dye LUMO to the semi-conductor CB, which lowers electron-hole recombination and enhances PCE. Values of (Eads) are computed by equation 4.3 [188]:

$$E_{ads} = E_{(dye+ZnTiO_3)} - (E_{dye} + E_{ZnTiO_3}) \tag{4.3}$$

where E_{dye} and E_{ZnTiO_3} refer to the total energy of the dye and semiconductor before the adsorption process, respectively, and $E_{(dye+ZnTiO_3)}$ is the adsorption energy for the complex.

The carboxyl (COOH) groups of N3 dye adsorbed on $ZnTiO_3$ (101) surface via the Bidentate Bridging (BB) model, are shown in Figure 4.24a. Zn and Ti atoms are moderately reactive and may combine with oxygen or other non-metals. With their valence shell electrons, both atoms can release electrons necessary to make bonds with the carboxyl group of the N3 dye. The bond distance between Ti and O_{24} is 2.109 Å, while the

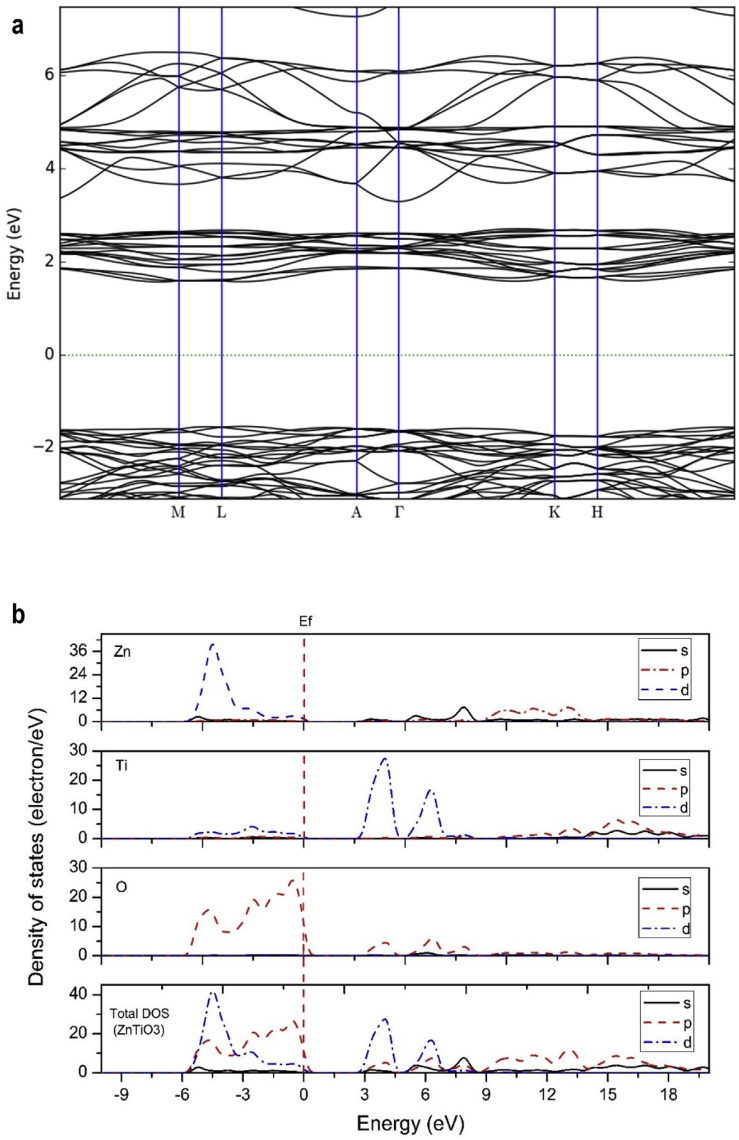

FIGURE 4.22: Electronic properties of $ZnTiO_3$ showing a) Material band structure and b) Partial and total density of state plots where. The Fermi level is represented by the (dashed line) and is set as zero.

distance between Zn and O_{25} is slightly different (2.176 Å). Its surface is protonated with a hydrogen atom that is linked to closer surface oxygen by creating (H-O) bond of 0.972 Å. This is because Ti atoms around O25 stay away from the surface after the optimization, which suggests that the O_{25} atom, in COOH group, could not form an O_{25}-Ti bond instead of O_{25}-Zn. This leads the anchoring group to make a combination with both Zn and Ti atoms. Both interactions between COOH and the surface were illustrated by 2D electronic density representation as shown in Figure 4.24b.

As shown in Figure 4.24a , the adsorption energy (Eads) of N3@$ZnTiO_3$ was calculated to be (-10.5 eV), as reported in Table 4.7. Yang et al. reported that Eads values for

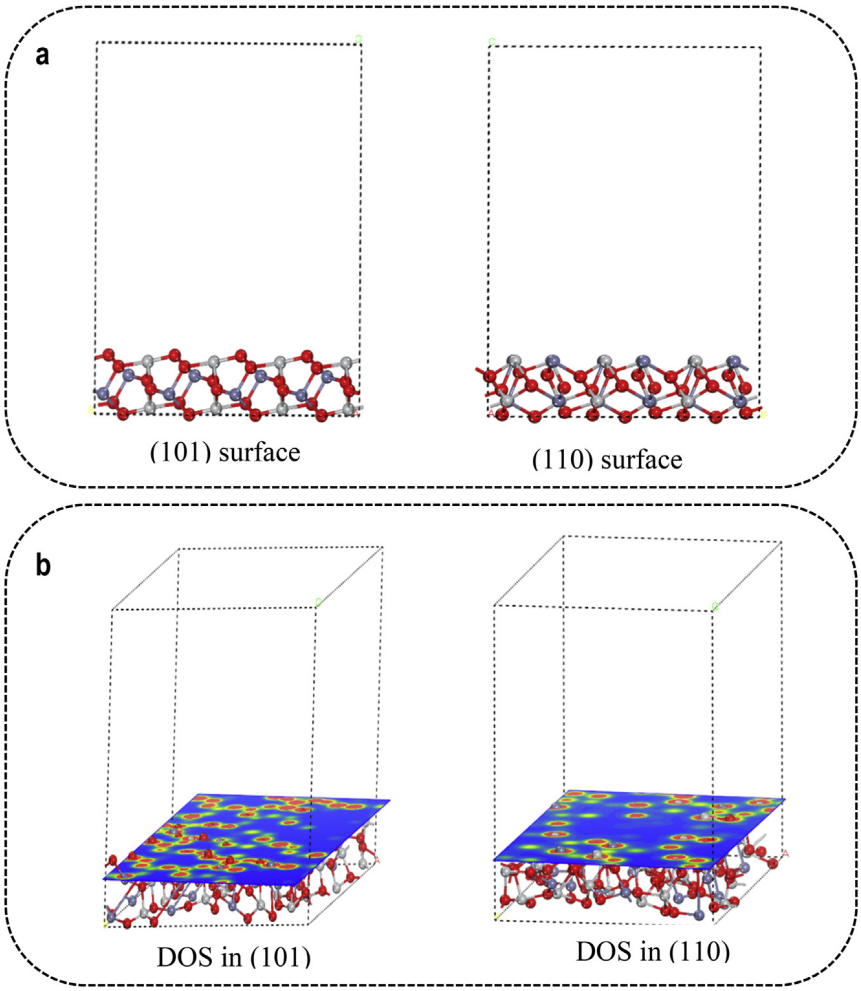

FIGURE 4.23: $ZnTiO_3$ surfaces, showing (a) $ZnTiO_3$ (101) and (110) surfaces before geometry optimization, and (b) the electronic density presentation of (101) and (110) surfaces after optimization. The colors, blue, green, yellow and red represent the electrons location probability of 0 electron, 2 x 10^{-1} electron, 6 x 10^{-1} electron and 1 electron, respectively. (For interpretation of the references to color in this figure legend, the reader is referred to the Web version of this article.)

N3@TiO_2 in (101) and (100) surfaces were (-3.84 eV) and (-6.37 eV), respectively [190], whereas Azpiroz et al. showed that Eads value of N3@ZnO in (101) surface was (-3.88 eV) [189]. The Eads value, observed here for N3@$ZnTiO_3$ in (101) surface, is higher than those for either N3@TiO_2 or N3@ZnO values. This means that the $ZnTiO_3$ perovskite has larger specific surface area than TiO_2 and ZnO. Unlike (101) surface, N3 dye adsorbs on $ZnTiO_3$ (110) surface via the two monodentate ester (ME) mode, without any proton attached on the closer surface oxygen, presumably due to the missing oxygen atoms on the (110) surface as displayed in Figure 4.25.

However, the bond distances between (Ti and O_{24}) and (Ti and O_{22}) atoms are calculated to be 2.26 Å and 2.15 Å, respectively. The calculated adsorption energy (Eads)

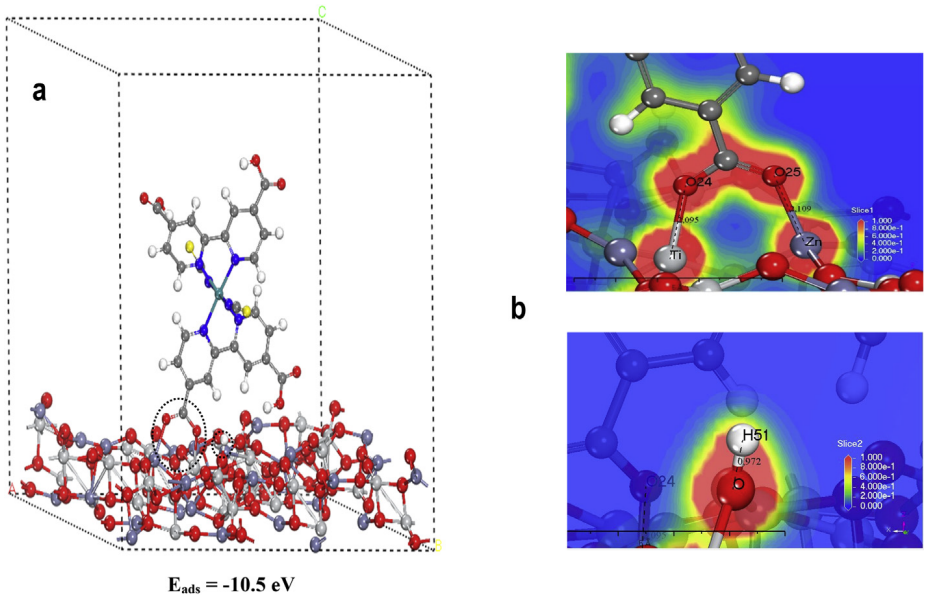

FIGURE 4.24: A schematic for the N3 dye adsorbed onto $ZnTiO_3$ (101) surface, a) Optimization of N3@$ZnTiO_3$ complex, b) calculated distances between Ti-O_{24} and Ti-O_{22}, with 2D representation of electronic density of monodentate ester (ME) anchoring group.

TABLE 4.7: Adsorption energies of N3 dye on different surfaces and solids

Adsorption	Surface used	Eads (eV)	Eads (kcal/mol)	Reference
N3@ZnO	101	-3.88	-89.58	[189]
N3@TiO2	101	-3.84	-88.55	[190]
	100	-6.37	-146.9	[190]
N3@ZnTiO3	101	-10.5	-241,50	
	110	-2.5	-57.65	This work

for N3@$ZnTiO_3$ complex is -2.50 eV (-57.65 kcal/mol). This value is smaller than Eads in (101) surface, due to its lower surface electronic density, which means that several surface metaleoxygen bonds are involved in the adsorption energetic process.

4.5.7 Electron injection and dye regeneration

To investigate the electrochemical properties of DSSCs, the LUMO energy of N3 dye should be higher than the conduction band edge of $ZnTiO_3$ perovskite. In fact, this can ensure electron injection from the excited state of N3 dye to the conduction band of $ZnTiO_3$. The HOMO energy should also be lower than that of (I^-/I_3^-) redox couple to enable dye regeneration process [191]. The driving force of electron injection (Δ

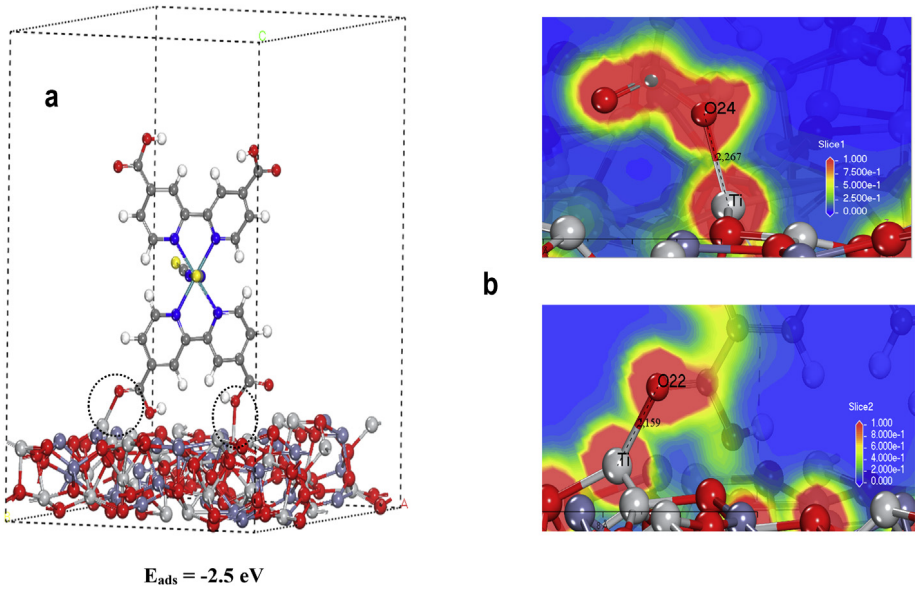

FIGURE 4.25: A schematic for the N3 dye adsorbed onto $ZnTiO_3$ (110) surface, a) Optimization of N3@$ZnTiO_3$ complex, b) calculated distances between Ti-O_{24} and Ti-O_{22}, with 2D representation of electronic density of monodentate ester (ME) anchoring group.

G_{ing}) and dye regeneration (ΔG_{reg}) are illustrated in Table 4.8 by using the following equations [192],[193].

$$\Delta G_{ing} = -[E^{ox}_{Dye^*} - E^{CBE}_{TiO_2}] \tag{4.4}$$

$$E^{ox}_{Dye^*} = [E^{ox}_{Dye} - \lambda^{ICT}_{max}] \tag{4.5}$$

$$\Delta G_{reg} = -[E^{ox}_{I^-/I_3} - E^{ox}_{Dye}] \tag{4.6}$$

TABLE 4.8: Approximated electrochemical parameters of the N3 dye adsorbed on 110 and 101 surfaces of ZnTiO3.

Adsorption	**Surface used**	$\mathbf{E^{ox}_{Dye}}$ **(eV)**	$\mathbf{E^{ox}_{Dye^*}}$**(eV)**	ΔG_{ing} **(eV)**	ΔG_{reg} **(eV)**	**LHE**
	-110	-5.95	-4.24	-0.06	-1.05	0.13
N3@$ZnTiO_3$	-101	-5.76	-4.16	-0.12	-0.86	0.22

where,
E^{ox}_{Dye} is considered as the HOMO energy of the sensitizer based on the Koopmans's theorem [48], λ^{ICT}_{max} is the maximum absorption energy of the dye, $E^{CBE}_{TiO_2}$ is the conduction band edge (CBE) energy of the $ZnTiO_3$ taken as -4.27 eV [194], and $E^{ox}_{I^-/I_3}$ is the redox potential taken as -4.90 eV [195]. The negative ΔG_{ing} value indicates that the electron injection is a spontaneous process. Moreover, the more negative value

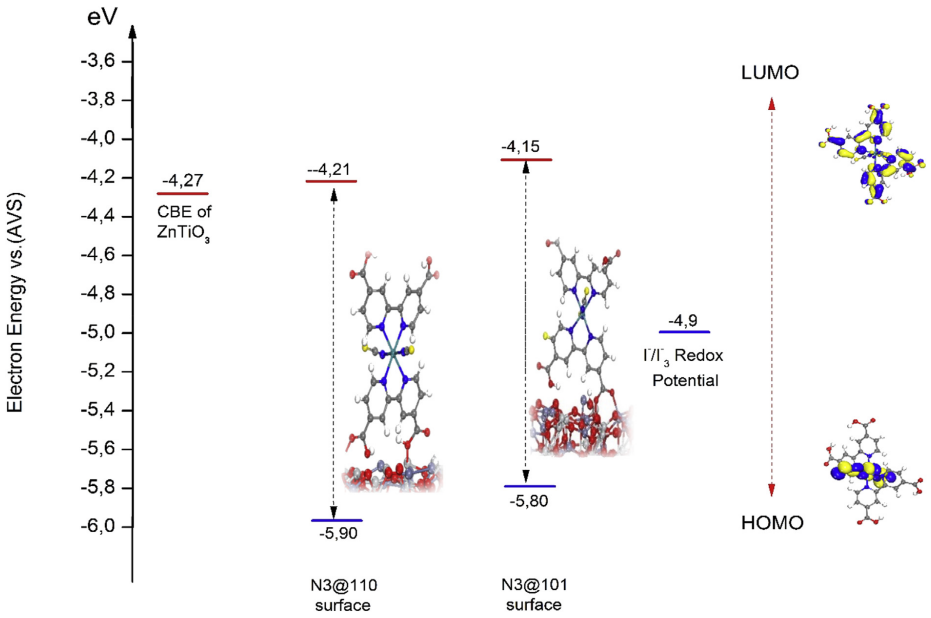

FIGURE 4.26: Schematic energy diagram of Ruthenium dye adsorbed on (110) and (101) surfaces, with respect to $ZnTiO_3$ conduction band edge and I^- / I_3- redox potential.

provides larger driving force leading to higher short circuit photocurrent density (Jsc) value [196],[197]. However, in case of ruthenium dye adsorbed on $ZnTiO_3$ (101) has largest negative ΔG_{inj} value of -0.06 compared to -0.12 in N3/(110) surface. This indicates that, the injection rate (K_{inj}) of N3@$ZnTiO_3$ (101) complex is more feasible than N3@$ZnTiO_3$ (110) complex, leading to a low relaxation rate between the LUMO and HOMO of ruthenium dye. In addition, the dye regeneration value -0.86 in N3/(101) is more negative than -1.05 in N3/(110) surface. This confirms that the regeneration rate (k_{reg}) of N3@$ZnTiO_3$(101) complex is more higher than N3@$ZnTiO_3$ (110) complex, which lowers recombination rate between the conduction band of $ZnTiO_3$ and the ground state (HOMO) of N3 dye. All above results are summarized in Figure 4.26

4.5.8 Conclusion

First principal computational approaches based on Density Functional Theory, have been applied to compute the optical and electronic properties of N3 dye as free and adsorbed on perovskite $ZnTiO_3$. B3LYP hybrid functional and GGA-PBE exchange correlation with TS parameterization for DFT-D correction have been used here. Calculations were performed for N3 dye in its gas phase and ethanol solution for comparison purposes. DFT-D approach is found to be an accurate approximation for electronic structure of zinc titanate, as it yields comparable results to the available experimental data. The adsorption energy (Eads) has been computedconsidering the van der Waals dispersion corrections based on Grimme scheme. Compared to TiO_2 and ZnO, the $ZnTiO_3$ perovskite exhibited larger Eads value. The higher electronic density on (101) surface leads to higher adsorption energy (-241.50 kcal/mol) than in the (110) surface (-57.65 kcal/mol). The N3 adsorption onto $ZnTiO_3$ via bidentate bridging (BB) mode, on (101) surface, is more stable than on the (110) surface. The large surface area feature of the $ZnTiO_3$ photoanode leads to enhanced light harvesting efficiency of the dye. The electron injection efficiency (-0.06) of ruthenium dye attached on (101) surfacewas expected to be higher than in the (110) surface (-0.12). It was mainly attributed to relaxation rate decrease between HOMO and LUMO energy levels of the dye. Furthermore, the decrease of recombination rate between the dye and the semiconductor is expected to increase the power conversion efficiency (PCE) of the DSSC.

4.6 Adsorption of triphenylamine-based dye onto $ZnTiO_3$ (101) surface

Triphenylamine (TPA) derivative dyes exhibit excellent solubility and sound stability with high photoluminescence efficiency due to their conjugation. Such dyes have been used in the fabrication of optoelectronic and electronic devices [198] and are examined in DSSCs [199],[200],[201]. Studies on Triphenylamine-Based Dyes in DSSCs have been reported from experimental[202], [203],[204], and theoretical [200], [205],[206]points of views. TPA dyes are expected to behave as an ideal donors due to their high electron donation and good hole-transportation. Despite their wide spread investigation, as stated above, TPA dyes need further study. For example, effect of the dye substituent of the DSSC efficiency should be further assessed, which means that comparative study between different types of TPA dyes is imperative. For example, TPA-based dyes, shown in Figure 4.27, with different substituents having different linkage composition and length showed different power conversion efficiency values. While TPA-1 showed conversion efficiency value of 2.5% with TiO_2, TPA-2 and TPA-3 showed higher values of 5.2% and 7.3%, respectively [207]. TPA-4 dye showed even higher conversion efficiency of 9.1% [208].

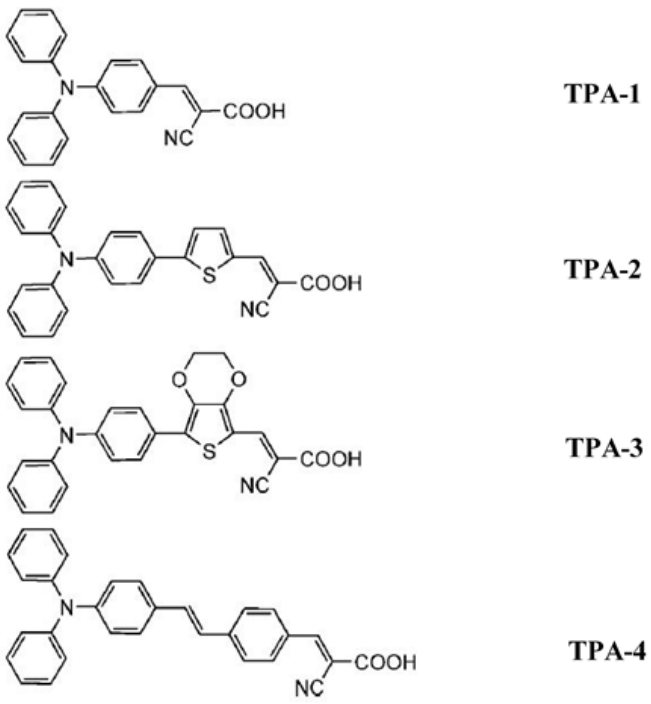

FIGURE 4.27: Molecular structures of different Triphenylamine-based dyes studied.

This work aims at comparatively studying characteristics of such dyes. Rationalizing the conversion efficiency variations for these dyes in earlier reported TiO_2 DSSC systems, based on their characteristics, is described here. Anchoring the dyes to $ZnTiO_3$ perovskite semiconductor electrodes, for future DSSC study is another major goal of this work. The perovskite $ZnTiO_3$ is chosen here due to its special features, most importantly is its high electron mobility in the range (150 - 400 cm^2/Vs) that is higher than either TiO_2 or ZnO systems [209].Figure 1 shows that these dyes differ in substituent length and chemical composition. Effects of such differences on properties of these dyes are investigated here. The electronic properties and electronic absorption spectra are simulated for each dye in its free form and $ZnTiO_3$ adsorbed form. The energy level diagrams and electron density values are also studied on each dye in its free and adsorbed forms. The geometry of adsorption onto the $ZnTiO_3$ surface (101) is also comparatively studied to find the dye with best features. All such parameters are studied here in cross comparative manner between different dyes, for the first time, so as to find the one that may best fit for $ZnTiO_3$ DSSCs. Comparison with earlier published theoretical and experimental results is also presented.

4.6.1 Materials and methods

The geometry optimization for each Triphenylamine-based dye (TPA), in free and adsorbed forms, was fully performed by density functional theory (DFT), by using the hybrid B3LYP-DNP functional. The DNP (including polarization d-function), which is similar to the Gaussian09 6-31G (d, p) basis set, and has higher accuracy than other available basis sets, was selected as a basis set here. For the electronic structure, single-point calculations were performed using the hybrid B3LYP functional, with the same basis set. The dye electronic absorption spectra were calculated using time-dependent density functional theory (TD-DFT). For the geometry optimization and optical properties, the convergence tolerance of energy was 1.0 $\times 10^{-6}$ Ha, and the maximum force was considered as 0.0004 Ha/Åwith maximum displacement 0.0005Å. To determine the relative stability of dye molecule adsorption onto the (101) surface of a given $(ZnTiO_3)_8$ perovskite cluster (involving 8 Zn atoms, 8 Ti atoms and 24 O atoms), full geometry optimization was conducted using the DMol3 code. The DFT-D approach was applied to treat the weak (Van der Waals, vdW) interactions between TPA dye carboxylic groups (COOH) and $ZnTiO_3$ surfaces.To check the geometrical parameters and adsorption energy of (TPA@$ZnTiO_3$) complex systems the periodic DFT geometry optimizations have been performed within the generalized gradient approximation (GGA) using the PBE exchange–correlation functional. All calculations were performed with the BIOVIA MATERIALS STUDIO package.

4.6.2 Structure of Triphenylamine-based dyes

The dye molecular structure has important role in DSSCs. Optimized geometrical structures of Triphenylamine-based sensitizers were earlier reported [210]. The structures used here are based on the earlier reported ones shown in Figure 4.27. The four TPA dyes studied have different substituent lengths with different linkages. As described in Section 4.6 above, different linkages caused changes in dye conversion efficiency in TiO_2 DSSCs. Figure 4.27 shows that all dyes involve π-conjugated systems. The optimized 3-dimensional structures are illustrated in Figure 4.28.

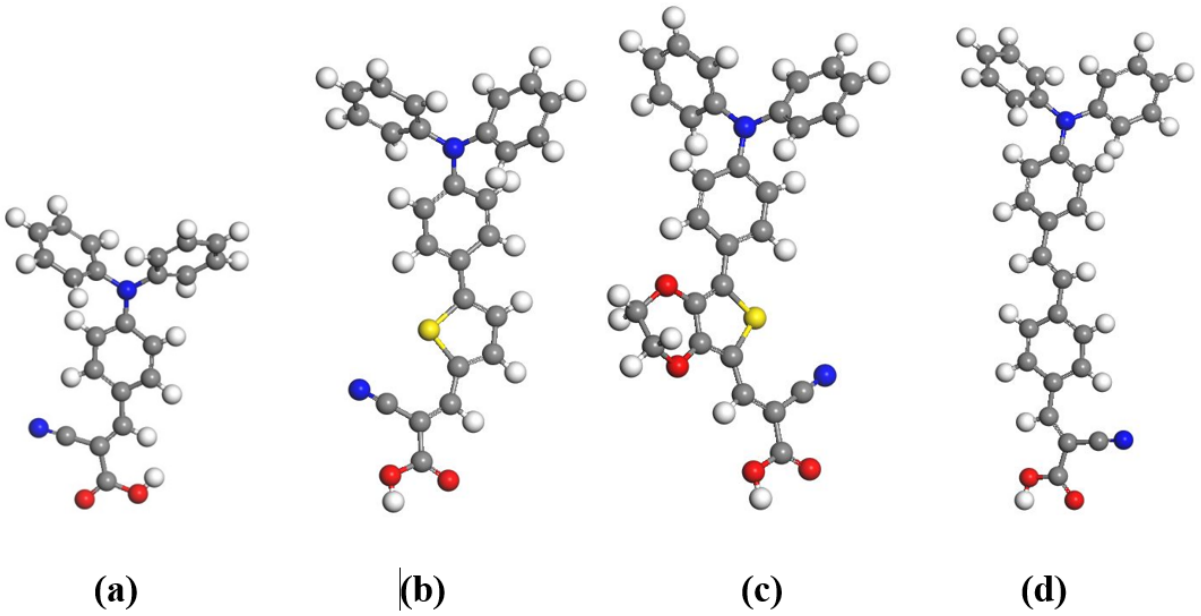

FIGURE 4.28: Optimized 3-dimensional structures for the dyes (a) TPA-1 without any linkage, (b) TPA-2 with thiophene linkage, (c) TPA-3 with bridge (EDOT) linkage, and(d) TPA-4 with phenylenevinylene linkage. All structures are made based on density DFT/B3LYP hybrid functional.

4.6.3 Electronic absorption spectra

One main feature for a sensitizer in DSSCs is its ability to absorb in the visible spectral region (400 to 800nm) and the near infrared (NIR) region. In this work, electronic absorption spectra are investigated using time-dependent density functional theory (TD-DFT) (Figure 4.29) in ethanol solvent for all four dyes in their free form and after adsorption onto $ZnTiO_3$ perovskite. The calculated λ_{max} value is an important criterion for suitability of these metal-free organic systems to consider as sensitizers in a DSSC. The electronic absorption spectra of TPA-dyes indicate a systematic peak position shifting in both forms (free and adsorbed). The spectrum of the TPA-4 dye has a high absorption peak between 440 nm and 500 nm, compared to other TPA-dyes. The TPA-4

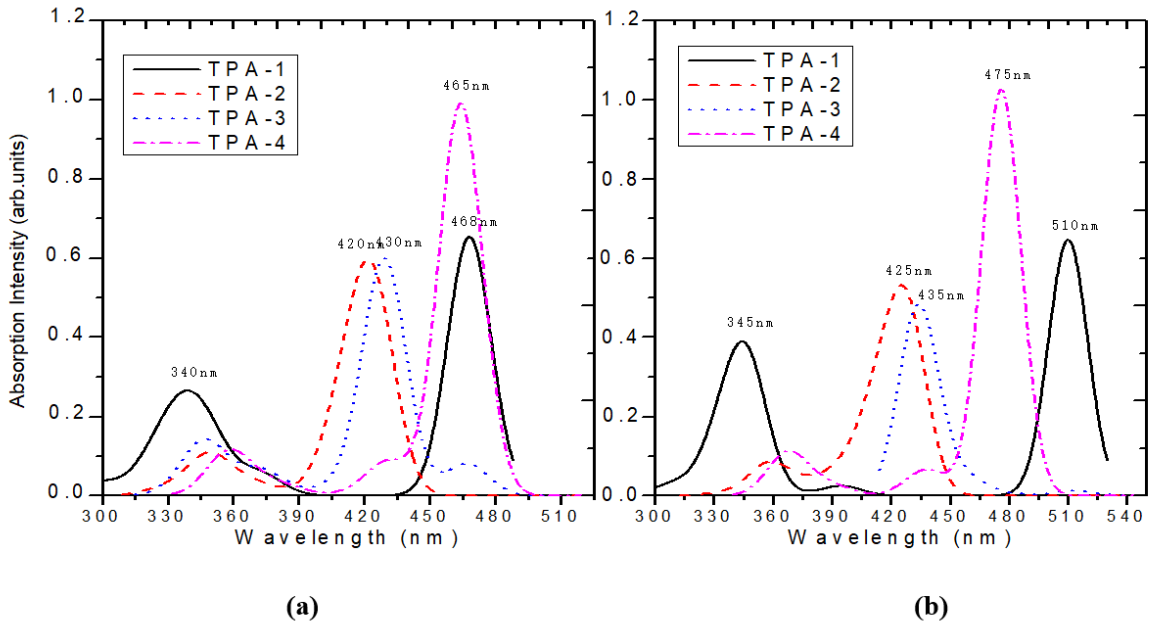

FIGURE 4.29: Simulated electronic absorption spectra for different TPA dyes (a)in their free forms and(b)in their $ZnTiO_3$ adsorbed forms. Simulation was performed by First-principles (TD-DFT) calculation in ethanol solvent.

peaks are at 465 nm(for free form) and at 475 nm(adsorbed form). For TPA-1 dye, experimental results showed an absorption maximum at 386 nm in ethanol solution[211] compared to 340 nm and 468 nm values observed here. Other earlier reports showed similar values of 386 nm [212] or 400 nm [213] Similarly, the TPA-2 shows a value of 420 nm in the free form and 425 nm in the adsorbed form. Jinxia et al.reported a value of 429 nm [214] while Wei-Hsin et al. experimentally reported a value of 410 nm [215]. The absorption peaks of TPA-3 dye in the free and adsorbed forms are 430 nm and 435 nm, respectively. The reported experimental value is 426nm [215]. The λ_{max} value corresponds to the oscillator strength (*f*, which is another feature that affects the solar cell power conversion efficiency (PCE). The Light Harvesting Efficiency (LHE) is related to oscillator strength at its λmax [216]. The free dyes can thus be ordered in terms of their matching with the LHE as: TPA-4>TPA- 1>TPA-2>TPA-3.

4.6.4 Energy level alignment

To enhance the electron injection into the semiconductor conduction band (CB), and dye regeneration processes, the DFT calculations can show energy levels of the dye, the $ZnTiO_3$ semiconductor and the liquid redox couple. The calculated energy levels for the ground and the excited states of TPA dyes, together with the conduction band edge for $ZnTiO_3$ and the redox couple I^-/I_3^- are illustrated in Figure 4.30

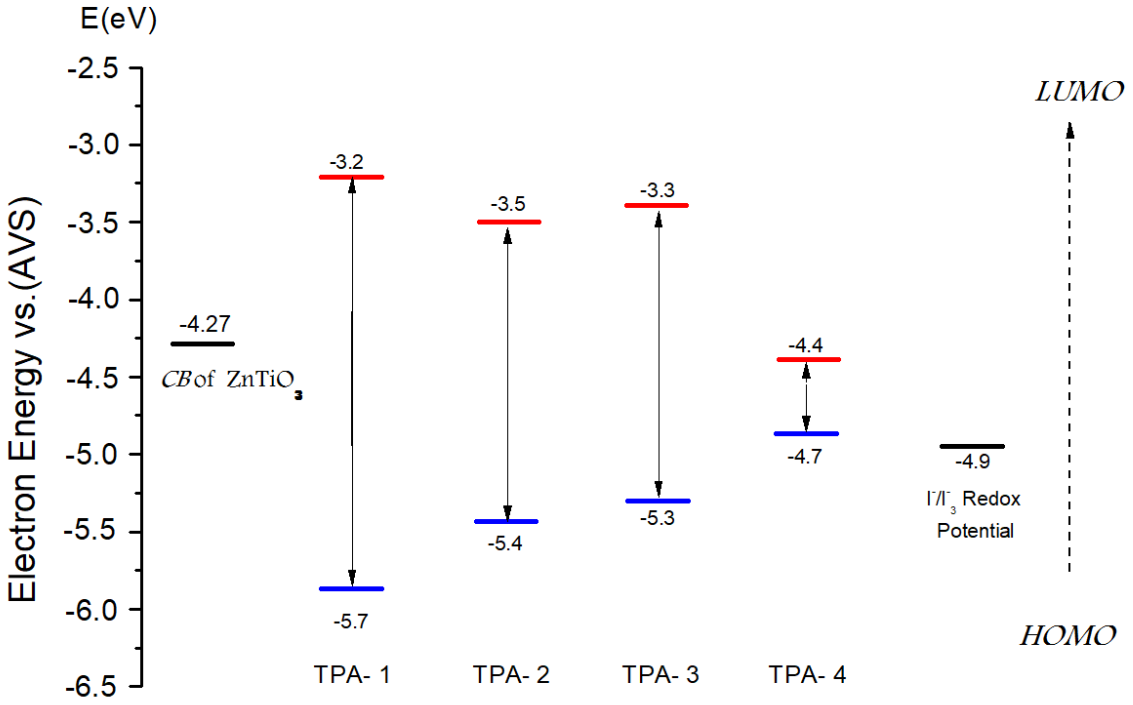

FIGURE 4.30: Energy diagram presenting the ground state (blue) and the excited state (red) energies calculated by TD-DFT (B3LYP) methods for TPA-dyes.

For TPA-dyes, the LUMO energy levels should be higher than the conduction band edge (CBE) of $ZnTiO_3$ perovskite. This allows the injection of the photo-excited electrons into the conduction band (CB) of $ZnTiO_3$. The TPA- dye HOMO levels should also bellow than the energy level for I^-/I_3^- redox couple, to regenerate the positively charged dye ions resulting after electron injection into the conduction band of the semiconductor. The driving force for the electron injection (from dye into semiconductor (CB) is the difference between the excited state energy level of the dye and the semiconductor CBE. The spontaneity of electron injection can be expressed in terms of Gibbs free energy, as shown in Equations (4.4),(4.5),(4.6).

where E^{ox}_{Dye} is the HOMO energy of the dye based on the Koopmans's theorem; λ^{ICT}_{max} is the maximum absorption energy of the dye and $E^{CBE}_{TiO_2}$ is the $ZnTiO_3$ CBE energy taken as -4.27 eV [212], and the redox potential $E^{CBE}_{TiO_2}$ is taken as -4.9 eV [213]. The negative ΔG_{inj} indicates spontaneous electron injection process. The higher negative value means higher driving force leading to larger short circuit photo-current density (Jsc) . Table 4.9 summarizes calculated ΔG_{inj}, ΔG_{reg} and LHE values for different TPA dye systems.

Table 4.9 shows that the spontaneity to regenerate different TPA-dyes gradually increases with decreasing the LHE value of the dye. This is due to different substituents

TABLE 4.9: Approximated electrochemical parameters of different TPA-dyes calculated by B3LYP-DNP functional.

	E^{ox}_{Dye} (eV)	$E^{ox}_{Dye^*}$ (eV)	ΔG_{inj} (eV)	ΔG_{reg} (eV)	LHE
TPA-1	-5.77	-3.29	-0.98	-0.87	0.78
TPA-2	-5.42	-3.53	-0.74	-0.52	0.72
TPA-3	-5.35	-3.36	-0.91	-0.45	0.65
TPA-4	-4.72	-4.47	0.2	0.18	0.9

in the dye molecule linkage. The TPA-4 dye has much lower negative regeneration (0.18)and injection (0.20) free energy values than other TPA-dyes. This inhibits the electron injection process from the dye into the $ZnTiO_3$ CB and the dye regeneration regeneration. On the other hand, the TPA-3 dye more spontaneous electron injection and dye regeneration processes, and subsequently the (TPA-3@$ZnTiO_3$@ I^-/I_3^-) system should have higher photo-electrochemical (PEC) performance. Add to that the higher adsorption energy for the TPA-3@$ZnTiO_3$ system, as described in Section 4.6.5 below. The difference between the properties of different TPA-based dyes is due to the linkage group present in the substituent groups as shown in Figures 4.27 and 4.28. With different linkages, the conjugation along the dye chain varies and affects electron injection from the dye sensitizer to the semiconductor CB. With higher injection rate, like in TPA-3 dye, higher JSC values are expected [214].

4.6.5 Dye adsorption

The way the dye molecules are anchored to the photoanode of DSSC significantly affects the dye adsorption energy. Therefore, calculating the value of adsorption energy gives insight on the adherence strength and way of bonding between the dye and the semiconductor surface. With higher adsorption energy, electron injection into the semiconductor CB is more facilitated. This consequently enhances the PCE value for the DSSC. TPA-based dyes have carboxyl groups at the end of their linkages. The carboxyl groups may adsorb in different modes onto the anatase $(ZnTiO_3)_{38}$ cluster with higher exposure for the (101) surfaces. Adsorption may occur via a monodentate or a bidentate mode. The latter mode has more stable adsorption with higher adsorption energy [201] .

To understand the adsorption behavior of Triphenylamine-based dyes onto a $ZnTiO_3$ perovskite, a $(ZnTiO_3)_8$ cluster is constructed with (101) surface exposed (Figure 4.31). To determine the stability of TPA-dye@$ZnTiO_3$ complexes, the adsorption energy of

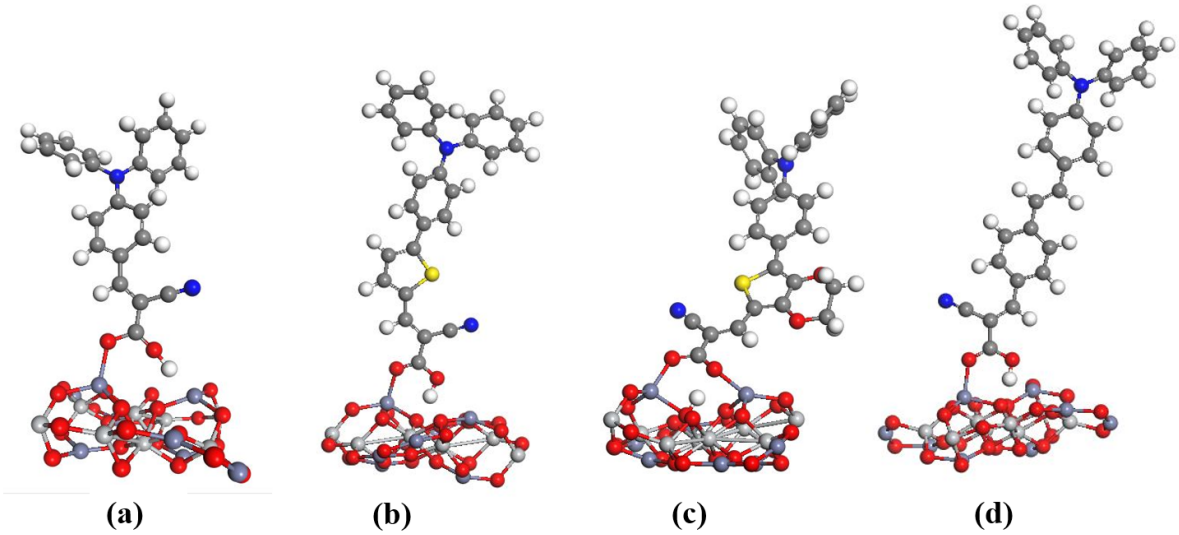

FIGURE 4.31: Optimized structures of the TPA-based dyes@$ZnTiO_3$ complexes systems: (a) TPA-1@$ZnTiO_3$;(b) TPA-2@$ZnTiO_3$; ;(c) TPA-3@$ZnTiO_3$; (d) TPA-4@$ZnTiO_3$, at the DFT/GGA/PBE level.

dye/$ZnTiO_3$ structure is expressed in Equation 4.3 : Values of adsorption energies for different TPA dyes are summarized in Table 4.10

TABLE 4.10: Adsorption energy values of TPA@ $ZnTiO_3$ (101) systems in (eV) and kJ/mol units

Adsorption	Unit	TPA-1	TPA-2	TPA-3	TPA-4
E_{ads}	(eV)	-1.41	-1.63	-5.82	-2.37
	(kJ/mol)	-136.39	-157.47	-561.33	-228.19

TPA-dyes have different adsorption energy values. Table 4.10 shows that the adsorption energy for different dyes follow the order: TPA-3>TPA-4>TPA-2>TPA-1. The simulation results show that TPA-3 dye exhibits highest adsorption energy of -561.33 kJ/mol (-5.82 eV)compared to TPA-4, TPA-2 and TPA-1 dyes. The results show TPA-3 dye may bond to the $ZnTiO_3$ (101) surface via a bidentate mode, as described in Figure 4.31. Other dyes, with lower adsorption energy, can bond via a monodentate mode only. The difference is rationalized by the structure of TPA-3 which involves two oxygen atoms in the ethylenedioxythiophene linkage. The two oxygen atoms, with high electronegativity, may withdraw electronic charge from the carboxyl group and increase the acidity of the H atom. Therefore, the loss of the H atom becomes more possible which allows bidentate bonding with $ZnTiO_3$ surface.
With superior adsorption energy to the $ZnTiO_3$ surface (101), TPA-3 has better adherence and stronger bonding with the semiconductor. Such strong bonding facilitates

the electronic injection between the excited dye molecules and the $ZnTiO_3$CB. Consequently, the DSSC performance should be preferably enhanced for TPA-3@$ZnTiO_3$ DSSCs. This is contrary to the TiO_2 based DSSCs, where TPA-4 showed highest conversion efficiency [208], compared to other studied dyes. Moreover, Table 4.10 results rationalize Table 4.9 findings. With stronger adsorption and adherence in TPA-3@$ZnTiO_3$ system, the electronic injection should be more spontaneous than in other dyes. In fact all simulation results acquired here are in congruence with one another, and all suggest that the TPA-3 is superior to other counterparts. Collectively, the results come out with a recommendation to preferably use the TPA-3 dye in $ZnTiO_3$ based DSSC systems. The results thus open the door to do more experimental and theoretical studies on dye TPA3@$ZnTiO_3$ DSSC systems, in terms of photoelectrochemical (PEC) characteristics. Taking into account the present findings, all PEC characteristics can be studied in the future, including short circuit photo-current density (Jsc), open circuit potential (Voc), fill factor (FF) and dye stability at the Dye@$ZnTiO_3$(101) surface. Comparison between different TPA-based dyes is recommended. Comparison between $ZnTiO_3$ on one hand and TiO_2 and ZnO systems on the other hand, is also worth to study both theoretically and experimentally.

4.6.6 Conclusion

Four triphenylamine-based dyes (TPA-1, TPA-2, TPA-3 and TPA-4), reported earlier in TiO_2 based dye sensitized solar cells, have been investigated here as sensitizers for $ZnTiO_3$ based cells. Contrary to earlier reports, where TPA-4 showed higher efficiency in TiO_2 systems, the TPA-3 is anticipated to show highest power conversion efficiency (PCE) among the series in case of $ZnTiO_3$ cells. This is based on simulation study. All dyes have been investigated here from different aspects. Density functional theory (DFT), time-dependent density functional theory (TD-DFT), and hybrid B3LYP-DNP functional were used. The BIOVIA MATERIALS STUDIO package was used in the calculations. Based on its special structure, the TPA-3 dye shows superiority, over all other three counterparts, in terms of studied characteristics: electronic absorption spectra, light harvesting energy, energy level alignment with the semiconductor band edge positions, charge transfer between excited dye and semiconductor conduction band, dye regeneration, and adsorption energy onto $ZnTiO_3$ surface (101). All results suggest that the TPA-3 is superior to other dyes in terms of bonding to the semiconductor surface, spontaneity of charge transfer at the interface, and future photoelectrochemical performance.

Conclusions and Perspectives

As seen in the literature, although there are still drawbacks that ETMs materials could limit the enhancement of the solar cells performance. Although these drawbacks can easily be overcome by various methods, such as doping ETMs, or surface modification by coating them with thin surface layers, or using Ternary Metal Oxides semiconductors with a bandgap similar to that of TiO_2. However, perovskite materials or Ternary metal oxides with a chemical formula of (ABX_3) could be attractive candidates in the field of efficient third-generation photovoltaic cells due to their electrical properties and band structure can be easily modified by alternating the composition.

Computationally, structural, Electronic and Optical properties of $ZnTiO_3$ perovskite has been studied using First principal computational approache based on Density Functional Theory (DFT), $ZnTiO_3$ experiences similar physical properties to ZnO and TiO_2 metal oxides in band alignment, band-gap and higher electron mobility, the surface area of $ZnTiO_3$ is greater then in ZnO and TiO_2, leads to adsorb more dye molecules on the surface and promoted to be a good candidate for dye sensitized solar cell application.

Our perspective in next researches is to proceed with validating our computational work by manufacturing Perovskite $ZnTiO_3$ thin films for photoanode purpose in dye sensitized solar cell, $ZnTiO_3$ were actually prepared using two chemicals approaches , sol–gel method using Titanyl acetylacetonate, Titanium isopropoxide, Znic nitrate and Znic nitrate as precursor materials and 2-methoxy ethanol as solvent. The resultant sol ($ZnTiO_3$) was then filtered using Wattman filter paper and kept it in an air tight bottle. A few drops of zinc titanate sol were placed on FTO glasses spin coated with different spinning speeds and times of (1000, 2000 and 3000 rpm) and (20s, 30s, 50s) respectively. The films were later dried for 30 min. The $ZnTiO_3$ films were annealed at 450°C for 4 h in air. In addition, a preparation technique of $ZnTiO_3$ paste from commercially-available powder has been disclosed in order to fabricate the nanocrystalline layers by Doctor blade coating method without cracking and peeling-off thin films on FTO substrate. Zinc titanate films were soaked in a dye solution (0.5mM purified N535 dye in absolute ethanol) at room temperatures for 60 min. After the dye adsorption process, the films were thoroughly rinsed with a mild stream of absolute ethanol to remove the

physically adsorbed dye molecules. Sandwich-type DSSCs were then assembled using the dye-adsorbed ZTO film and a platinized FTO substrate with a hot-melt film (60μ, Surlyn) between them. Finally, an iodide-based liquid electrolyte was infiltrated into the cell through a hole from the counter electrode side. The active area of the dye-coated ZTO film was 1cm^2.

However, the results of our experiments were not enough accurate to support our computational study, that is requires more knowledge and experience in chemistry engineering and become more familiar with utilizing lab equipment and machines such us X-ray powder diffractometer (XRD) for crystal structure, a field-emission scanning electronmicroscope (SEM) for the morphological properties of the films and UV-vis spectrometer to preform optical properties of the samples, end up with solar simulator to examinate the photo-current and voltage characteristics of the cell.
Finally, $ZnTiO_3$ perovskite has been studied for the first time as a photoanode in dye sensitized solar cell application, according to its higher discovered features than TiO_2 and ZnO oxide materials, we promote that Zinc titanate would become further engaging to scientists and promised for use as an electron transport material in DSSC and PSC, moreover, increase the power conversion efficiency (PCE) of the cell in the future.

Bibliography

[1] Y. Chergui, N. Nehaoua, and D. Mekki, "Comparative study of dye-sensitized solar cell based on ZnO and TiO_2 nanostructures," *Solar Cells-Dye-Sensitized Devices*, 2011.

[2] Y. Dkhissi, S. Meyer, D. Chen, H. C. Weerasinghe, L. Spiccia, Y.-B. Cheng, and R. A. Caruso, "Stability comparison of perovskite solar cells based on zinc oxide and titania on polymer substrates," *ChemSusChem*, vol. 9, no. 7, pp. 687–695, 2016.

[3] B. Srinivas, S. Balaji, M. Nagendra Babu, and Y. Reddy, "Review on present and advance materials for solar cells," *International Journal of Engineering Research-Online*, vol. 3, pp. 178–182, 2015.

[4] M. Bertolli, "Solar cell materials. course: Solid state ii," *Department of Physics, University of Tennessee*, 2008.

[5] P. Jayakumar, "Resource solar energy assessment handbook," 2009.

[6] A. Kołodziej, "Staebler-wronski effect in amorphous silicon and its alloys," *Opto-electronics review*, vol. 12, no. 1, pp. 21–32, 2004.

[7] A. K. Pal and H. C. Potter, "Advances in solar energy: Solar cells and their applications," in *Advances in Solar Energy Research*, pp. 75–127, Springer, 2019.

[8] K. Chopra, P. Paulson, and V. Dutta, "Thin-film solar cells: an overview," *Progress in Photovoltaics: Research and applications*, vol. 12, no. 2-3, pp. 69–92, 2004.

[9] M. Imamzai, M. Aghaei, Y. H. M. Thayoob, and M. Forouzanfar, "A review on comparison between traditional silicon solar cells and thin-film cdte solar cells," in *Proceedings of National Graduate Conference (Nat-Grad*, pp. 1–5, 2012.

[10] S. Sharma, K. K. Jain, A. Sharma, *et al.*, "Solar cells: in research and applications—a review," *Materials Sciences and Applications*, vol. 6, no. 12, p. 1145, 2015.

[11] M. A. Maehlum, "Best thin film solar panels–amorphous, cadmium telluride or cigs," *Retrieve from: http://energyinformative. org/best-thin-film-solar-panels-amorphous-cadmium-telluridecigs*, 2015.

[12] D. Y. Goswami and F. Kreith, *Handbook of energy efficiency and renewable energy*. Crc Press, 2007.

[13] A. Luque and S. Hegedus, *Handbook of photovoltaic science and engineering*. John Wiley & Sons, 2011.

[14] W. A. Badawy, "A review on solar cells from si-single crystals to porous materials and quantum dots," *Journal of advanced research*, vol. 6, no. 2, pp. 123–132, 2015.

[15] A. M. Bagher, M. M. A. Vahid, and M. Mohsen, "Types of solar cells and application," *American Journal of optics and Photonics*, vol. 3, no. 5, pp. 94–113.

[16] F. Andorka, "Cigs solar cells simplified. solar power world," *Archived from the original on*, vol. 16, 2014.

[17] T. M. Razykov, C. S. Ferekides, D. Morel, E. Stefanakos, H. S. Ullal, and H. M. Upadhyaya, "Solar photovoltaic electricity: Current status and future prospects," *Solar energy*, vol. 85, no. 8, pp. 1580–1608, 2011.

[18] P. Choubey, A. Oudhia, and R. Dewangan, "A review: Solar cell current scenario and future trends," *Recent Research in Science and Technology*, vol. 4, no. 8, 2012.

[19] M. Ye, X. Wen, M. Wang, J. Iocozzia, N. Zhang, C. Lin, and Z. Lin, "Recent advances in dye-sensitized solar cells: from photoanodes, sensitizers and electrolytes to counter electrodes," *Materials Today*, vol. 18, no. 3, pp. 155–162, 2015.

[20] B. Ganesh, Y. V. Supriya, and G. Vaddeswaram, "Recent advancements and techniques in manufacture of solar cells: organic solar cells," *International Journal of Electronics and Computer Science Engineering*, vol. 2, no. 2, pp. 565–573, 2013.

[21] A. C. Mayer, S. R. Scully, B. E. Hardin, M. W. Rowell, and M. D. McGehee, "Polymer-based solar cells," *Materials today*, vol. 10, no. 11, pp. 28–33, 2007.

[22] C. J. Brabec, S. E. Shaheen, C. Winder, N. S. Sariciftci, and P. Denk, "Effect of lif/metal electrodes on the performance of plastic solar cells," *Applied physics letters*, vol. 80, no. 7, pp. 1288–1290, 2002.

[23] K. P. Fritz, S. Guenes, J. Luther, S. Kumar, N. S. Sariciftci, and G. D. Scholes, "Iv–vi nanocrystal–polymer solar cells," *Journal of Photochemistry and Photobiology A: Chemistry*, vol. 195, no. 1, pp. 39–46, 2008.

[24] B. Li, L. Wang, B. Kang, P. Wang, and Y. Qiu, "Review of recent progress in solid-state dye-sensitized solar cells," *Solar energy materials and solar cells*, vol. 90, no. 5, pp. 549–573, 2006.

[25] S. Suhaimi, M. M. Shahimin, Z. Alahmed, J. Chyskỳ, and A. Reshak, "Materials for enhanced dye-sensitized solar cell performance: Electrochemical application," *Int. J. Electrochem. Sci*, vol. 10, no. 4, pp. 2859–2871, 2015.

[26] M. Mitchell, "New nanoparticles bring cheaper, lighter solar cells outdoors," *Rdmag. com. Retrieved*, pp. 08–24, 2014.

[27] N.-G. Park, "Perovskite solar cells: an emerging photovoltaic technology," *Materials today*, vol. 18, no. 2, pp. 65–72, 2015.

[28] J. Huang and Y. Yuan, "World scientific handbook of organic optoelectronic devices volume 1: Perovskite electronics,"

[29] M. Grätzel, "Solar water splitting cells," *Nature*, vol. 414, pp. 338–344, 2001.

[30] T. Markvart, A. McEvoy, and L. Castaner, *Practical handbook of photovoltaics: fundamentals and applications*. Elsevier, 2003.

[31] H. Häberlin, *Photovoltaics: system design and practice*. John Wiley & Sons, 2012.

[32] S. Singh and B. Basak, "Power management of non-conventional energy sources connected to local grid," in *International Conference on Modelling and Simulation*, pp. 255–267, Springer, 2017.

[33] C. Solanki and G. Beaucarne, "Advanced solar cell concepts," *Energy for Sustainable Development*, vol. 11, no. 3, pp. 17–23, 2007.

[34] M. A. Green, E. D. Dunlop, J. Hohl-Ebinger, M. Yoshita, N. Kopidakis, and X. Hao, "Solar cell efficiency tables (version 56)," *Progress in Photovoltaics: Research and Applications*, vol. 28, no. 7, pp. 629–638, 2020.

[35] H. Tributsch, "Reaction of excited chlorophyll molecules at electrodes and in photosynthesis," *Photochemistry and Photobiology*, vol. 16, no. 4, pp. 261–269, 1972.

[36] N. Rawal, A. Vaishaly, H. Sharma, and B. B. Mathew, "Dye sensitized solar cells: the emerging technology," *Energy and Power Engineering Science EPES*, vol. 2, no. 2, pp. 46–52, 2015.

[37] S. Iijima, "Helical microtubules of graphitic carbon," *nature*, vol. 354, no. 6348, pp. 56–58, 1991.

[38] B. Gregg, "a.; pichot, f.; ferrere, s.; fields, cl interfacial recombination processes in dye-sensitized solar cells and methods to passivate the interfaces," *J. Phys. Chem. B*, vol. 105, no. 7, pp. 1422–1429, 2001.

[39] A. Mehmood, F. A. Shaikh, and A. Waqas, "Modeling of the solar photovoltaic systems to fulfill the energy demand of the domestic sector of pakistan using retscreen software," in *2014 International Conference and Utility Exhibition on Green Energy for Sustainable Development (ICUE)*, pp. 1–7, IEEE, 2014.

[40] S. Ngamsinlapasathian, T. Sreethawong, Y. Suzuki, and S. Yoshikawa, "Effect of substrate on dye-sensitized solar cell performance using nanocrystalline titania," in *Electron Transfer in Nanomaterials: Proceedings of the International Symposium*, vol. 2004, p. 126, The Electrochemical Society, 2006.

[41] J. Shi, J. Liang, S. Peng, W. Xu, J. Pei, and J. Chen, "Synthesis, characterization and electrochemical properties of a compact titanium dioxide layer," *Solid state sciences*, vol. 11, no. 2, pp. 433–438, 2009.

[42] H. Yu, S. Zhang, H. Zhao, G. Will, and P. Liu, "An efficient and low-cost TiO_2 compact layer for performance improvement of dye-sensitized solar cells," *Electrochimica Acta*, vol. 54, no. 4, pp. 1319–1324, 2009.

[43] H. Choi, C. Nahm, J. Kim, J. Moon, S. Nam, D.-R. Jung, and B. Park, "The effect of $TiCl_4$ -treated TiO_2 compact layer on the performance of dye-sensitized solar cell," *Current Applied Physics*, vol. 12, no. 3, pp. 737–741, 2012.

[44] K. Kalyanasundaram, *Dye-sensitized solar cells*. CRC press, 2010.

[45] D. Chen, F. Huang, Y.-B. Cheng, and R. A. Caruso, "Mesoporous anatase TiO_2 beads with high surface areas and controllable pore sizes: a superior candidate for high-performance dye-sensitized solar cells," *Advanced Materials*, vol. 21, no. 21, pp. 2206–2210, 2009.

[46] N. Dhere, "Sol. energy mater," *Sol. Cells https://doi. org/10.1016/j. solmat*, vol. 3, no. 91, p. 1376, 2007.

[47] L. Giribabu, R. K. Kanaparthi, and V. Velkannan, "Molecular engineering of sensitizers for dye-sensitized solar cell applications," *The Chemical Record*, vol. 12, no. 3, pp. 306–328, 2012.

[48] A. Mishra, M. K. Fischer, and P. Bäuerle, "Metal-free organic dyes for dye-sensitized solar cells: From structure: Property relationships to design rules," *Angewandte Chemie International Edition*, vol. 48, no. 14, pp. 2474–2499, 2009.

[49] N. A. Ludin, A. A.-A. Mahmoud, A. B. Mohamad, A. A. H. Kadhum, K. Sopian, and N. S. A. Karim, "Review on the development of natural dye photosensitizer for dye-sensitized solar cells," *Renewable and Sustainable Energy Reviews*, vol. 31, pp. 386–396, 2014.

[50] S. Rühle, "Tabulated values of the shockley–queisser limit for single junction solar cells," *Solar Energy*, vol. 130, pp. 139–147, 2016.

[51] Z.-S. Wang, K. Sayama, and H. Sugihara, "Efficient eosin y dye-sensitized solar cell containing $Br^-/Br3^-$ electrolyte," *The Journal of Physical Chemistry B*, vol. 109, no. 47, pp. 22449–22455, 2005.

[52] Z.-S. Wang, K. Sayama, and H. Sugihara, "Efficient eosin y dye-sensitized solar cell containing $Br^-/Br3^-$ electrolyte," *The Journal of Physical Chemistry B*, vol. 109, no. 47, pp. 22449–22455, 2005.

[53] G. Oskam, B. V. Bergeron, G. J. Meyer, and P. C. Searson, "Pseudohalogens for dye-sensitized TiO_2 photoelectrochemical cells," *The Journal of Physical Chemistry B*, vol. 105, no. 29, pp. 6867–6873, 2001.

[54] S. A. Sapp, C. M. Elliott, C. Contado, S. Caramori, and C. A. Bignozzi, "Substituted polypyridine complexes of cobalt (ii/iii) as efficient electron-transfer mediators in dye-sensitized solar cells," *Journal of the American Chemical Society*, vol. 124, no. 37, pp. 11215–11222, 2002.

[55] S. A. Sapp, C. M. Elliott, C. Contado, S. Caramori, and C. A. Bignozzi, "Substituted polypyridine complexes of cobalt (ii/iii) as efficient electron-transfer mediators in dye-sensitized solar cells," *Journal of the American Chemical Society*, vol. 124, no. 37, pp. 11215–11222, 2002.

[56] J. Wu, Z. Lan, S. Hao, P. Li, J. Lin, M. Huang, L. Fang, and Y. Huang, "Progress on the electrolytes for dsscs," *Pure Appl. Chem*, vol. 80, no. 11, pp. 2241–2258, 2008.

[57] J. Zhao, A. Wang, P. P. Altermatt, and M. A. Green, "18.2% efficient multicrystalline silicon cell," in *Conference Record of the Twenty Sixth IEEE Photovoltaic Specialists Conference-1997*, pp. 227–230, IEEE, 1997.

[58] K.-J. Lee, J.-H. Kim, H.-S. Kim, D. Shin, D.-W. Yoo, and H.-J. Kim, "A study on a solar simulator for dye sensitized solar cells," *International Journal of Photoenergy*, vol. 2012, 2012.

[59] J. Halme *et al.*, "Dye-sensitized nanostructured and organic photovoltaic cells: technical review and preliminary tests," 2002.

[60] S. Shalini, R. Balasundaraprabhu, T. S. Kumar, N. Prabavathy, S. Senthilarasu, and S. Prasanna, "Status and outlook of sensitizers/dyes used in dye sensitized solar cells (dssc): a review," *International Journal of Energy Research*, vol. 40, no. 10, pp. 1303–1320, 2016.

[61] W. S. Yang, J. H. Noh, N. J. Jeon, Y. C. Kim, S. Ryu, J. Seo, and S. I. Seok, "High-performance photovoltaic perovskite layers fabricated through intramolecular exchange," *Science*, vol. 348, no. 6240, pp. 1234–1237, 2015.

[62] J. S. Shaikh, N. S. Shaikh, S. S. Mali, J. V. Patil, K. K. Pawar, P. Kanjanaboos, C. K. Hong, J. H. Kim, and P. S. Patil, "Nanoarchitectures in dye-sensitized solar cells: metal oxides, oxide perovskites and carbon-based materials," *Nanoscale*, vol. 10, no. 11, pp. 4987–5034, 2018.

[63] H. You, R. Liu, C. Liang, S. Yang, F. Wang, X. Lu, and B. Ding, "Gold nanoparticle doped hollow SnO_2 supersymmetric nanostructures for improved photocatalysis," *Journal of Materials Chemistry A*, vol. 1, no. 12, pp. 4097–4104, 2013.

[64] D. Jeannot, J. Pinard, P. Ramoni, and E. M. Jost, "Physical and chemical properties of metal oxide additions to Ag-SnO/Sub_2/contact materials and predictions of electrical performance," *IEEE Transactions on Components, Packaging, and Manufacturing Technology: Part A*, vol. 17, no. 1, pp. 17–23, 1994.

[65] S. Gubbala, V. Chakrapani, V. Kumar, and M. K. Sunkara, "Band-edge engineered hybrid structures for dye-sensitized solar cells based on SnO_2 nanowires," *Advanced Functional Materials*, vol. 18, no. 16, pp. 2411–2418, 2008.

[66] K. Basu, D. Benetti, H. Zhao, L. Jin, F. Vetrone, A. Vomiero, and F. Rosei, "Enhanced photovoltaic properties in dye sensitized solar cells by surface treatment of SnO_2 photoanodes," *Scientific reports*, vol. 6, p. 23312, 2016.

[67] Q. Wali, A. Fakharuddin, I. Ahmed, M. H. Ab Rahim, J. Ismail, and R. Jose, "Multiporous nanofibers of SnO_2 by electrospinning for high efficiency dye-sensitized solar cells," *Journal of Materials Chemistry A*, vol. 2, no. 41, pp. 17427–17434, 2014.

[68] A. Mallick, P. More, S. Ghosh, R. Chippalkatti, B. A. Chopade, M. Lahiri, and S. Basu, "Dual drug conjugated nanoparticle for simultaneous targeting of mitochondria and nucleus in cancer cells," *ACS applied materials & interfaces*, vol. 7, no. 14, pp. 7584–7598, 2015.

[69] Z. Dong, H. Ren, C. M. Hessel, J. Wang, R. Yu, Q. Jin, M. Yang, Z. Hu, Y. Chen, Z. Tang, *et al.*, "Quintuple-shelled SnO_2 hollow microspheres with superior light scattering for high-performance dye-sensitized solar cells," *Advanced Materials*, vol. 26, no. 6, pp. 905–909, 2014.

[70] F. Wang, C. Di Valentin, and G. Pacchioni, "Rational band gap engineering of WO_3 photocatalyst for visible light water splitting," *ChemCatChem*, vol. 4, no. 4, pp. 476–478, 2012.

[71] M. Gillet, K. Aguir, C. Lemire, E. Gillet, and K. Schierbaum, "The structure and electrical conductivity of vacuum-annealed WO_3 thin films," *Thin Solid Films*, vol. 467, no. 1-2, pp. 239–246, 2004.

[72] K. Hara, Z.-G. Zhao, Y. Cui, M. Miyauchi, M. Miyashita, and S. Mori, "Nanocrystalline electrodes based on nanoporous-walled WO_3 nanotubes for organic-dye-sensitized solar cells," *Langmuir*, vol. 27, no. 20, pp. 12730–12736, 2011.

[73] G. Yang, X.-J. Fu, J.-B. Sun, and J. Zhou, "Optical properties of aluminum silver alloy films deposited by magnetron sputtering," *Journal of alloys and compounds*, vol. 547, pp. 23–28, 2013.

[74] A. Rajendran and S. Kandasamy, "Synthesis and photovoltaic property characterization of CeO_2 film deposited on ITO substrate for dye sensitized solar cell," *Materials Research Innovations*, vol. 23, no. 1, pp. 15–21, 2019.

[75] H. Yu, Y. Bai, X. Zong, F. Tang, G. M. Lu, and L. Wang, "Cubic CeO_2 nanoparticles as mirror-like scattering layers for efficient light harvesting in dye-sensitized solar cells," *Chemical Communications*, vol. 48, no. 59, pp. 7386–7388, 2012.

[76] M. Shahpari, A. Behjat, M. Khajaminian, and N. Torabi, "The influence of morphology of hematite (α-Fe_2O_3) counter electrodes on the efficiency of dye-sensitized solar cells," *Solar Energy*, vol. 119, pp. 45–53, 2015.

[77] M. Cavas, R. Gupta, A. A. Al-Ghamdi, Z. H. Gafer, F. El-Tantawy, and F. Yakuphanoglu, "Preparation and characterization of dye sensitized solar cell based on nanostructured Fe_2O_3," *Materials Letters*, vol. 105, pp. 106–109, 2013.

[78] K. Ocakoglu, T. Krupnik, B. van den Bosch, E. Harputlu, M. P. Gullo, J. D. J. Olmos, S. Yildirimcan, R. K. Gupta, F. Yakuphanoglu, A. Barbieri, *et al.*, "Photosystem i-based biophotovoltaics on nanostructured hematite," *Advanced Functional Materials*, vol. 24, no. 47, pp. 7467–7477, 2014.

[79] J. Z. Ou, R. A. Rani, M.-H. Ham, M. R. Field, Y. Zhang, H. Zheng, P. Reece, S. Zhuiykov, S. Sriram, M. Bhaskaran, *et al.*, "Elevated temperature anodized Nb_2O_5: a photoanode material with exceptionally large photoconversion efficiencies," *ACS nano*, vol. 6, no. 5, pp. 4045–4053, 2012.

[80] J. Glasscock, P. Barnes, I. Plumb, A. Bendavid, and P. Martin, "Structural, optical and electrical properties of undoped polycrystalline hematite thin films produced using filtered arc deposition," *Thin Solid Films*, vol. 516, no. 8, pp. 1716–1724, 2008.

[81] H. Zhang, Y. Wang, D. Yang, Y. Li, H. Liu, P. Liu, B. J. Wood, and H. Zhao, "Directly hydrothermal growth of single crystal Nb_3O_7 (oh) nanorod film for high performance dye-sensitized solar cells," *Advanced Materials*, vol. 24, no. 12, pp. 1598–1603, 2012.

[82] K. Sayama, H. Sugihara, and H. Arakawa, "Photoelectrochemical properties of a porous Nb_3O_7 electrode sensitized by a ruthenium dye," *Chemistry of Materials*, vol. 10, no. 12, pp. 3825–3832, 1998.

[83] A. áRanga Rao, "V. ádutta," *Nanotechnology*, vol. 19, p. 445712, 2008.

[84] N. Memarian, I. Concina, A. Braga, S. M. Rozati, A. Vomiero, and G. Sberveglieri, "Hierarchically assembled ZnO nanocrystallites for high-efficiency dye-sensitized solar cells," *Angewandte Chemie*, vol. 123, no. 51, pp. 12529–12533, 2011.

[85] S. Yang, H. Kou, H. Wang, K. Cheng, and J. Wang, "The photoelectrochemical properties of N3 sensitized $CaTiO_3$ modified TiO_2 nanocrystalline electrodes," *Electrochimica Acta*, vol. 55, no. 1, pp. 305–310, 2009.

[86] K. G. Baiju, B. Murali, and D. Kumaresan, "Synthesis of hierarchical barium titanate micro flowers with superior light-harvesting characteristics for dye sensitized solar cells," *Materials Research Express*, vol. 5, no. 7, p. 075503, 2018.

[87] S. Yang, H. Kou, J. Wang, H. Xue, and H. Han, "Tunability of the band energetics of nanostructured $SrTiO_3$ electrodes for dye-sensitized solar cells," *The Journal of Physical Chemistry C*, vol. 114, no. 9, pp. 4245–4249, 2010.

[88] S. Burnside, J.-E. Moser, K. Brooks, M. Grätzel, and D. Cahen, "Nanocrystalline mesoporous strontium titanate as photoelectrode material for photosensitized solar devices: increasing photovoltage through flatband potential engineering," *The Journal of Physical Chemistry B*, vol. 103, no. 43, pp. 9328–9332, 1999.

[89] D. W. Kim, S. S. Shin, S. Lee, I. S. Cho, D. H. Kim, C. W. Lee, H. S. Jung, and K. S. Hong, "$BaSnO_3$ perovskite nanoparticles for high efficiency dye-sensitized solar cells," *ChemSusChem*, vol. 6, no. 3, pp. 449–454, 2013.

[90] S. S. Shin, J. S. Kim, J. H. Suk, K. D. Lee, D. W. Kim, J. H. Park, I. S. Cho, K. S. Hong, and J. Y. Kim, "Improved quantum efficiency of highly efficient perovskite $BaSnO_3$-based dye-sensitized solar cells," *ACS nano*, vol. 7, no. 2, pp. 1027–1035, 2013.

[91] K. Sarkar, E. V. Braden, T. Fröschl, N. Hüsing, and P. Müller-Buschbaum, "Spray-deposited zinc titanate films obtained via sol-gel synthesis for application in dye-sensitized solar cells," *Journal of Materials Chemistry A*, vol. 2, no. 36, pp. 15008–15014, 2014.

[92] J. Yu, D. Li, L. Zhu, and X. Xu, "Application of $ZnTiO_3$ in quantum-dot-sensitized solar cells and numerical simulations using first-principles theory," *Journal of Alloys and Compounds*, vol. 681, pp. 88–95, 2016.

[93] S. Shin, S. Lee, and S. I. Seok, "Exploring wide bandgap metal oxides for perovskite solar cells," *APL Materials*, vol. 7, no. 2, p. 022401, 2019.

[94] Q. Tang, Z. Zhou, and Z. Chen, "Innovation and discovery of graphene-like materials via density-functional theory computations," *Wiley Interdisciplinary Reviews: Computational Molecular Science*, vol. 5, no. 5, pp. 360–379, 2015.

[95] E. Pavarini, E. Koch, F. Anders, and M. Jarrell, "Correlated electrons: from models to materials," *Reihe Modeling and Simulation*, vol. 2, 2012.

[96] P. Qin, A. L. Domanski, A. K. Chandiran, R. Berger, H.-J. Butt, M. I. Dar, T. Moehl, N. Tetreault, P. Gao, S. Ahmad, *et al.*, "Yttrium-substituted nanocrystalline TiO_2 photoanodes for perovskite based heterojunction solar cells," *Nanoscale*, vol. 6, no. 3, pp. 1508–1514, 2014.

[97] Q. Yu, Y. Wang, Z. Yi, N. Zu, J. Zhang, M. Zhang, and P. Wang, "High-efficiency dye-sensitized solar cells: the influence of lithium ions on exciton dissociation, charge recombination, and surface states," *ACS nano*, vol. 4, no. 10, pp. 6032–6038, 2010.

[98] Y.-S. Yen, H.-H. Chou, Y.-C. Chen, C.-Y. Hsu, and J. T. Lin, "Recent developments in molecule-based organic materials for dye-sensitized solar cells," *Journal of Materials Chemistry*, vol. 22, no. 18, pp. 8734–8747, 2012.

[99] M. Wang, C. Grätzel, S. M. Zakeeruddin, and M. Grätzel, "Recent developments in redox electrolytes for dye-sensitized solar cells," *Energy & Environmental Science*, vol. 5, no. 11, pp. 9394–9405, 2012.

[100] J. N. de Freitas, A. F. Nogueira, and M.-A. De Paoli, "New insights into dye-sensitized solar cells with polymer electrolytes," *Journal of Materials Chemistry*, vol. 19, no. 30, pp. 5279–5294, 2009.

[101] S. Bai, C. Bu, Q. Tai, L. Liang, Y. Liu, S. You, Z. Yu, S. Guo, and X. Zhao, "Effects of bis (imidazolium) molten salts with different substituents of imidazolium cations

on the performance of efficient dye-sensitized solar cells," *ACS Applied Materials & Interfaces*, vol. 5, no. 8, pp. 3356–3361, 2013.

[102] M. B. Achari, V. Elumalai, N. Vlachopoulos, M. Safdari, J. Gao, J. M. Gardner, and L. Kloo, "A quasi-liquid polymer-based cobalt redox mediator electrolyte for dye-sensitized solar cells," *Physical Chemistry Chemical Physics*, vol. 15, no. 40, pp. 17419–17425, 2013.

[103] J. Ci, C. Cao, S. Kuga, J. Shen, M. Wu, and Y. Huang, "Improved performance of microbial fuel cell using esterified corncob cellulose nanofibers to fabricate air-cathode gas diffusion layer," *ACS Sustainable Chemistry & Engineering*, vol. 5, no. 11, pp. 9614–9618, 2017.

[104] D. Li, D. Qin, M. Deng, Y. Luo, and Q. Meng, "Optimization the solid-state electrolytes for dye-sensitized solar cells," *Energy & environmental science*, vol. 2, no. 3, pp. 283–291, 2009.

[105] G. Hodes and D. Cahen, "All-solid-state, semiconductor-sensitized nanoporous solar cells," *Accounts of chemical research*, vol. 45, no. 5, pp. 705–713, 2012.

[106] D. Bi, L. Yang, G. Boschloo, A. Hagfeldt, and E. M. Johansson, "Effect of different hole transport materials on recombination in $CH_3NH_3PbI_3$ perovskite-sensitized mesoscopic solar cells," *The journal of physical chemistry letters*, vol. 4, no. 9, pp. 1532–1536, 2013.

[107] B. Lee, J. He, R. P. Chang, and M. G. Kanatzidis, "All-solid-state dye-sensitized solar cells with high efficiency," *Nature*, vol. 485, no. 7399, pp. 486–489, 2012.

[108] J. H. Heo, S. H. Im, J. H. Noh, T. N. Mandal, C.-S. Lim, J. A. Chang, Y. H. Lee, H.-j. Kim, A. Sarkar, M. K. Nazeeruddin, *et al.*, "Efficient inorganic–organic hybrid heterojunction solar cells containing perovskite compound and polymeric hole conductors," *Nature photonics*, vol. 7, no. 6, pp. 486–491, 2013.

[109] J. Burschka, "pellet, n.; moon, s."

[110] M. Wu and T. Ma, "Platinum-free catalysts as counter electrodes in dye-sensitized solar cells," *ChemSusChem*, vol. 5, no. 8, pp. 1343–1357, 2012.

[111] S.-Q. Fan, B. Fang, J. H. Kim, B. Jeong, C. Kim, J.-S. Yu, and J. Ko, "Ordered multimodal porous carbon as highly efficient counter electrodes in dye-sensitized and quantum-dot solar cells," *Langmuir*, vol. 26, no. 16, pp. 13644–13649, 2010.

[112] H. Wang, K. Sun, F. Tao, D. J. Stacchiola, and Y. H. Hu, "3d honeycomb-like structured graphene and its high efficiency as a counter-electrode catalyst for dye-sensitized solar cells," *Angewandte Chemie International Edition*, vol. 52, no. 35, pp. 9210–9214, 2013.

[113] Y. Jo, J. Y. Cheon, J. Yu, H. Y. Jeong, C.-H. Han, Y. Jun, and S. H. Joo, "Highly interconnected ordered mesoporous carbon–carbon nanotube nanocomposites: Pt-free, highly efficient, and durable counter electrodes for dye-sensitized solar cells," *Chemical Communications*, vol. 48, no. 65, pp. 8057–8059, 2012.

[114] Z. Yang, M. Liu, C. Zhang, W. W. Tjiu, T. Liu, and H. Peng, "Carbon nanotubes bridged with graphene nanoribbons and their use in high-efficiency dye-sensitized solar cells," *Angewandte Chemie*, vol. 125, no. 14, pp. 4088–4091, 2013.

[115] M. S. Faber, K. Park, M. Caban-Acevedo, P. K. Santra, and S. Jin, "Earth-abundant cobalt pyrite COS_2 thin film on glass as a robust, high-performance counter electrode for quantum dot-sensitized solar cells," *The journal of physical chemistry letters*, vol. 4, no. 11, pp. 1843–1849, 2013.

[116] S.-H. Chang, M.-D. Lu, Y.-L. Tung, and H.-Y. Tuan, "Gram-scale synthesis of catalytic CO_9S_8 nanocrystal ink as a cathode material for spray-deposited, large-area dye-sensitized solar cells," *ACS nano*, vol. 7, no. 10, pp. 9443–9451, 2013.

[117] R.-Y. Yao, Z.-J. Zhou, Z.-L. Hou, X. Wang, W.-H. Zhou, and S.-X. Wu, "Surfactant-free $CuInS_2$ nanocrystals: an alternative counter-electrode material for dye-sensitized solar cells," *ACS Applied Materials & Interfaces*, vol. 5, no. 8, pp. 3143–3148, 2013.

[118] S.-J. Yuan, Z.-J. Zhou, Z.-L. Hou, W.-H. Zhou, R.-Y. Yao, Y. Zhao, and S.-X. Wu, "Enhanced performance of dye-sensitized solar cells using solution-based in situ synthesis and fabrication of $Cu_2ZnSnSe_4$ nanocrystal counter electrode," *Chemistry–A European Journal*, vol. 19, no. 31, pp. 10107–10110, 2013.

[119] H. Zhang, M. Ge, L. Yang, Z. Zhou, W. Chen, Q. Li, and L. Liu, "Synthesis and catalytic properties of Sb_2S_3 nanowire bundles as counter electrodes for dye-sensitized solar cells," *The Journal of Physical Chemistry C*, vol. 117, no. 20, pp. 10285–10290, 2013.

[120] H. Kang, E. Sowade, and R. R. Baumann, "Direct intense pulsed light sintering of inkjet-printed copper oxide layers within six milliseconds," *ACS applied materials & interfaces*, vol. 6, no. 3, pp. 1682–1687, 2014.

[121] Y. Zhao, A. Thapa, Q. Feng, M. Xi, Q. Qiao, and H. Fong, "Electrospun tic/c nano-felt surface-decorated with pt nanoparticles as highly efficient and cost-effective counter electrode for dye-sensitized solar cells," *Nanoscale*, vol. 5, no. 23, pp. 11742–11747, 2013.

[122] W. Wei, H. Wang, and Y. H. Hu, "Unusual particle-size-induced promoter-to-poison transition of zrn in counter electrodes for dye-sensitized solar cells," *Journal of Materials Chemistry A*, vol. 1, no. 45, pp. 14350–14357, 2013.

[123] Z. Wen, S. Cui, H. Pu, S. Mao, K. Yu, X. Feng, and J. Chen, "Metal nitride/graphene nanohybrids: general synthesis and multifunctional titanium nitride/graphene electrocatalyst," *Advanced Materials*, vol. 23, no. 45, pp. 5445–5450, 2011.

[124] M.-S. Wu and J.-F. Wu, "Pulse-reverse electrodeposition of transparent nickel phosphide film with porous nanospheres as a cost-effective counter electrode for dye-sensitized solar cells," *Chemical Communications*, vol. 49, no. 93, pp. 10971–10973, 2013.

[125] J. Guo, Y. Shi, Y. Chu, and T. Ma, "Highly efficient telluride electrocatalysts for use as pt-free counter electrodes in dye-sensitized solar cells," *Chemical Communications*, vol. 49, no. 86, pp. 10157–10159, 2013.

[126] M. Wu, X. Lin, A. Hagfeldt, and T. Ma, "A novel catalyst of WO_2 nanorod for the counter electrode of dye-sensitized solar cells," *Chemical Communications*, vol. 47, no. 15, pp. 4535–4537, 2011.

[127] R. Trevisan, M. Döbbelin, P. P. Boix, E. M. Barea, R. Tena-Zaera, I. Mora-Seró, and J. Bisquert, "Pedot nanotube arrays as high performing counter electrodes for dye sensitized solar cells. study of the interactions among electrolytes and counter electrodes," *Advanced Energy Materials*, vol. 1, no. 5, pp. 781–784, 2011.

[128] J. Xia, L. Chen, and S. Yanagida, "Application of polypyrrole as a counter electrode for a dye-sensitized solar cell," *Journal of Materials Chemistry*, vol. 21, no. 12, pp. 4644–4649, 2011.

[129] W. Sun, T. Peng, Y. Liu, S. Xu, J. Yuan, S. Guo, and X.-Z. Zhao, "Hierarchically porous hybrids of polyaniline nanoparticles anchored on reduced graphene oxide sheets as counter electrodes for dye-sensitized solar cells," *Journal of Materials Chemistry A*, vol. 1, no. 8, pp. 2762–2768, 2013.

[130] C. Yuan, S. Guo, S. Wang, L. Liu, W. Chen, and E. Wang, "Electropolymerization polyoxometalate (pom)-doped pedot film electrodes with mastoid microstructure and its application in dye-sensitized solar cells (dsscs)," *Industrial & Engineering Chemistry Research*, vol. 52, no. 20, pp. 6694–6703, 2013.

[131] Z. Zhang, X. Zhang, H. Xu, Z. Liu, S. Pang, X. Zhou, S. Dong, X. Chen, and G. Cui, "$CuInS_2$ nanocrystals/pedot: Pss composite counter electrode for dye-sensitized solar cells," *ACS applied materials & interfaces*, vol. 4, no. 11, pp. 6242–6246, 2012.

[132] G. Guan, Z. Yang, L. Qiu, X. Sun, Z. Zhang, J. Ren, and H. Peng, "Oriented pedot: Pss on aligned carbon nanotubes for efficient dye-sensitized solar cells," *Journal of Materials Chemistry A*, vol. 1, no. 42, pp. 13268–13273, 2013.

[133] R. Bajpai, S. Roy, P. Kumar, P. Bajpai, N. Kulshrestha, J. Rafiee, N. Koratkar, and D. Misra, "Graphene supported platinum nanoparticle counter-electrode for enhanced performance of dye-sensitized solar cells," *ACS Applied Materials & Interfaces*, vol. 3, no. 10, pp. 3884–3889, 2011.

[134] Y. Li, H. Wang, Q. Feng, G. Zhou, and Z.-S. Wang, "Reduced graphene oxide–TaON composite as a high-performance counter electrode for co (bpy) $33^{+}/2^{+-}$ mediated dye-sensitized solar cells," *ACS applied materials & interfaces*, vol. 5, no. 16, pp. 8217–8224, 2013.

[135] "nis_2,"

[136] L. Chen, C. X. Guo, Q. Zhang, Y. Lei, J. Xie, S. Ee, G. Guai, Q. Song, and C. M. Li, "Graphene quantum-dot-doped polypyrrole counter electrode for high-performance dye-sensitized solar cells," *ACS applied materials & interfaces*, vol. 5, no. 6, pp. 2047–2052, 2013.

[137] V.-D. Dao, L. L. Larina, K.-D. Jung, J.-K. Lee, and H.-S. Choi, "Graphene–NiO nanohybrid prepared by dry plasma reduction as a low-cost counter electrode material for dye-sensitized solar cells," *Nanoscale*, vol. 6, no. 1, pp. 477–482, 2014.

[138] H.-Y. Chen, J.-Y. Liao, B.-X. Lei, D.-B. Kuang, Y. Fang, and C.-Y. Su, "Highly catalytic carbon nanotube/pt nanohybrid-based transparent counter electrode for efficient dye-sensitized solar cells," *Chemistry–An Asian Journal*, vol. 7, no. 8, pp. 1795–1802, 2012.

[139] Y. Xiao, J. Wu, J. Lin, G. Yue, J. Lin, M. Huang, Y. Huang, Z. Lan, and L. Fan, "A high performance pt-free counter electrode of nickel sulfide/multi-wall carbon nanotube/titanium used in dye-sensitized solar cells," *Journal of Materials Chemistry A*, vol. 1, no. 44, pp. 13885–13889, 2013.

[140] G. Yue, J. Wu, J.-Y. Lin, Y. Xiao, S.-Y. Tai, J. Lin, M. Huang, and Z. Lan, "A counter electrode of multi-wall carbon nanotubes decorated with tungsten sulfide used in dye-sensitized solar cells," *Carbon*, vol. 55, pp. 1–9, 2013.

[141] G.-r. Li, F. Wang, Q.-w. Jiang, X.-p. Gao, and P.-w. Shen, "Carbon nanotubes with titanium nitride as a low-cost counter-electrode material for dye-sensitized solar cells," *Angewandte Chemie International Edition*, vol. 49, no. 21, pp. 3653–3656, 2010.

[142] D. BIOVIA, "Materials studio overview."

[143] D. S. Biovia, "Discovery studio visualizer," *San Diego, CA, USA*, vol. 936, 2017.

[144] C. Bonhomme, C. Gervais, F. Babonneau, C. Coelho, F. Pourpoint, T. Azais, S. E. Ashbrook, J. M. Griffin, J. R. Yates, F. Mauri, *et al.*, "First-principles calculation of nmr parameters using the gauge including projector augmented wave method: a chemist's point of view," *Chemical Reviews*, vol. 112, no. 11, pp. 5733–5779, 2012.

[145] C.-K. Skylaris, P. D. Haynes, A. A. Mostofi, and M. C. Payne, "Introducing onetep: Linear-scaling density functional simulations on parallel computers," *The Journal of chemical physics*, vol. 122, no. 8, p. 084119, 2005.

[146] L. Tannas, "System requirements," in *Flat-Panel Displays and CRTs*, pp. 31–53, Springer, 1985.

[147] D. Zhou, "An introduction of density functional theory and its application," *Physics. Drexel. Edu*, 2007.

[148] J. Yu, D. Li, L. Zhu, and X. Xu, "Application of zntio3 in quantum-dot-sensitized solar cells and numerical simulations using first-principles theory," *Journal of Alloys and Compounds*, vol. 681, pp. 88–95, 2016.

[149] A. D. Lozano-Gorrín, "Structural characterization of new perovskites," in *Polycrystalline Materials: Theoretical and Practical Aspects*, pp. 107–124, IntechOpen, 2012.

[150] M. Johnsson and P. Lemmens, "Crystallography and chemistry of perovskites," *Handbook of magnetism and advanced magnetic materials*, 2007.

[151] F. Dulln and D. Rase, "Phase equilibria in the system zno—tio2," *Journal of the American Ceramic Society*, vol. 43, no. 3, pp. 125–131, 1960.

[152] W. Mojtahedi and J. Abbasian, "H2s removal from coal gas at elevated temperature and pressure in fluidized bed with zinc titanate sorbents. 2. sorbent durability," *Energy & fuels*, vol. 9, no. 5, pp. 782–787, 1995.

[153] K. Haga, T. Ishii, J.-i. Mashiyama, and T. Ikeda, "Dielectric properties of two-phase mixture ceramics composed of rutile and its compounds," *Japanese journal of applied physics*, vol. 31, no. 9S, p. 3156, 1992.

[154] H. T. Kim, J.-C. Hwang, J.-H. Nam, B. H. Choi, and M. T. Lanagan, "Structure and microwave dielectric properties of (Zn 1-x Nix) TiO_3 ceramics," *Journal of materials research*, vol. 18, no. 5, pp. 1067–1072, 2003.

[155] L. Zhao, F. Liu, X. Wang, Z. Zhang, and J. Yan, "Preparation and characterizations of $ZnTiO_3$ powders by sol–gel process," *Journal of sol-gel science and technology*, vol. 33, no. 1, pp. 103–106, 2005.

[156] H. Obayashi, Y. Sakurai, and T. Gejo, "Perovskite-type oxides as ethanol sensors," *Journal of Solid State Chemistry*, vol. 17, no. 3, pp. 299–303, 1976.

[157] S. F. Wang, F. Gu, M. K. Lü, W. G. Zou, S. W. Liu, D. Xu, D. R. Yuan, and G. J. Zhou, "Photoluminescence characteristics of $ZnTiO_3$: $Bi3^+$ nanocrystals," *Journal of Physics and Chemistry of Solids*, vol. 65, no. 7, pp. 1243–1245, 2004.

[158] M. Pastore and F. De Angelis, "Computational modelling of TiO_2 surfaces sensitized by organic dyes with different anchoring groups: adsorption modes, electronic structure and implication for electron injection/recombination," *Physical Chemistry Chemical Physics*, vol. 14, no. 2, pp. 920–928, 2012.

[159] P. W. Borthwick, "Some relationships between bond lengths and angles in–COO^-,–COOH and–cooch3 groups," *Acta Crystallographica Section B: Structural Crystallography and Crystal Chemistry*, vol. 36, no. 3, pp. 628–632, 1980.

[160] R. L. Akkermans, N. A. Spenley, and S. H. Robertson, "Monte carlo methods in materials studio," *Molecular Simulation*, vol. 39, no. 14-15, pp. 1153–1164, 2013.

[161] K. Khaled, "Molecular simulation, quantum chemical calculations and electrochemical studies for inhibition of mild steel by triazoles," *Electrochimica Acta*, vol. 53, no. 9, pp. 3484–3492, 2008.

[162] Y. Lu, D.-j. Choi, J. Nelson, O.-B. Yang, and B. Parkinson, "Adsorption, desorption, and sensitization of low-index anatase and rutile surfaces by the ruthenium complex dye N3," *Journal of The Electrochemical Society*, vol. 153, no. 8, p. E131, 2006.

[163] M. Pastore and F. De Angelis, "Computational modelling of TiO_2 surfaces sensitized by organic dyes with different anchoring groups: adsorption modes, electronic structure and implication for electron injection/recombination," *Physical Chemistry Chemical Physics*, vol. 14, no. 2, pp. 920–928, 2012.

[164] Y. Xu and M. A. Schoonen, "The absolute energy positions of conduction and valence bands of selected semiconducting minerals," *American Mineralogist*, vol. 85, no. 3-4, pp. 543–556, 2000.

[165] M. Skompska and K. Zarębska, "Electrodeposition of ZnO nanorod arrays on transparent conducting substrates–a review," *Electrochimica Acta*, vol. 127, pp. 467–488, 2014.

[166] L. Znaidi, "Sol–gel-deposited ZnO thin films: A review," *Materials Science and Engineering: B*, vol. 174, no. 1-3, pp. 18–30, 2010.

[167] M. Benali Kanoun, S. Goumri-Said, A. Manchon, and U. Schwingenschlögl, "Ferromagnetism carried by highly delocalized hybrid states in sc-doped ZnO thin films," *Applied Physics Letters*, vol. 100, no. 22, p. 222406, 2012.

[168] C. Xu, J. Wu, U. V. Desai, and D. Gao, "Multilayer assembly of nanowire arrays for dye-sensitized solar cells," *Journal of the American Chemical Society*, vol. 133, no. 21, pp. 8122–8125, 2011.

[169] J. Yu, D. Li, L. Zhu, and X. Xu, "Application of $ZnTiO_3$ in quantum-dot-sensitized solar cells and numerical simulations using first-principles theory," *Journal of Alloys and Compounds*, vol. 681, pp. 88–95, 2016.

[170] M. C. Payne, M. P. Teter, D. C. Allan, T. Arias, and a. J. Joannopoulos, "Iterative minimization techniques for ab initio total-energy calculations: molecular dynamics and conjugate gradients," *Reviews of modern physics*, vol. 64, no. 4, p. 1045, 1992.

[171] F. De Angelis, S. Fantacci, E. Mosconi, M. K. Nazeeruddin, and M. Gratzel, "Absorption spectra and excited state energy levels of the N719 dye on TiO_2 in dye-sensitized solar cell models," *The Journal of Physical Chemistry C*, vol. 115, no. 17, pp. 8825–8831, 2011.

[172] U. Staub, R. De Souza, P. Beaud, E. Möhr-Vorobeva, G. Ingold, A. Caviezel, V. Scagnoli, B. Delley, W. Schlotter, J. Turner, *et al.*, "Persistence of magnetic order in a highly excited Cu^{2+} state in CuO," *Physical Review B*, vol. 89, no. 22, p. 220401, 2014.

[173] K. Chaitanya, B. M. Heron, and X.-H. Ju, "Influence of a local electric field on the light harvesting efficiency of a cyclopentadithiophene-bridged da-π-a indoline dye on pure and n-doped tio2 surfaces," *Dyes and Pigments*, vol. 141, pp. 501–511, 2017.

[174] M. Guo, H. Yang, X. Jian, J. Li, Z. Liang, and P. Han, "The adsorptions of fixed groups- cn,- NH_2,- SH,- OH and- COOH of dye molecules on stoichiometric, oxygen vacancy and pt-doped SnO_2 (110) surfaces," *Applied Surface Science*, vol. 428, pp. 851–860, 2018.

[175] J. P. Perdew and Y. Wang, "Accurate and simple analytic representation of the electron-gas correlation energy," *Physical review B*, vol. 45, no. 23, p. 13244, 1992.

[176] M. Cossi and V. Barone, "Time-dependent density functional theory for molecules in liquid solutions," *The Journal of chemical physics*, vol. 115, no. 10, pp. 4708–4717, 2001.

[177] S. J. Clark, M. D. Segall, C. J. Pickard, P. J. Hasnip, M. I. Probert, K. Refson, and M. C. Payne, "First principles methods using castep," *Zeitschrift für kristallographie-crystalline materials*, vol. 220, no. 5-6, pp. 567–570, 2005.

[178] S. Appalakondaiah, G. Vaitheeswaran, S. Lebegue, N. E. Christensen, and A. Svane, "Effect of van der waals interactions on the structural and elastic properties of black phosphorus," *Physical Review B*, vol. 86, no. 3, p. 035105, 2012.

[179] P. Wang, S. M. Zakeeruddin, J. E. Moser, M. K. Nazeeruddin, T. Sekiguchi, and M. Grätzel, "A stable quasi-solid-state dye-sensitized solar cell with an amphiphilic ruthenium sensitizer and polymer gel electrolyte," *Nature materials*, vol. 2, no. 6, pp. 402–407, 2003.

[180] C.-Y. Chen, S.-J. Wu, C.-G. Wu, J.-G. Chen, and K.-C. Ho, "A ruthenium complex with superhigh light-harvesting capacity for dye-sensitized solar cells," *Angewandte chemie*, vol. 118, no. 35, pp. 5954–5957, 2006.

[181] S. Suhaimi, M. M. Shahimin, Z. Alahmed, J. Chyskỳ, and A. Reshak, "Materials for enhanced dye-sensitized solar cell performance: Electrochemical application," *Int. J. Electrochem. Sci*, vol. 10, no. 4, pp. 2859–2871, 2015.

[182] M. Ihara, K. Tanaka, K. Sakaki, I. Honma, and K. Yamada, "Enhancement of the absorption coefficient of cis^{-} (ncs) 2 bis (2, 2 '-bipyridyl-4, 4 '-dicarboxylate) ruthenium (ii) dye in dye-sensitized solar cells by a silver island film," *The Journal of Physical Chemistry B*, vol. 101, no. 26, pp. 5153–5157, 1997.

[183] A. Benghia, T. Dahame, and B. Bentria, "First principle calculation of physical properties of barium based chalcogenides BaM_4S_7 (m= ga, al); a dft, dft-d and hybrid functional hse06 study," *Optical Materials*, vol. 54, pp. 269–275, 2016.

[184] J. Yu, D. Li, L. Zhu, and X. Xu, "Application of $ZnTiO_3$ in quantum-dot-sensitized solar cells and numerical simulations using first-principles theory," *Journal of Alloys and Compounds*, vol. 681, pp. 88–95, 2016.

[185] N. Serpone, "Is the band gap of pristine TiO_2 narrowed by anion-and cation-doping of titanium dioxide in second-generation photocatalysts?," *The Journal of Physical Chemistry B*, vol. 110, no. 48, pp. 24287–24293, 2006.

[186] Z.-X. Li, F.-B. Shi, Y. Ding, T. Zhang, and C.-H. Yan, "Facile synthesis of highly ordered mesoporous $ZnTiO_3$ with crystalline walls by self-adjusting method," *Langmuir*, vol. 27, no. 23, pp. 14589–14593, 2011.

[187] M. Pastore and F. De Angelis, "Computational modelling of TiO_2 surfaces sensitized by organic dyes with different anchoring groups: adsorption modes, electronic structure and implication for electron injection/recombination," *Physical Chemistry Chemical Physics*, vol. 14, no. 2, pp. 920–928, 2012.

[188] J. Ruiyu, L. Dengyang, C. Chao, Z. Tao, Y. Fanfan, and Z. Jinhong, "Adsorption simulation of sulfur oxide on the surface of metal," *Journal of Chemical and Pharmaceutical Research*, vol. 6, no. 3, pp. 949–954, 2014.

[189] J. M. Azpiroz and F. De Angelis, "Dft/tddft study of the adsorption of N3 and N719 dyes on ZnO (1010) surfaces," *The Journal of Physical Chemistry A*, vol. 118, no. 31, pp. 5885–5893, 2014.

[190] H. Yang, J. Li, G. Zhou, S. W. Chiang, H. Du, L. Gan, C. Xu, F. Kang, and W. Duan, "First principles study of ruthenium (ii) sensitizer adsorption on anatase TiO_2 (001) surface," *RSC advances*, vol. 5, no. 74, pp. 60230–60236, 2015.

[191] C. Sun, Y. Li, P. Song, and F. Ma, "An experimental and theoretical investigation of the electronic structures and photoelectrical properties of ethyl red and carminic acid for dssc application," *Materials*, vol. 9, no. 10, p. 813, 2016.

[192] J. P. Hill, "Molecular engineering combined with cosensitization leads to record photovoltaic efficiency for non-ruthenium solar cells," *Angewandte Chemie International Edition*, vol. 55, no. 9, pp. 2976–2978, 2016.

[193] W. Li, L. G. Rego, F.-Q. Bai, J. Wang, R. Jia, L.-M. Xie, and H.-X. Zhang, "What makes hydroxamate a promising anchoring group in dye-sensitized solar cells? insights from theoretical investigation," *The journal of physical chemistry letters*, vol. 5, no. 22, pp. 3992–3999, 2014.

[194] Y. Xu and M. A. Schoonen, "The absolute energy positions of conduction and valence bands of selected semiconducting minerals," *American Mineralogist*, vol. 85, no. 3-4, pp. 543–556, 2000.

[195] H.-C. Zhu, J. Zhang, and Y.-L. Wang, "Adsorption orientation effects of porphyrin dyes on the performance of dssc: Comparison of benzoic acid and tropolone anchoring groups binding onto the TiO_2 anatase (101) surface," *Applied Surface Science*, vol. 433, pp. 1137–1147, 2018.

[196] W. Zhang, J. Wu, Y. Wen, W. Wu, and L. Wang, "First principles study on interface between dual-channel anchorable organic dyes and TiO_2 for dye-sensitized solar cells," *Dyes and Pigments*, vol. 149, pp. 908–914, 2018.

[197] C. Sundari, M. Martoprawiro, and A. Ivansyah, "A dft and tddft study of pcm effect on N3 dye absorption in ethanol solution," in *Journal of Physics: Conference Series*, vol. 812, p. 012068, IOP Publishing, 2017.

[198] Z. M. E. Fahim, S. M. Bouzzine, M. M. Hamidi, M. Bouachrine, M. Hamidi, G. Salgado-Morán, L. H. Mendoza-Huizar, and G. A. Alvarez-Romero, "Optoelectronic properties of triphenylamine based dyes for solar cell applications. a dft study," *Química Nova*, vol. 41, no. 2, pp. 129–133, 2018.

[199] M. Pastore, E. Mosconi, F. De Angelis, and M. Gratzel, "A computational investigation of organic dyes for dye-sensitized solar cells: benchmark, strategies, and open issues," *The Journal of Physical Chemistry C*, vol. 114, no. 15, pp. 7205–7212, 2010.

[200] J. Xu, L. Zhu, D. Fang, B. Chen, L. Liu, L. Wang, and W. Xu, "Substituent effect on the π linkers in triphenylamine dyes for sensitized solar cells: a dft/tddft study," *ChemPhysChem*, vol. 13, no. 14, pp. 3320–3329, 2012.

[201] M. Pastore and F. De Angelis, "Computational modelling of TiO_2 surfaces sensitized by organic dyes with different anchoring groups: adsorption modes, electronic structure and implication for electron injection/recombination," *Physical Chemistry Chemical Physics*, vol. 14, no. 2, pp. 920–928, 2012.

[202] A. J. Mozer, Y.-B. Cheng, A. Mishra, U. Bach, A. Nattestad, P. Bauerle, S. Powar, E. Mena-Osteritz, and M. Weidelener, "Synthesis and characterization of perylene-bithiophene-triphenylamine triads: Studies on the effect of alkyl-substitution in p-type NiO based photocathodes," 2012.

[203] C. J. Wood, K. C. Robson, P. I. Elliott, C. P. Berlinguette, and E. A. Gibson, "Novel triphenylamine-modified ruthenium (ii) terpyridine complexes for nickel oxide-based cathodic dye-sensitized solar cells," *Rsc Advances*, vol. 4, no. 11, pp. 5782–5791, 2014.

[204] Z. Zhang, J. Han, X. Li, S. Cai, and J. Su, "Novel organic dyes based on bulky tri (triphenylamine)-substituted styrene for dye-sensitized solar cells," *Chinese Journal of Chemistry*, vol. 30, no. 12, pp. 2779–2785, 2012.

[205] W. Xu, J. Pei, J. Shi, S. Peng, and J. Chen, "Influence of acceptor moiety in triphenylamine-based dyes on the properties of dye-sensitized solar cells," *Journal of Power sources*, vol. 183, no. 2, pp. 792–798, 2008.

[206] H. Tian, X. Yang, R. Chen, R. Zhang, A. Hagfeldt, and L. Sun, "Effect of different dye baths and dye-structures on the performance of dye-sensitized solar cells based on triphenylamine dyes," *The Journal of Physical Chemistry C*, vol. 112, no. 29, pp. 11023–11033, 2008.

[207] D. Jacquemin, "Perp te, ea; scuseria, ge; ciofini, i," *Adamo, CJ Chem. Theory Comput*, vol. 4, p. 123, 2008.

[208] R. A. Yukna, D. P. Callan, J. T. Krauser, G. H. Evans, M. E. Aichelmann-Reidy, K. Moore, R. Cruz, and J. B. Scott, "Multi-center clinical evaluation of combination anorganic bovine-derived hydroxyapatite matrix (abm)/cell binding peptide (p-15) as a bone replacement graft material in human periodontal osseous defects. 6-month results," *Journal of periodontology*, vol. 69, no. 6, pp. 655–663, 1998.

[209] S. Appalakondaiah and G. Vaitheeswaran, "S. leb gue, ne christensen, a. svane," *Phys. Rev. B*, vol. 86, p. 035105, 2012.

[210] J. Liang, C. Zhu, and Z. Cao, "Electronic and optical properties of the triphenylamine-based organic dye sensitized TiO_2 semiconductor: insight from

first principles calculations," *Physical Chemistry Chemical Physics*, vol. 15, no. 33, pp. 13844–13851, 2013.

[211] W. Li, L. G. Rego, F.-Q. Bai, J. Wang, R. Jia, L.-M. Xie, and H.-X. Zhang, "What makes hydroxamate a promising anchoring group in dye-sensitized solar cells? insights from theoretical investigation," *The journal of physical chemistry letters*, vol. 5, no. 22, pp. 3992–3999, 2014.

[212] Y. Xu and M. A. Schoonen, "The absolute energy positions of conduction and valence bands of selected semiconducting minerals," *American Mineralogist*, vol. 85, no. 3-4, pp. 543–556, 2000.

[213] H.-C. Zhu, J. Zhang, and Y.-L. Wang, "Adsorption orientation effects of porphyrin dyes on the performance of dssc: Comparison of benzoic acid and tropolone anchoring groups binding onto the TiO_2 anatase (101) surface," *Applied Surface Science*, vol. 433, pp. 1137–1147, 2018.

[214] S. Koops, "O, regan, bc; barnes, prf; durrant, jr," *J. Am. Chem. Soc*, vol. 131, no. 13, pp. 4808–4818, 2009.

[215] W.-H. Liu, I.-C. Wu, C.-H. Lai, C.-H. Lai, P.-T. Chou, Y.-T. Li, C.-L. Chen, Y.-Y. Hsu, and Y. Chi, "Simple organic molecules bearing a 3, 4-ethylenedioxythiophene linker for efficient dye-sensitized solar cells," *Chemical Communications*, no. 41, pp. 5152–5154, 2008.

[216] W. Zhang, J. Wu, Y. Wen, W. Wu, and L. Wang, "First principles study on interface between dual-channel anchorable organic dyes and TiO_2 for dye-sensitized solar cells," *Dyes and Pigments*, vol. 149, pp. 908–914, 2018.

[bibliography.bib]